Guidelines for Authors

This periodical is a publication of the Academic Publishing and Translation Directorate of Qassim University. Its purpose is to provide an opportunity for scholars to publish their original research.

Manuscripts will be published in on of the following platforms:

i) **Article:** It should be original and has a significant contribution to the field in which the research was conducted.
ii) **Review Article:** A critical synthesis of the current literature in a particular field, or a synthesis of the literature in a particular field during an explicit period of time.
iii) **Brief Article (Technical Notes):** A short article (note) having the same characteristics as an article.
iv) **Innovation and Invention Reports**
v) **Forum:** Letters to the Editor, comments and responses, preliminary results or findings, and miscellany.
vi) **Book Reviews**

The Editorial Board will consider manuscripts in the following fields:

- Electrical Engineering
- Civil Engineering
- Mechanical Engineering
- Chemical Engineering
- Computer Engineering
- Mining and Petroleum Engineering
- Computer Science
- Information Technology
- Information Systems
- Basic Engineering and Computer Sciences

A manuscript should be submitted in English, and, if accepted for publication, it should not be published elsewhere without the written permission of the Editor-in-Chief.

General Instructions

1. **Submission of manuscripts for publication:** Papers must be presented in final page format (not more than 20 pages, A4 size), along with a compact disk (CD) containing the contribution executed on a PC using MS Word or any updated version of it. Manuscripts should be typed using Times New Roman, 12 points font, and one and half space. Pages are to be numbered consecutively and are to include all illustrative material, such as tables and figures, in their appropriate places in the text. If the author does not follow these guidelines, the paper is likely to be rejected or delayed.
2. **Abstracts:** Manuscripts for articles, review articles, and brief articles require both Arabic and English abstracts, using not more than 200 words..
3. **Keywords:** Each article must have keywords before both abstracts (English and Arabic) and they should not exceed 10 words.
4. **Tables and other illustrations:** Tables, figures, charts, graphs and plates should be planned to fit the Journal's page size (A4 incl. running heads). Line drawings are to be presented on high quality tracing paper using black India ink. Copies are not permitted for use as originals. Line quality is required to be uniform, distinct, and in proportion to the illustration. Photographs may be submitted on glossy print paper, in either black and white, or color, or made by using Adobe Photoshop. Tables and other illustrative material must include headings or titles, and captions for figures.

5. **Abbreviations:** The names of periodicals should be abbreviated in accordance with *The World List of Scientific Periodicals*. e.g., *et al., J. of Food Sci.*
For weights and measurements, and where appropriate, abbreviations rather than words are to be used, e.g., cm, mm, m, km, cc, ml, g, kg, min, %, etc., Fig.
Latin abbreviations such as: *op. cit., loc. cit., ibid.,* are to be in italic (if they are used).
6.**References:** References are mentioned numerically [between brackets] in the text and a list of references are provided at the end of the manuscript as follows:
a- Journals: [number] followed by the last name of the author (authors), First name or abbreviation, "paper title" , journal title , volume and issue numbers, (the year of publications between parentheses) , and page numbers.
Example: Sawyer, D. A. "Pounding of Rainwater on Flexible Roof Systems," Proceedings ASCE, Journal of the Structural Division, Vol. 93, No. 1, (1967), pp.127-147.
b- Books: Book references must include author, book title, the publisher's location, and publisher, and the year of publication.
Example: Feld, J., and Carper, K., Construction failure, 2nd Ed., New York, Wiley, 1997.
7. **Content Note or Footnote:** A content note or footnote is a note from the author to the reader providing clarifying information. A content note is indicated in the text by using a half-space superscript number (e.g. … books[3] are …). Content notes are to be sequentially numbered throughout the text. A reference may be cited in a content note by the use of the standard (Author, Date) style in the same way they are used in the text.
Content notes are to be presented below a solid half-line separating them from the text of the page in which the footnote is mentioned (in single column). Use the same half-space superscript number assigned in the content note(s) in the text to precede the content note itself.
8. **Proofs:** No changes, additions or deletions will be allowed in the pageproof stage.
9. **Opinions:** Manuscripts submitted to the Journal for publication contain the author's conclusions and opinions and, if published, do not constitute a conclusion or opinion of the Editorial Board.
10. **Offprints:** Two copies of the journal and twenty reprints of the accepted papers will be sent to the authors.
11. **Correspondence:** All correspondence may be addressed to:

E-mail: quecjour@qec.edu.sa

12. **Frequency:** …Two issues per year…….

Subscription and Exchange:

E-mail: quecjour@qec.edu.sa

In The Name of ALLAH,
Most Gracious, Most Merciful

Qassim University Scientific Publications

(Refereed Journal)

Volume (5) – NO.(1)

Journal of

Engineering and Computer Sciences

January 2012 – Safar 1433H

Scientific Publications & translation

Deposif: 1429/2023

Qassim University, College of Engineering, P.O. Box: 6677 Buraidah 51431
quecjour@qec.edu.sa

Journal of Engineering and Computer Sciences
Qassim University, Vol. 5, No. 1, PP 1-94, for English (January 2012/Safar 1433H.)

Contents

Page

Journal of Engineering and Computer Sciences
Qassim University, Vol. 5, No. 1, pp. 1-19 (January 2012/Safar 1433H)

Improving Geotechnical Properties of Dune Sands through Cement Stabilization

Awad AlKarni[1] and Sherif M. ElKholy[2]
[1]*Engineering College, King Saud University, KSA, awad.alkarni@gmail.com*
[2]*Engineering College, Qassim University, KSA, On leave from Construction Research Institute, National Water Research Center, Egypt, selkholy@qec.edu.sa*

(Received 18/6/2011; accepted for publication 17/2/2012)

ABSTRACT. When designing and constructing highways or more generally any super structures on dune sands type of soil, it is essential to make sure that the foundation soil is stable and provides good support to the applied loads. Dune sands soil are known to spread in huge areas throughout the kingdom of Saudi Arabia in which thousands of miles of new roads and highways are being constructed every year. Replacing such kind of weak soil is not an economically feasible alternative since it is very costly; besides, the replacement soil is not always available in nearby sites. This study discusses the possibility of dune sands soil stabilization using Portland cement as the stabilizing agent. Various ratios of cement content mixed with dune sands are used to examine the improvement of engineering properties of dune sands in terms of strength characteristics, and shear strength parameters. The results indicate that mixing dune sands with cement stabilizing agents would influence the engineering properties of treated soil. It is determined that the cement stabilization of dune sands improves the strength characteristics of the treated soil so that it becomes usable as a base material for roads construction and proper foundation material for other types of super structures. It was also determined that a cement content more than 9% may not probably cause any additional improvement for the stabilized soil. A suggested relationship is introduced to predict the values of initial tangent elastic modulus for such type of cement-treated dune sands.

Key words: *Dune sands, Cement stabilization, soil improvement, Shear Strength Parameters.*

1. INTRODUCTION

Saudi Arabia as many of the Gulf countries has witnessed extensive development programs and urbanization in the last few decades. These unprecedented construction activities throughout Saudi Arabia included constructing an internationally recognized network of highways to serve the newly developed areas of the kingdom. Thousands of miles of new roads, highways and airport runways are being constructed every year in addition to newly developed societies and cities. All these activities revealed some constructional problems which have been attributed to the poor quality of soil profiles in these areas. It was found out that the soil profile in such areas consists mainly of thick layers of fine to medium, non-plastic, wind-blown sand deposits, known as dune sands. This type of soil is usually characterized with its poorly graded fine grained materials with low bearing capacity and shear strength. These properties encouraged researchers and engineers to investigate the possibility of improving these deposits through stabilization techniques.

In Saudi Arabia, sand is the predominant type of soil exists almost in all soil profiles, particularly at the shallow levels. The sandy soil usually exists in two forms; dune sand and beach sand; both of which are somewhat Aeolian in nature [1]. These Aeolian deposits have an excess of fines and exist in a rather loose state and are often mixed with soluble salts that act as a cementing agent. This soil also has high potential to collapse due to the nature of its texture and grains structure. The shallowness of the groundwater alters the compressibility of this soil and can lead to fines migration and cause instability problems. The high variation of this soil strength and compressibility leads to the possibility of differential settlement under loads. Some of the problems which resulted from founding on such soil layers have been reported in the literature. As reported in [1] and [2], the formation of depressions zones and settlements in newly constructed roads. Other typical problems associated with the abundance of sands in arid and semi-arid areas can be summarized as continuous sand movement, and ground surface erosion and dust clouds [3]. The continuous movement of dune sands, wind or rain blown, causes abrasion for existing structures and blockage of streets and highways [4]. This sandy soil cannot be used as a foundation material in their natural condition due to its loose structure and vulnerability to collapse upon wetting [5]. For the same reasons, these soils are not suitable for construction of landfill liners and covers. However, when improved, they can be utilized in many applications.

Stabilization of such soils has become a trend nowadays and several stabilization alternatives have been tried over the last few years. Mixing of desert sands with other materials such as natural clays, bentonite, cement-by-pass dust and incinerator ash were found to improve the sand properties so that it can be used to support structures and road constructions [6]. The improvement in engineering properties of cement-treated soils is believed to be mainly due to the hardening of cement in the presence of moisture and extension of curing period [7]. Results of stabilizing of fine sand with industrial by-products such as ground-granulated blast furnace slag, low-calcium fly ash and meta-kaolin were

reported in [8]. Miller and Azad [9] conducted a laboratory study to investigate the influence of soil type on stabilization with cement kiln dust. The study revealed that increases in the unconfined compressive strength (UCS) of soil occurred with the addition of CKD. Increases in UCS were inversely proportional to the plasticity index (PI) of the untreated soil. Baghdadi and Rahman [10] presented the effects of cement kiln dust (CKD) on the geotechnical properties of dune sand. In their study, sand was stabilized with various mix proportions and the geotechnical properties of the stabilized sand were investigated. The results obtained for the maximum dry density, optimum moisture content, unconfined compressive strength and CBR showed that the stabilized soil can be utilized as base materials in highway construction. Peethamparana et al. [11] investigated the influence of chemical and physical characteristics of cement kiln dusts (CKDs) on its suitability for soil stabilization through investigating various samples of soil/CKD mixture. They concluded that both the compressive strength and the temperature of hydration of the CKD mix can give early indications of the suitability of particular CKD for soil stabilization. Zhiming and Herrera [12] conducted an extensive laboratory and field testing program to evaluate the effectiveness of cement kiln dust (CKD) as a stabilizer for a limestone base material. The results of this study showed that CKD has promise to be a good stabilizer for the base material if it is used properly. The comparative performances of CKD and other traditional stabilizers such as lime, cement, and fly ash were also investigated during laboratory and field testing. The unconfined compressive strength (UCS) increased substantially when the dosage of CKD was increased. The dynamic modulus also increased substantially with addition of CKD. Conductivity and colorimetry tests indicated that sulfate content increased with the added amount of CKD. A low resistivity value of CKD-stabilized base materials indicated that they cannot be used as backfill material. The field pavement evaluation indicated that the lime-stabilized section exhibited the highest modulus, followed by the CKD-stabilized section.

AL-Abdul Wahhab et al. [13] conducted an experimental program to evaluate the feasibility of using blends of dune sand--crusher fines that were stabilized with emulsified asphalt in low volume roads in Saudi Arabia. They stated that dune sand treated with emulsified asphalt alone was weak and unstable. However, the addition of crusher fines and Portland cement improved the mix properties significantly.

It can be noticed from this published literature that the research interest was devoted mainly to investigate the improvement in the characteristics of stabilized dune sands regardless of the loading conditions. However, practically wise when saturated cohesionless soils are loaded; the rate of application of load affects its general behavior and the resulting deformation. If the loads are applied slowly; any induced pore water pressure will dissipate as the loading progresses. However, under quick loading conditions the opposite occurs; the induced pore water pressure increases and may actually cause sudden failure of structures. Thus when simulating these conditions in the laboratory, the soil engineering properties and strength characteristics of interest are those developed under undrained conditions. Examples of quick loading conditions include; blast loading within soil deposits and dynamic

loads due to earthquakes within the soil body, for which ground accelerations may be very high but of very short duration. Under most general earthquake loading conditions; cohesionless soils would be in undrained condition during loading and the stress/strain applications will be of cyclic nature. These undrained conditions may be simulated in the laboratory using the Triaxial loading tests which will be used herein to investigate the potential improvement in dune sands characteristics due to stabilization techniques. Portland cement is used in the current study since it has proven to be an efficient stabilizing agent in improving the inferior properties of sandy soils.

2. METHODOLGY

2.1 Tested Soil

The soil samples used for the current study are selected from local sites and are identified as uniformly graded white dune sands. The necessary laboratory tests were conducted on the soil in order to determine its physical and engineering properties. It was determined that according to the USCS classification system, this soil is classified as SP (poorly graded sand) and according to AASHTO system it is classified as A-1-b. In addition, standard compaction tests were conducted on samples of the sand and it was determined that the maximum dry density (MDD) is 18 kN/m^3 at optimum moisture content (OMC) of 9.91 %. Table (1) shows average values of the main physical and engineering properties of tested soil while Figures. (1) and (2) show the particle gradation and the compaction curves for the tested soil.

Table (1). Summary of the physical properties of the tested dune sands.

Physical and Engineering Properties	
Classification of soil	White, poorly graded sand (SP)
Specific gravity, Gs	2.67
Dry density (kN/m^3)	
γ_d max	18.0
γ_d min	15.65
Void ratio (e) max	0.7
Void ratio (e) min	0.48

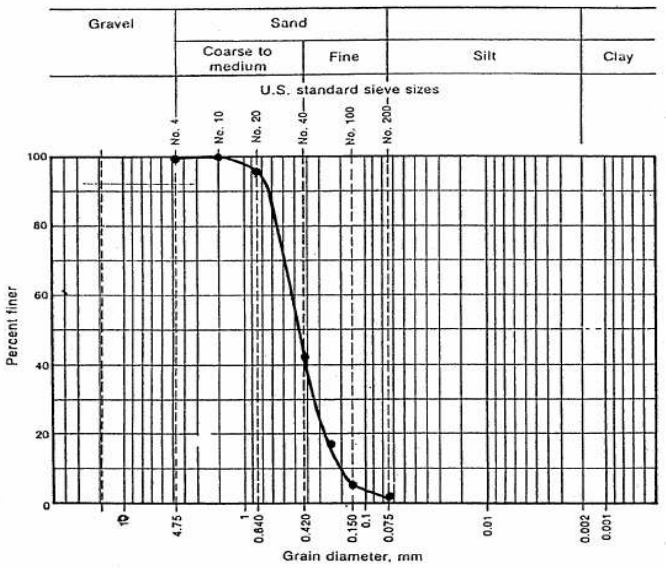

Fig. (1). Particle Gradation of the tested dune sands.

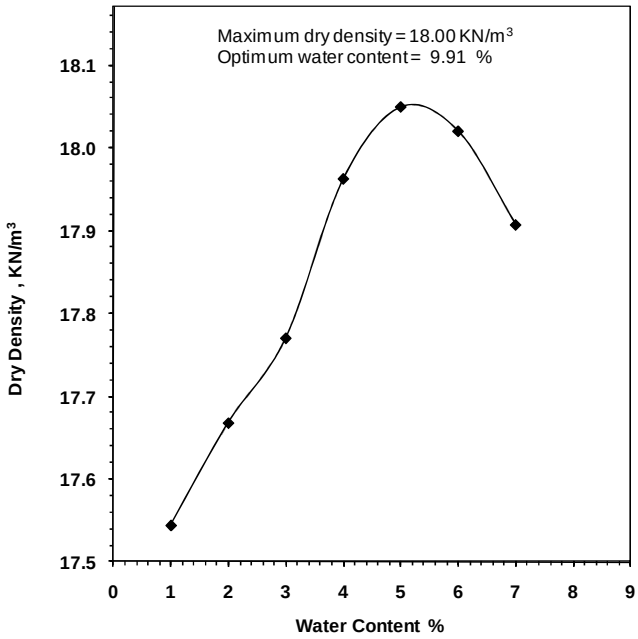

Fig. (2). Compaction curve for the tested dune sands.

2.2 Preparing Samples and Testing Procedure

The objective of the current study is to investigate the effect of cement stabilization on the strength characteristics of dune sands soil. To achieve that goal, a comprehensive Triaxial testing program is proposed utilizing the typical consolidated undrained conditions. The testing program aims to evaluate the strength of selected samples of stabilized dune sands under a constant pore pressure. A back pressure (U) is applied during the tests in order to maintain 100% saturation. The value of (U) is kept constant during the loading where the deviator stress is increased until the failure is reached; this procedure is repeated for different (σ_c). Different mixtures of sand with cement are prepared with cement content of 5%, 7%, and 9% by weight.

The mixture is prepared in dry conditions and then the water is added to the mix carefully. Mixing with water must be carefully observed, because there is a risk that the addition of water needed for hydration and compaction will wash the fine cement particles downwards through the permeable mass of dune sands. This would result in an inhomogeneous strength, or in other words, an excessively strong lower layer and a virtually unstabilized upper layer. This risk can be averted by adding the water to the soil before mixing in the cement. Preparing the mixture this way allows for cement hydration and mixture compaction; while at the same time observing the homogeneity of the sand-cement mixture. The used percentage of water is chosen based on preliminary tests where the mix workability is important. Compaction of cement treated soil must follow mixing stage as soon as possible, and certainly not more than two hours later because of the initial cement hydration reaction. Any source of water may be used, but sulphate-rich water should be avoided. The mixture is properly cured for three days before preparing the test samples. Curing of cement treated soil is conducted to avoid the loss of moisture before gaining mixture strength. It was found that the strength of cement-stabilized soil increase marginally with time of curing, but after 28 days should not merit consideration in design.

The Triaxial test samples are prepared according to ASTM standards. Samples size is 35.5 mm in diameter and 71 mm in height and they are compacted in the split mold in three equal layers to reach the desired density. The samples are set up in the Triaxial chamber; and a cell confining pressure of 40 kPa is applied. The sample is allowed to reach saturation (within 24 hours). Drainage valves are then opened and the confining pressure is increased to the desired value. The sample is allowed to consolidate under this confining pressure for 24 hours. Upon completing the consolidation stage, the desired value of back pressure is applied, which is kept constant during the test. The sample is then loaded at an axial strain rate of 0.3 mm/min, with full sample drainage permitted. The readings of axial load, axial displacement, and volume change are recorded continuously up to the sample failure. The recorded data are then analyzed; the soil shearing strength parameters and the necessary plots are prepared. Table (2) presents the details of the conducted testing program.

Table (2). Conducted testing program on the cement-treated sand.

Testing Series	Back Pore Water Pressure U (kPa)	Confining Pressure σ_c (kPa)	Cement Percent (%)
I	100	400 ،300 ،200	5
II	100	400 ،300 ،200	7
III	100	400 ،300 ،200	7

3. RESULTS AND DISCUSSION

The resulted data of the testing program which are herein discussed included deviator stress at failure, σ_d, initial modulus of elasticity (E_i), softening modulus of elasticity (E_p), reference stress (f_o), and the shear strength parameters (ϕ) and (C) (drained and undrained values).

3.1 Experimental Results

Figures (3) – (5) show typical results of the Triaxial testing program in the form of p-q curves, total Mohr's circles, and volumetric change behavior of the cement stabilized dune sands at various confining pressures.

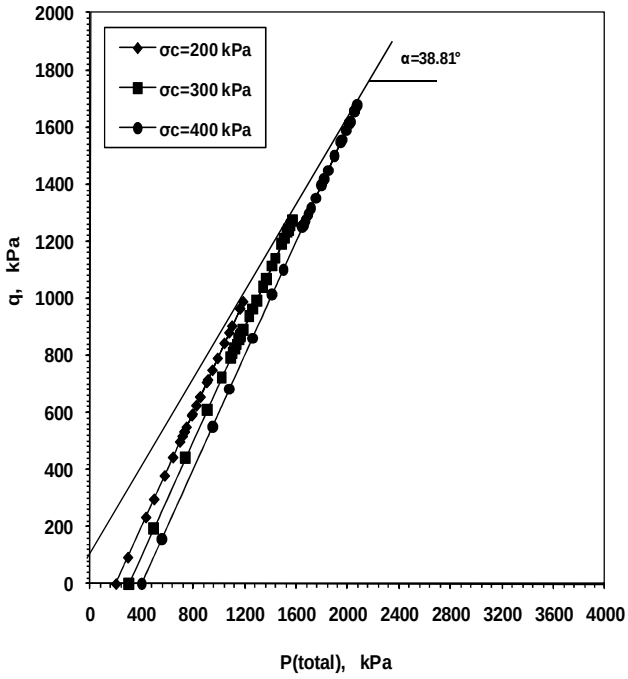

Fig. (3). pq curve for stabilized dune sands at various confining pressure (9% cement).

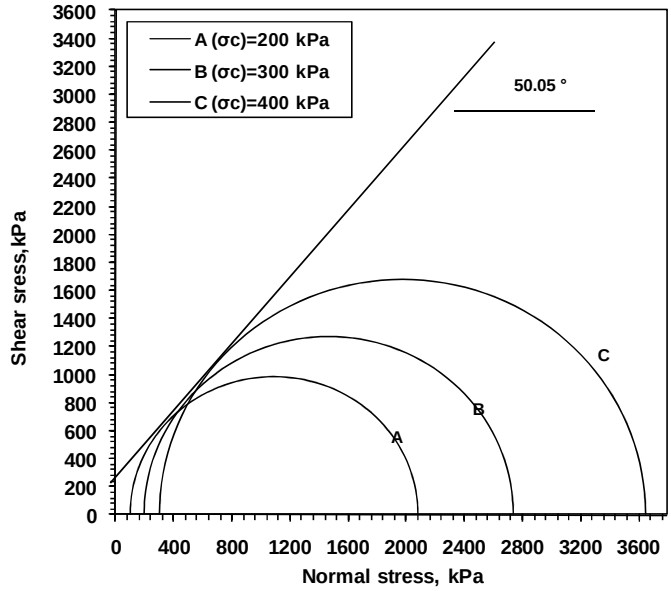

Fig. (4). Total Mohr's circle (9% Cement).

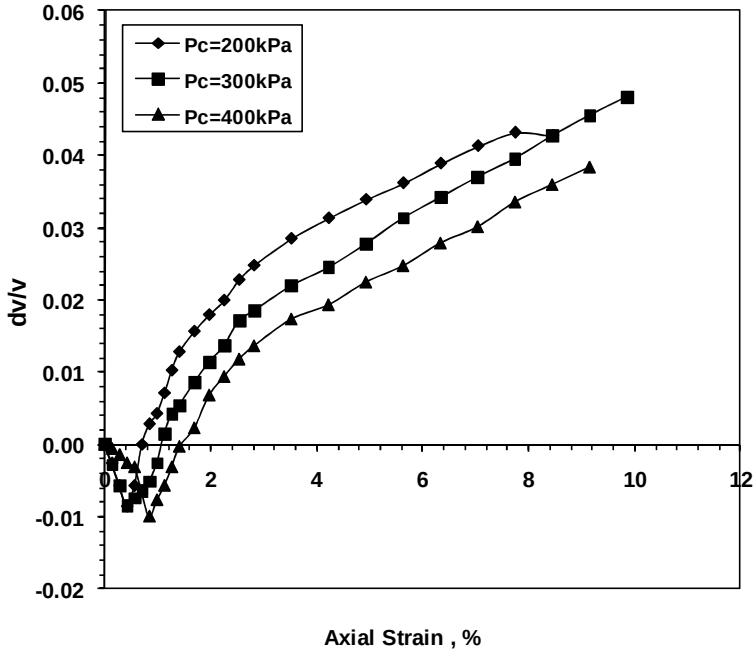

Fig. (5). Volumetric change behavior of cement stabilized dune sands (9% Cement).

3.2 Characteristics of Stabilized Dune Sands

From these results, the characteristics of the stabilized dune sands are presented in the following tables. Tables (3) – (5) show the resulted values for these parameters for the three prepared cement-sand mixtures of 5%, 7%, and 9% at different values of confining pressure and constant back pressure of 100 kPa. Tables (6) and (7) show a comparison of these values at the three sand-cement mixtures.

Table (3). Test results of cement-sand (5%) at different confining pressure and constant back pore water pressure U = 100 kPa.

P_c (kp)	σ_d (kPa)	E_i	E_p	f_o (kPa)	A	$'\alpha$	Φ	Φ'	C
200	1261.2851	818.5	191	1725					
300	1530.335	954.93	14.23	1820	33.62	32.8	40.91°	40.69°	120
400	2023.2259	1548.5	91.96	2230					

Table (4). Test results of cement-sand (7%) at different confining pressure and constant back pore water pressure U = 100 kPa.

Pc (kPa)	σ_d (kPa)	E_i	E_p	f_o (kPa)	A	$'\alpha$	Φ	Φ'	C
200	1604.8	958.33	33.3	1755					
300	1911.7	1166.7	37.3	2070	32.52	33°	40.7°	40.5°	195
400	2339.6	2000	37.03	2480					

Table (5). Test results of cement-sand (9%) at different confining pressure and constant back pore water pressure U = 100 kPa.

Pc (kPa)	σ_d (kPa)	E_i	E_p	f_o (kPa)	A	$'\alpha$	Φ	Φ'	C
200	1965.3	1000	185	2570					
300	2541.4	1125	175	2980	38.81°	38.2°	50.6°	50°	140
400	3350.3	2000	125	3645					

Table (6). Comparison of sand-cement mixture characteristics at different percentages of cement.

% of cement	σ_c (kPa)	σ_d (kPa)	E_i	E_p	f_o
5 %	200	1261.3	818.5	191	1725
	300	1530.355	954.93	114.23	1820
	400	2023.226	1548.5	91.96	2230
7 %	200	1604.8	958.33	33.3	1755
	300	1911.7	1166.7	37.3	2070
	400	2339.8	2000	37.03	2480
9 %	200	1965.3	1000	185	2570
	300	2541.4	1125	175	2980
	400	3350.3	2000	125	3645

Table (7). Comparison of sand-cement mixture strength characteristics at different percentages of cement.

% of cement	α	ά	Φ	Φ'	C
5 %	33.62	32.8	40.9	40.7	120
7 %	32.52	33	40.7	40.5	195
9 %	38.81	38.2	50.6	50	140

Figures (6) – (8) show the variation of the deviator stress σ_d with axial strain at different values of confining pressure (σ_c) for the stabilized soil. Figure (9) shows a comparison of deviator stress variation with axial strain for different percentages of cement stabilizer at a confining pressure of 400 kPa and a back pressure of 100 kPa.

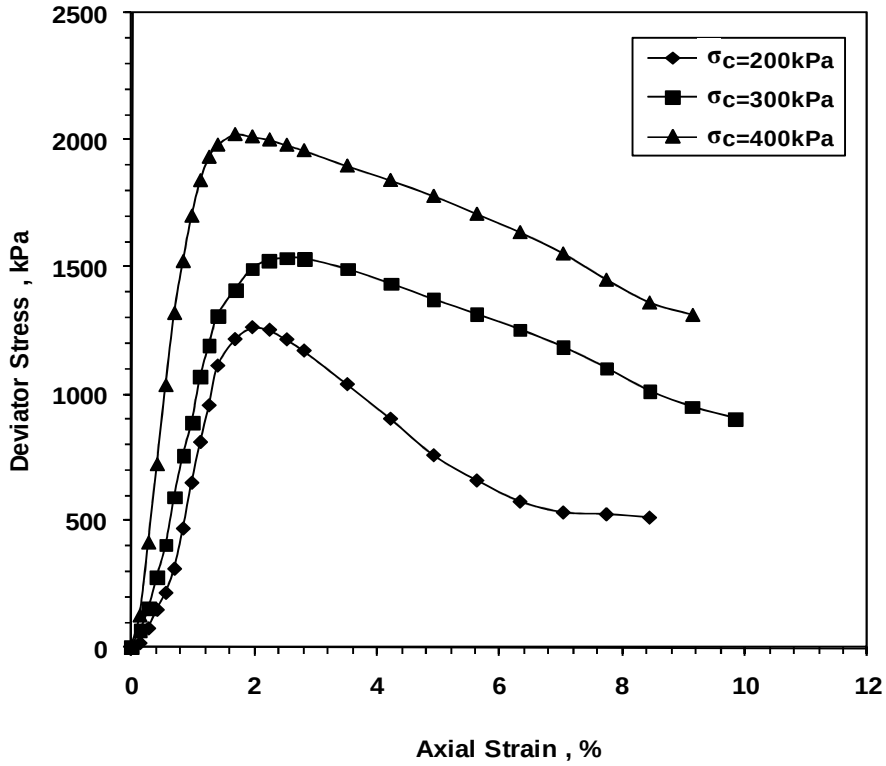

Fig. (6). Variation of deviator stress with axial strain for cement-sand mixture (5%) at different values of confining pressure σ_c.

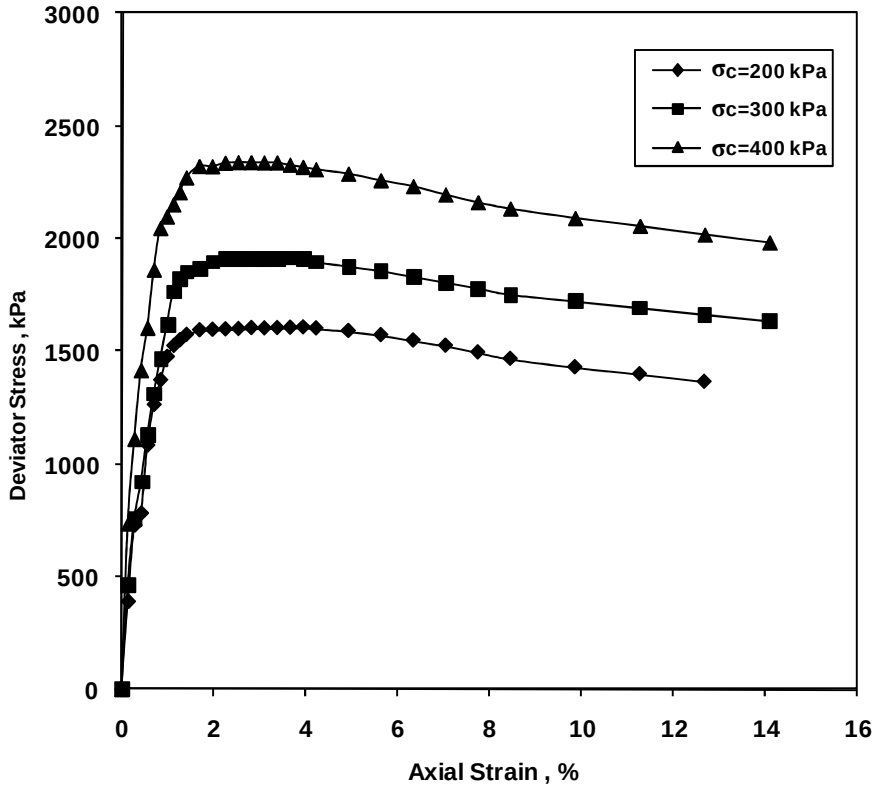

Fig. (7). Variation of deviator stress with axial strain for cement-sand mixture (7%) at different values of confining pressure σ_c.

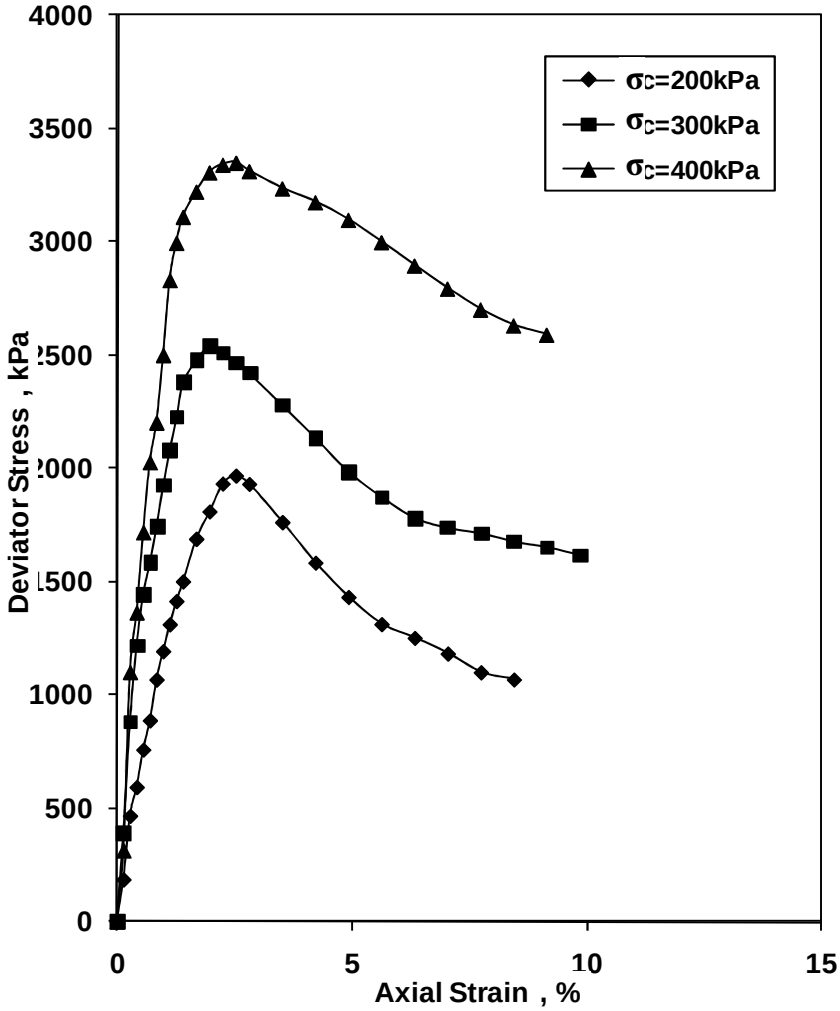

Fig. (8). Variation of deviator stress with axial strain for cement-sand mixture (9%) at different values of confining pressure σc .

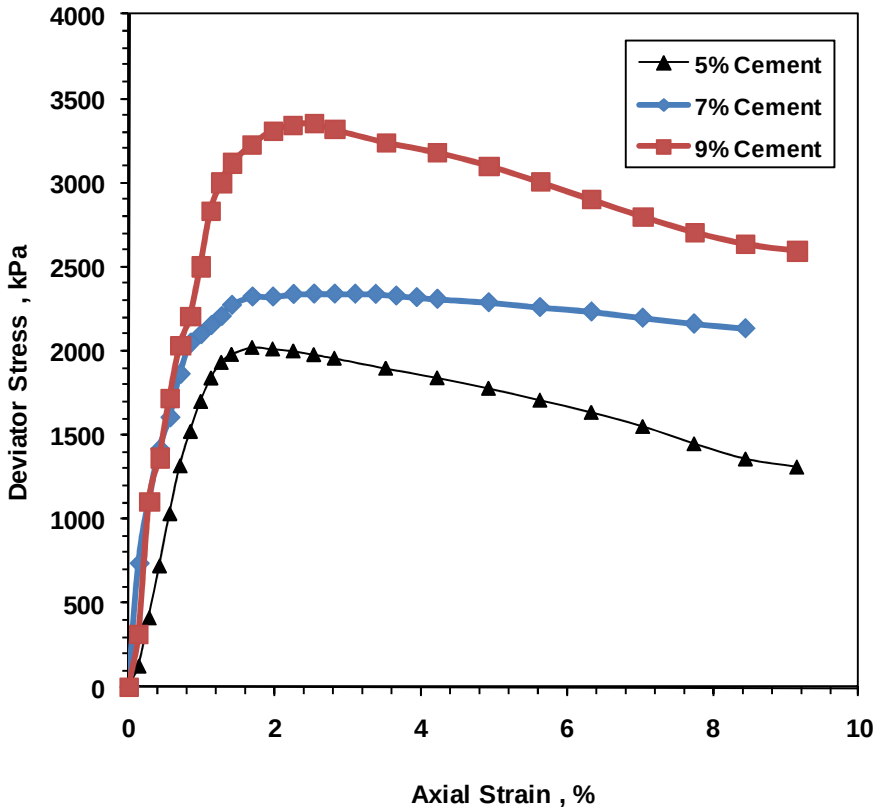

Fig. (9). Variation of deviator stress for various cement-sand mixing percentages.

The experimental results of the tested cement stabilized dune sands clearly show that the behavior of dense sand soil not that of loose poorly graded dune sands. The strength characteristics of the soil improved dramatically due to cement stabilization.

Looking at the results presented in Tables (3) – (7); one can find out that there is some kind of relationships among the strength characteristics of the stabilized soil. Figure (10) shows the variation of failure deviator stress with the confining pressure for the three cement content percentages (5%, 7%, 9%). While Figure (11) shows the variation of failure deviator stress with the change in cement content percentage in the stabilized soil at the different confining pressure and constant back pressure. Figure (12) shows the variation of initial tangent modulus with the variation of confining pressure at constant back pressure; noticing that the confining pressure as well as the initial tangent modulus are normalized by dividing them by the atmospheric pressure (102.3 kPa).

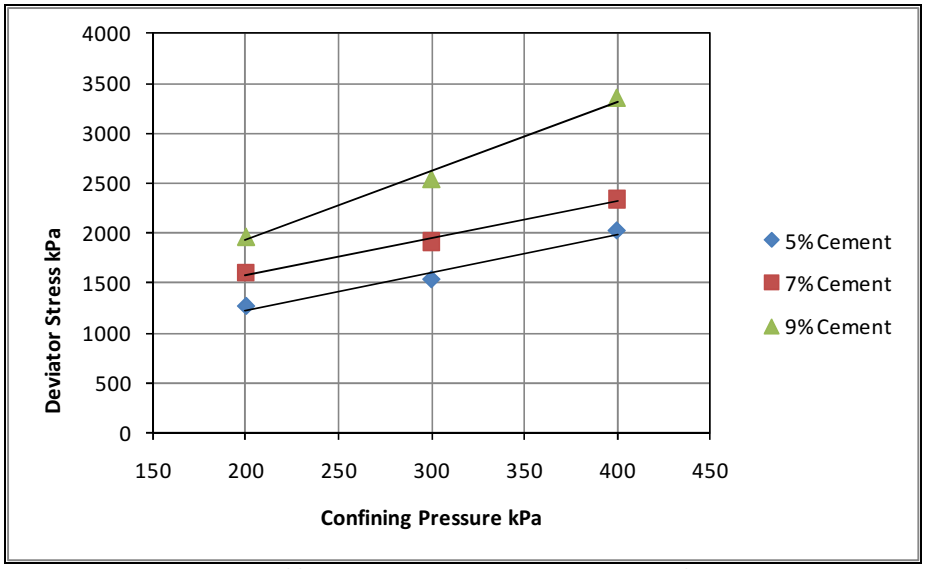

Fig. (10). Variation of failure deviator stress vs the change in confining pressure.

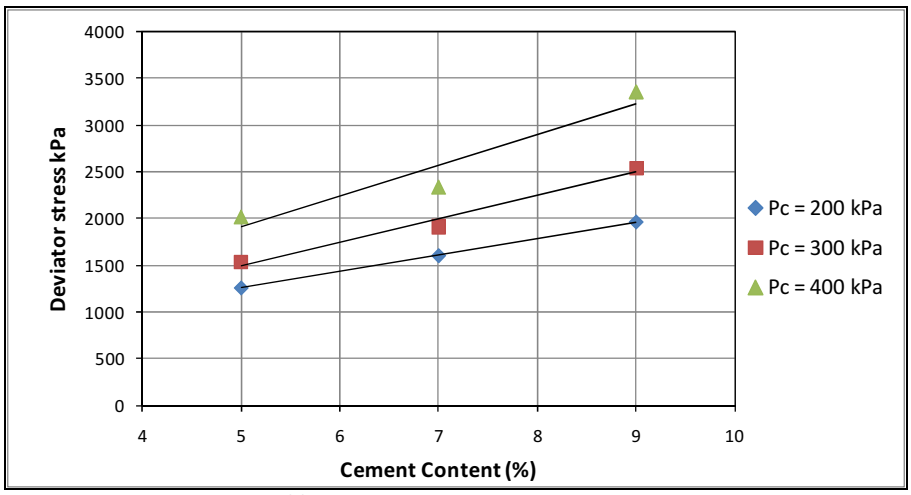

Fig. (11). Variation of failure deviator stress vs the change in cement content %.

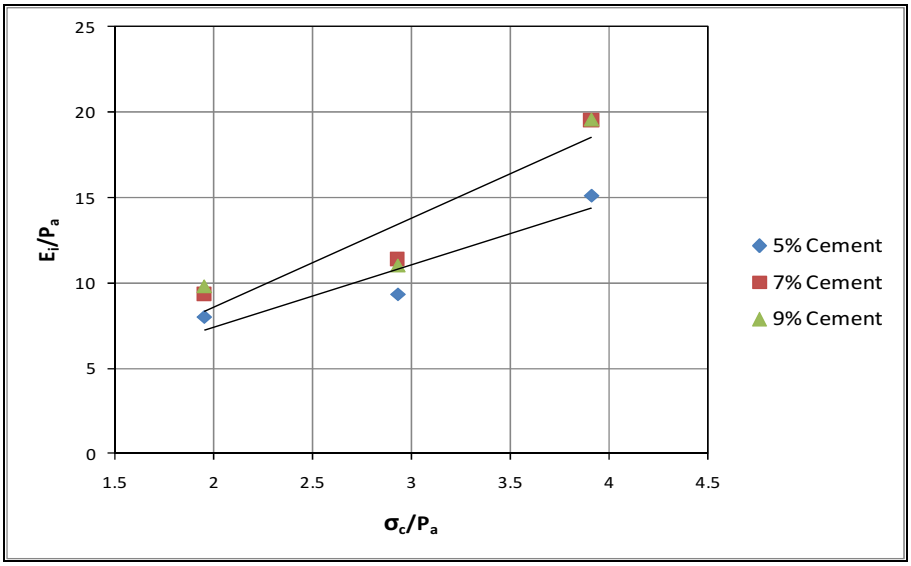

Fig. (12). Variation of failure deviator stress vs the change in cement content %.

From Figure (12); it may be noticed that the variation of initial tangent elasticity modulus with confining pressure did not change between 7% and 9% cement contents. This means that increasing the cement content more than 9% would probably not cause any more increase in the initial tangent modulus. Therefore, it can be used to introduce the following suggested equation to describe the relationship between them with a correlation factor $R^2 = 0.9$ (implying a strong correlation).

This equation can be used as a preliminary prediction for the values of E_i which can be used for the purpose of preliminary design and settlement calculations for this cement percent and should be checked for different mixtures with different types of dune sands.

4. CONCLUSIONS

The results of the testing program clearly show that the engineering properties of the dune sands soil improved considerably due to stabilizing with cement material. The deviator stress as well as volumetric change behavior shows similarity to those known for dense sand. The maximum deviator stress increases with the increase of confining pressure and the strength parameters of dune sands improved the most when mixing it with 9% cement. The resulted values of friction angles (Φ and Φ') are as high as those of the dense sand soil. Moreover, cohesion intercept values appeared; which also increases the shear strength of the cement stabilized soil. These improved shear strength parameters would considerably reduce the deformations and settlement under structures to acceptable and limited values and will help in reducing and optimizing the thickness of base materials under roads and

highways. The results also indicate that increasing the cement content above 9% may not probably improve the strength characteristics much more. However, other factors should also be investigated in order to examine its effect on the behavior of the treated soil, especially the effect of changing the value of the back pore pressure and the curing time before conducting the laboratory tests in order to reach the optimum treatment conditions. Moreover, the effect of cement stabilization on the values of soil CBR and MR should also be investigated for. These factors will be investigated and presented in future articles.

5. REFERENCES

[1] Aiban, S. A., "A Study of Sand Stabilization in Eastern Saudi Arabia", Engineering Geology, *Elsevier*, Vol. 38, (1994), pp. 65–79.

[2] AL-Abdul Wahhab, H.I. and Ramadhan, R.,"Prediction of Pavement Rutting in the Eastern Saudi Arabia", *Arabian J. Sci. Eng*., Vol. 15, No. 3, (1990), pp. 385-402.

[3] Stipho, A. S., "Aeolian Sand Hazards and Engineering Design for Desert Regions", *Quarterly Journal of Engineering Geology & Hydrogeology*; Vol. 25, No. 2, (1992), pp. 83-92.

[4] Al-Khanbashi, A., Mohamed, A. M. O., Moet, A., and Hadi, B., "Stabilization of Desert Sand Using Water-Born Polymers", Proceedings of the *First International Conference on Geotechnical, Geo-environmental Engineering and Management in arid Lands*, Al-Ain, United Arab Emirates, (2000), pp. 143-148.

[5] Elsharief, A. M., Mohamed Zein, Y. E. A., and Hussein, Y., "Geo-technical Properties of QOZ Soil", Proceedings of the *Twelfth Regional Conference for Africa on Soil Mechanics and Geotechnical Engineering*, Durban, South Africa, (1999), pp. 317-320.

[6] Mohamedzein, Y. E. A., Al-Aghbari, M. Y. and Taha, R. A., "Stabilization of Desert Sands Using Municipal Solid Waste Incinerator Ash", *Geotechnical and Geological Engineering*, Vol. 24, No. 6, (2006), pp. 1767-1780.

[7] Al-Aghbari, M.Y. and Dutta, R. K., "Suitability of Desert Sand Cement Mixes for Base Courses in Highway Pavements", *Electronic Journal of Geotechnical Engineering*, Vol. 10, No. 4, (2005).

[8] Buchwald, A. and Schulz, M., "Alkali-Activated Binders by Use of Industrial By-Products", *Cement and Concrete Research*, Vol. 35, No. 5, (2005), pp. 968-973.

[9] Miller and Azad, "Influence of Soil Type on Stabilization with Cement Kiln Dust", *Construction and Building Materials*, Vol. 14, No. 2, (2000), pp. 89-97.

[10] Baghdadi, Z. A. and Rahman, M. A., "The Potential of Cement Kiln Dust for the Stabilization of Dune Sand in Highway Construction", *Building and Environment*, Vol. 25, No. 4, (1990), pp. 285-289.

[11] Peethamparana, S., Olekb, J., and Lovell, J., "Influence of Chemical and Physical Characteristics of Cement Kiln Dusts (CKDs) on Their Hydration

Behavior and Potential Suitability for Soil Stabilization", *Cement and Concrete Research, Elsevier*, Vol. 38, No. 6, (2008), pp. 803-815.

[12] Zhiming, S. and Herrera, C. H., "Laboratory and Field Evaluation of Base Stabilization Using Cement Kiln Dust", *Transportation Research Record: Journal of the Transportation Research Board*, Vol. 19, (2007), pp. 42-49.

[13] AL-Abdul Wahhab, H., Bayomy, F., and Al-Halhouli, A., "Evaluation of Emulsified, Asphalt-Treated Sand for Low-Volume Roads and Road Bases", *Transportation Research Record No. 1106, Fourth International Conference on Low-Volume Roads*, Vol. 1, (1988).

تحسين الخصائص الجيوتكنيكية للكثبان الرملية عن طريق التثبيت بالأسمنت

عوض القرني[١] شريف الخولي[٢]

[١] *كلية الهندسة – جامعة الملك سعود –المملكة العربية السعودية-* awad.alkarni@gmail.com

[٢] *كلية الهندسة – جامعة القصيم –المملكة العربية السعودية - فى إجازة من معهد بحوث الانشاءات – المركز القومى لبحوث المياه – مصر* selkholy@qec.edu.sa

(قدم للنشر فى١٨/٦/٢٠١١م ؛ قبل للنشر فى ١٧/٢/٢٠١٢م)

ملخص البحث. عند تصميم أو إنشاء الطرق أو بصفة عامة أية منشأ على تربة من الكثبان الرملية، فمن البديهي أن تكون التربة ثابتة وقادرة على تحمل الأحمال المتوقعة من المنشأ. تنتشر تربة الكثبان الرملية هي العديد من مناطق المملكة العربية السعودية التي يتم فيها إنشاء آلاف الأميال من الطرق كل عام الكثير منها يمر ويؤسس على هذه النوعية من التربة الضعيفة. استبدال هذه التربة عادة غير مجدي لسببين أولهما اقتصادي نتيجة ارتفاع التكلفة، والسبب الثاني هو عدم توافر التربة البديلة في مناطق قريبة قى الكثير من الأحيان.

تناقش هذه الدراسة إمكانية تثبيت تربة الكثبان الرملية باستخدام أسمنت بورتلاند. تم خلط نسب مختلفة من الأسمنت مع تربة الكثبان الرملية واختبار مدى التحست في الخواص الهندسية للتربة الناتجة عن عملية الخلط من ناحية قوة التحمل ومعاملات القص لها.

أظهرت نتائج الدراسة أن خلط تربة الكثبان الرملية بالاسمنت يؤثر بصورة كبيرة على الخواص الهندسية للتربة المعالجة وتحسنها إلى حد كبير مما يجعلها مستقرة وقابلة للاستخدام كتربة أساس للطرق أو المنشآت التي تقام فوقها وذلك حتى نسبة أسمنت ٩٪ وبعدها لا يحدث أي تحسن إضافي للخواص الهندسية للتربة. تم اقتراح علاقة رياضية للتنبؤ بقيمة معامل المرونة المماسي لتربة الكثبان الرملية المعالجة بالاسمنت.

Journal of Engineering and Computer Sciences
Qassim University, Vol. 5, No. 1, pp.21-31 (January 2012/Safar 1433H)

Spectral Response Assessment of Rugate Filters Using the Perturbation Method of Multiple Scales

Mohammed H. Bataineh

Electrical Engineering Department, Faculty of Engineering, Qassim University
P.O.Box 6677 (Email: mohbat@qec.edu.sa)

(Received 25/2/2011; accepted for publication 17/2/2012)

ABSTRACT. This paper uses the perturbation method of multiple scales to obtain a closed form solution for the reflectance of rugate filters. The computational speed of the method is orders of magnitude higher than that of others. This allows studying the effect of filter's profile modifications and gives insight on the effect of the parameters involved. In addition to that, the method could be used to synthesis the spectral response of rugate filters.

Keywords: periodic structures, Optical waveguide filters, coupled-mode theory, multiple scales analysis.

1. INTRODUCTION

Rugate filters are used extensively as antireflection coatings. The usual procedure of calculating their spectral response is to utilize their stack counterpart. Thus partition the filter's profile to very thin layers and employ the *ABCD* characteristic matrix approach [1,pp.45]. As the number of partitions increases the number of multiplication required increases and thus a long computational time is needed. Methods proposed to alleviate this computation burden have been proposed by tackling the problem from periodic structure point of view. In [2], coupled-wave theory has been employed and gives results in agreement with the conventional characteristic matrix method. The drawback of applying this method is in using unclearly justified approximations. In addition to that, this method cannot easily be adapted to consider modulating the sine-wave profile with other slowly varying functions. This paper uses one of the small amplitude theories referred to as the perturbation method of multiple scales to analyze these types of filters. This is indeed one of the five different methods discussed in [3] for the analysis of mode coupling of two guided modes. The perturbation method of multiple scales was used in [4] to treat propagation of electromagnetic waves in corrugated waveguides. Its application to the present problem will not only give a fast and accurate method of evaluating and assessing the spectral response of an arbitrary refractive index profile, but also open the way forward for synthesizing the spectral response, which requires further exploration, however. In the next section, formulation of the problem in terms of the perturbation method of multiple scales is given. In Section 3, the incident and reflected interacting waves are derived. Some examples and validation of the method are presented in section 4.

2. FORMULATION

The problem being considered is the propagation of plane electromagnetic waves in a medium whose relative permittivity varies periodically with the depth of the structure, assumed to be L, as shown in Figure 1. The outer face and substrate are of refractive indices n_0 and n_s, respectively. The

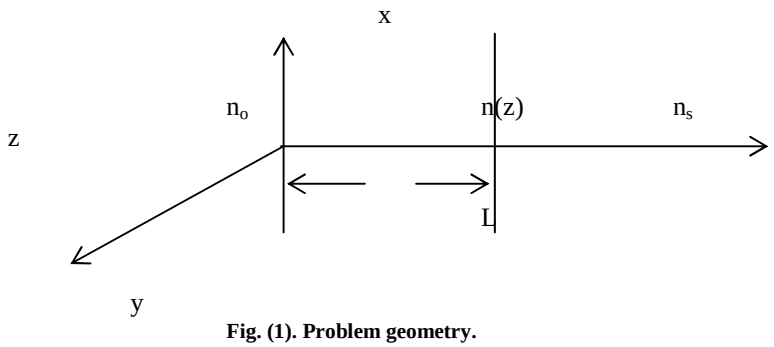

Fig. (1). Problem geometry.

The wave equation governing the electric field can be derived from Maxwell's equations and written as

$$\nabla^2 \vec{E} - \nabla \nabla \cdot \vec{E} + \omega^2 \mu_o \varepsilon_o \varepsilon_r(z) \vec{E} = 0 \quad (1)$$

A normal incident z-directed plane wave is considered with $\vec{E} = \hat{a}_x E_x(z)$. Substituting in Eq. (1) results in

$$\nabla^2 E_x + k_z^2 E_x = 0 \quad (2)$$

where:

$$k_z^2 = \omega^2 \mu_o \varepsilon_o \varepsilon_r(z)$$

or

$$k_z = \sqrt{\omega^2 \mu_o \varepsilon_o} \sqrt{\varepsilon_r(z)} = \tilde{k}_o n(z) \quad (3)$$

Here, n(z) is the refractive index of the rugate filter considered here to take a general form

$$n(z) = n_a (1 + \delta \sin (K_1 z))$$

Where n_a is the average unperturbed refractive index, δ is the perturbation index and K_1 is the wave number of the refractive index profile given by

$$K_1 = \frac{4\pi}{\lambda_1} n_a \quad (4)$$

λ_1 is the designed wavelength or wavelength at which peak performance is expected. Now k_z in Eq. (3) can be casted in the following form

$$k_z = \tilde{k}_o n_a (1 + \delta \sin (K_1 z))$$
$$= k_o (1 + \delta \sin (K_1 z)) \quad (5)$$

The governing equation (2) is a homogenous second order differential equation with variable coefficients whose solution is sought via the perturbation method of multiple scales.

3. WAVE INTERACTION EQUATIONS

The reflectivity or reflectance of a periodically varying refractive index profile is due to an interaction between incident and reflected waves. The derivation here is presented by expanding the field in powers of δ in the form

$$E_x(z) = E_x^{(0)}(z_o, z_1) + \delta E_x^{(1)}(z_o, z_1) + \ldots. \quad (6)$$

Where $z_o = z$ is a fast varying scale, and $z_1 = \delta z_o$ is a slowly varying scale. Expressing the derivatives in terms of z_o and z_1 by using the chain rule and substituting in Eq. (2), then equating coefficients of equal powers of δ to obtain

$$\underline{O(\delta^0)}$$

$$\frac{\partial^2 E_x^{(0)}}{\partial z_o^2} + k_o^2 E_x^{(0)} = 0 \tag{7}$$

$$\underline{O(\delta^1)}$$

$$\frac{\partial^2 E_x^{(1)}}{\partial z_o^2} + k_o^2 E_x^{(1)} = -2\frac{\partial^2 E_x^{(0)}}{\partial z_o \partial z_1} - k_o^2 \sin(K_1 z_o) E_x^{(0)} \tag{8}$$

Note that Eq. (7) corresponds to unperturbed system whose general solution is given by

$$E_x^{(0)}(z_o, z_1) = A(z_1)\, e^{-j k_o z_o} + B(z_1)\, e^{j k_o z_o} \tag{9}$$

Eq. (9) suggests propagation of two contra-directional traveling waves. The functions $A(z_1)$ and $B(z_1)$ are slowly varying functions representing the amplitudes of the incident and reflected waves, respectively. They are determined from the solvability conditions of the first order problem.

By substituting Eq. (9) in (8), we obtain

$$\frac{\partial^2 E_x^{(1)}}{\partial z_o^2} + k_o^2 E_x^{(1)} = j2k_o\left(A'(z_1) e^{-j k_o z_o} - B'(z_1) e^{j k_o z_o}\right) - \frac{k_o^2}{2j}\left(e^{j K_1 z_o} - e^{-j K_1 z_o}\right)\left(A(z_1) e^{-j k_o z_o} + B(z_1) e^{j k_o z_o}\right) \tag{10}$$

The primes denote differentiation with respect to z_1. Had we attempted a straightforward expansion (corresponding to $\frac{\partial}{\partial z_1} = 0$), we would found that it breaks down when the following resonance condition is satisfied

$$2k_o = K_1 \tag{11}$$

This is what is usually referred to as the Bragg condition. However, it is not necessary that this condition be valid exactly, it is sufficient if the phase $\pm j(2k_o - K_1)$ has a slow spatial variation. The nearness to resonance is measured by a detuning parameter α, defined by

$$2k_o - K_1 = \delta\alpha \tag{12}$$

Finding a particular solution of Eq. (10) would lead to secular terms; *i.e.*, solutions that are proportional to $z_0 e^{\pm jk_0 z_0}$. This means that $E_x^{(1)}$ would soon become greater than $E_x^{(0)}$ and, consequently, the perturbation expansion in Eq. (6) for E_x is not uniform and it breaks down. To eliminate the secular producing terms from the right-hand side of Eq. (10), we set the coefficients of $e^{\pm jk_0 z_0}$ equal to zero and arrive at the following solvability conditions for the first-order problem

Invoking the solvability conditions in Eq. (9) requires

$$j\,2k_o\;A'(z_1)+\frac{k_o^2}{2\,j}\,B\,e^{j(2k_o-K_1)z_o}\;=\;0 \tag{13}$$

or

$$\mathrm{A'(z_1)}\;=\;\frac{\mathrm{k_o}}{4}\;\mathrm{B\,e^{j\alpha z_1}} \tag{14}$$

and

$$-\,j\,2k_o\;B'(z_1)-\frac{k_o^2}{2\,j}\,A\,e^{-j(2k_o-K_1)z_o}\;=\;0 \tag{15}$$

or

$$B'(z_1)\;=\;\frac{k_o}{4}\;\;A\,e^{-j\alpha z_1} \tag{16}$$

Equations (14) and (16) are first order coupled equations with $\frac{k_o}{4}$ as a coupling coefficient. They can be solved using any standard differential equations solver to determine the amplitude reflection coefficient r, which is the ratio of the backward-propagating to the forward-propagating amplitude. However, to obtain a closed form formula for the reflectance, these two equations are decoupled by differentiating equation (14) and substituting from Eq. (16). The result is a second order differential equation given by:

$$A''-\,j\,\alpha\,A'-(\frac{k_o}{4})^2\;A=0 \tag{17}$$

Whose solution is given by

$$\mathrm{A(z_1)=e^{j\frac{\alpha}{2}z_1}\,(C_1\;e^{-\beta z_1}+C_2\;e^{\beta z_1})} \tag{18}$$

β in equation (18) is given by

$$\beta=\sqrt{\left(\frac{k_o}{4}\right)^2-\left(\frac{\alpha}{2}\right)^2} \tag{19}$$

The constants C_1 and C_2 are determined from the conditions imposed at the boundaries of the filter. The solution for $B(z_1)$ can be obtained from Eq. (14), and may be written as

$$\mathrm{B(z_1)=\frac{4}{k_o}\,[-C_1\,(\beta-j\frac{\alpha}{2})\,e^{-\beta z_1}+C_2\,(\beta+j\frac{\alpha}{2})\,e^{\beta z_1}]\,e^{-j\frac{\alpha}{2}z_1}} \tag{20}$$

Actually there is no need to impose two conditions to evaluate C_1 and C_2 since the amplitude reflection coefficient is given by the ratio of the backward propagating wave to the forward propagating wave of Eq. (9). To find the ratio of these two constants, we take the condition at the filter-substrate interface at z_o = L. The reflection coefficient, as defined above, when evaluated at z_o= L may be written also in terms of filter's refractive index profile at z_o= L and the that of substrate layer, i.e.,

$$r\Big|_{z_o=L} = r_s = \frac{n(L)-n_s}{n(L)+n_s} = \frac{B(\delta L)}{A(\delta L)}\, e^{j2k_o L} \tag{21}$$

Upon using Eqs.(18) and (20) into Eq. (21) one can obtain

$$\frac{C_2}{C_1} = \frac{\left(\frac{k_o}{4} r_s + (\beta - j\frac{\alpha}{2})\, e^{jK_1 L}\right)}{\left(-\frac{k_o}{4} r_s + (\beta + j\frac{\alpha}{2})\, e^{jK_1 L}\right)}\; e^{-2\beta\delta L} \tag{22}$$

The amplitude reflectivity at any point down the structure can now be written as:

$$r(z_0) = \frac{B(\delta z_0)}{A(\delta z_0)}\, e^{j2k_o z_0} \tag{23}$$

After some manipulation, Eq.(23) can be written in the following form

$$r(z_0) = \frac{-\left(\beta - j\frac{\alpha}{2}\right) + \frac{C_2}{C_1}\left(\beta + j\frac{\alpha}{2}\right) e^{2\beta\delta L}}{\frac{k_o}{4}\left(1 + \frac{C_2}{C_1}\, e^{2\beta\delta L}\right)}\; e^{jK_1 z_0} \tag{24}$$

The recursive Fresnel reflection formula [4] could now be used to find the reflection coefficient, ρ at z = 0:

$$\rho = \frac{r_a + r\Big|_{z_o=0}}{1 + r_a\, r\Big|_{z_o=0}} \tag{25}$$

Where r_a is the reflection coefficient at the outer interface, given by

$$r_a = \frac{n_0 - n(0)}{n_0 + n(0)} \tag{26}$$

The power reflection coefficient, or reflectance, is given by

$$R = \rho\rho^* \tag{27}$$

Various variations of the refractive index profile can be assessed by evaluating the reflectance, as defined in Eq.(27), with respect to the wavelength.

4. ILLUSTRATIVE EXAMPLES

To validate the method presented in this paper we use the same example given in [2]. The parameters used are 100 – cycle of rugate with $\delta = 0.05$, $\lambda_1 = 0.55$ μm, $n_s = 1.52$, and $n_o = 1$. The spectral response of power reflection coefficient, R, versus the wavelength, λ is shown in Fig. 2. The result is in excellent agreement with that given in [2] obtained in much less time when compared on the same machine. This example corresponds to uniform corrugation of rugate filter. Nonuniform corrugations could also be used. A variety of nonuniform perturbations can be studied and handled by the method. A notch–like response may be obtained by inverting the filter's profile at its mid-point. This is achieved by letting δ to take the form:

$$\delta(z_1) = \begin{cases} \delta_o & 0 \le z_1 \le \dfrac{L}{2} \\ -\delta_o & \dfrac{L}{2} \le z_1 \le L \end{cases} \tag{28}$$

The effect of this is shown in Fig. 3. Using the profile given in Eq. (28) means that a phase reversal at the middle of the structure has been made. This opens a narrow sharp transmission at the resonance wavelength. This is look a lot like the difference mode radiation pattern obtained in antenna arrays [6,pp.245.].

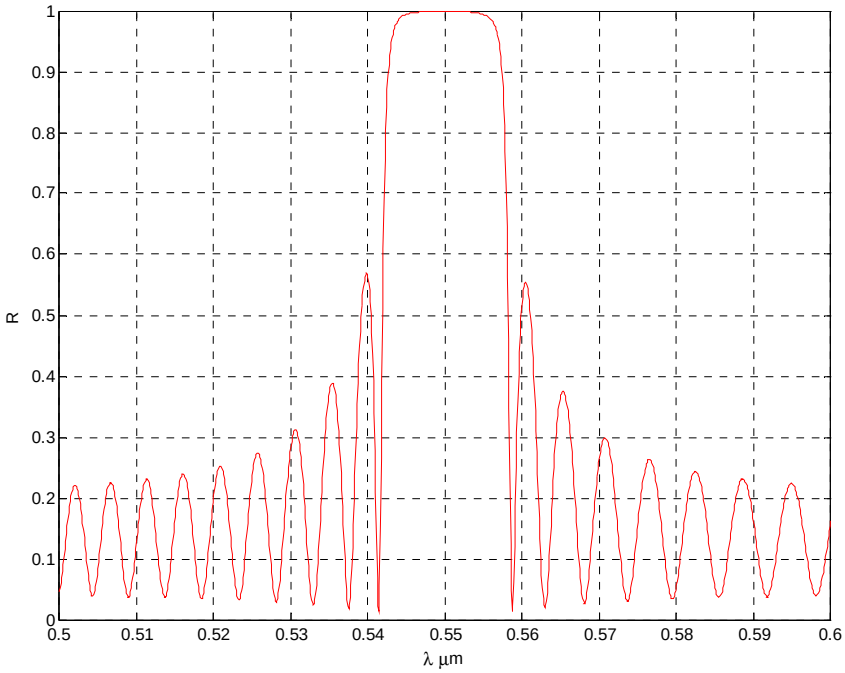

Fig. (2). Spectral response of uniform rugate.

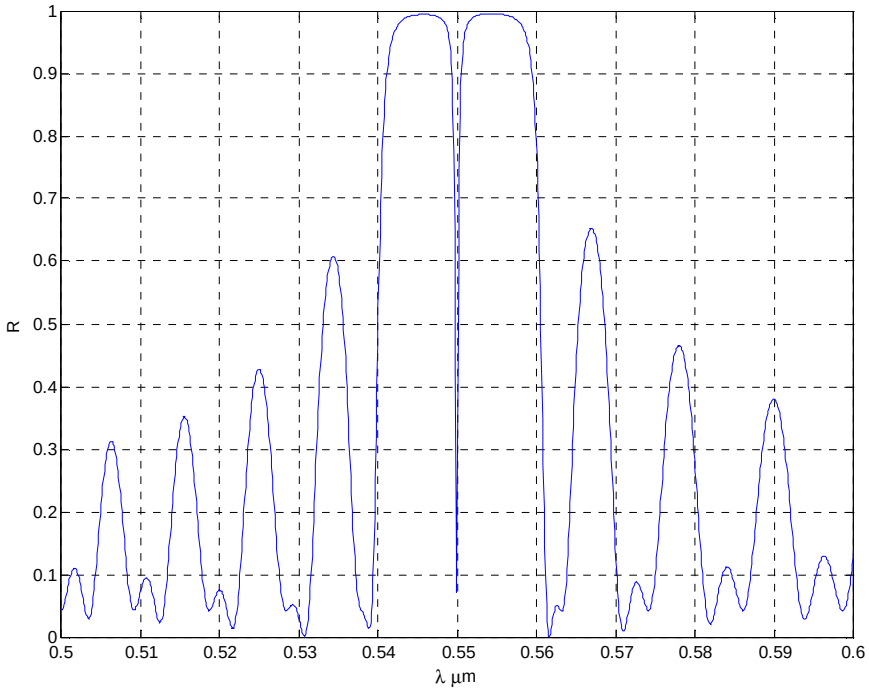

Fig. (3). Notch-like spectral response of nonuniform rugate.

5. CONCLUSIONS

Perturbation method of multiple scales can be used with arbitrary filter's profile to assess the response of rugate filters. In addition to its computational speed the method offers an alternative platform for synthesizing rugate filters. Important applications, notably wave division multiplexing, immerged by obtaining spectral response to suite the required application.

6. REFERENCES

[1] Macleod, A., *Thin-film Optical Filters,* UK, McGraw-Hill, (1989)**.**

[2] Southwell, W., "Spectral Response Calculations of Rugate Filters Using Coupled Wave Theory", *Journal of the Opt. Soc. of America*, Vol. 5, (1988), pp. 1558-1564.

[3] Seshadri, S. R., "Coupling of Guided Modes in Thin Films With Surface Corrugations", *J. Appl. Phys*., Vol. 63, No. 10, (1988), pp. R115-R146.

[4] Asfar, O. R., and Nayfeh, A. H., "The Application of the Method of Multiple Scales to Wave Propagation in Periodic Structure", *SIAM Review*, Vol. 25, (1983), pp. 445-480.

[5] Chew, W. C., *Waves and Fields in Inhomogeneous Media*, USA, IEEE Press, (1995).
[6] Stutzman, W., and Thiele, G., *Antenna Theory and Design*, USA, John Wiley, (1998).

تقييم الاستجابة الطيفية للمرشحات روجيت باستخدام أسلوب من قلقلة ذات مستويات متعددة

محمد حسين البطاينه

قسم هندسة الاتصالات، جامعة القصيم
mohbat@qec.edu.sa

(قدم للنشر فى ٢٠١١/٢/٢٥م ؛ قبل للنشر فى ٢٠١٢/٢/١٧م)

ملخص البحث. هذه الورقة تستخدم الأسلوب من قلقلة ذات مستويات متعددة للحصول على حل بشكل مغلق لانعكاس الطاقة من المرشحات rugate. السرعة الحسابية للأسلوب المتبع في الورقة أعلى من غيرها، وهذايسمح بدراسة تأثير التعديلات المطبقة على شكل المرشح كما يعطي فكرة عن تأثير العوامل المختلفه، ويمكن أن تستخدم هذه الطريقة لتصميم الاستجابة الطيفية للمرشحات rugate.

Journal of Engineering and Computer Sciences
Qassim University, Vol. 5, No. 1, pp. 33-51 (January 2012/Safar 1433H)

Virtual Power Producer and Consumer Agent Methodology for Optimal Management of Renewable Energy Resources

Hussein M. Khodr
Engineering College, Qassim University, Buraidah 51452, Saudi Arabia
khodr.hussein@qec.edu.sa

(Received 29/11/2011; accepted for publication 9/2/2012)

ABSTRACT. This paper proposes a Virtual Power Producer and Consumer Agent as a methodology aiming to optimize the integrated management of distributed renewable energy resources and to improve control Demand Side Management (DSM) and its aggregated loads. The paper presents a proposed method to coordinate the power generation technologies, the different load types, and the storage system. This method uses a framework based on data-mining techniques to characterize the customers load curve. The optimal power generation technologies dispatching of the smallest equipment of renewable energy resources and storage system is formulated as mixed-integer linear programming problem, due to the presence of the binary and continuous variables in the optimization problem. The model is coded in General Algebraic Modeling Systems (GAMS) and solved by High-performance mathematical programming solver for linear programming, mixed integer programming, and quadratic programming CPLEX solver. The application of methodology to a real case study in an isolated electrical service area in Portugal demonstrates the effectiveness of this method to solve the optimal isolated dispatch of the DC micro-grid renewable energy park. The solution has been converged in 0.09 seconds and 30 iterations.

Keywords: Renewable energy optimization; micro-grids; smart-grids; virtual power producers**.**

1. INTRODUCTION

The power and energy systems have been subjected to significant changes all over the globe in general. Portugal is not exonerated from these changes. Common rules have been established for many countries as well for Portugal in its internal electricity market. In this market the customers can freely choose their own electricity company suppliers, obviously according to their interests. Symmetric market allows electricity buyers to act as important agents in a perfect competitive environment. This fact indeed, requires load aggregators to obtain relevant knowledge concerning load consumption patterns and demand side-management or even demand response program opportunities. Elasticity demand can be the key issue for taking advantage of opportunistic strategies in the market place.

Strategic behavior based on elasticity demand requires consolidated knowledge concerning electricity consumers' performance. Knowledge about load consumption patterns is very important for load aggregators and electricity company suppliers, as it provides the basis for agreements concerning electricity prices, and for defining marketing policies and developing innovative contracts and services.

The characterization of electricity consumers' behavior relies not only on past consumption data, but also on consumption trends and strategies [1]. Historic data can be used to extract knowledge about consumption behavior by using adequate data-mining techniques. Consumption categories can be determined by using this data, the knowledge of costumers' behavior, and information involving issues such as activity type code, hired power value through contracts, and consumed energy [2].

The integrated management of Distributed Energy Resources (DER) can be achieved by implementing the Virtual Power Producer (VPP) concept [3]. The aggregation of loads in the scope of VPPs creates a new market agent structure, the Virtual Producer and Consumer Agent Methodology (VPCAM). The VPCAM provides the means to optimize the aggregated Distributed Energy Resources (DER), such as generation and storage, and to improve the Demand Side Management (DSM) of their aggregated loads.

This paper proposes VPCAM architecture and its function-based organization. Within this organization, the VPCAM uses a framework developed to characterize Medium Voltage (MV) and Low Voltage (LV) consumers, as a decision-support tool supporting the active and strategic participation of loads in the new liberalized electrical environment.

This paper presents the results of the mathematical optimization model and some experimental tests using the proposed architecture and methodology in real-world situations and considering real electricity generation and consumption data in an isolated area in Portugal.

2. PERSPECTIVE ENERGY PRICE IN THE SCOPE OF THE PORTUGUESE POWER SYSTEMS

The Portuguese Power System changed the primary resources of electricity generation by introducing a combined cycle of natural gas and, more recently, implementing new wind farms (in 2008, new wind farms with 576 MW of power were installed, increasing the total power of Portugal's wind farms to 2624 MW). In 2008, the production of the wind farms and the natural gas increased by 43% and around 20 %, respectively [4].

In contrast the production of coal thermal plants and fuel oil decreased by 11 % and 37%, respectively. Figure (1) shows the distribution of electricity production by technology and resource in Portugal. In 2008, two large photovoltaic plants were still in operation; the plant in the Amareleja region had a nominal capacity of 46 MW, and the plant in the Serpa region had a power output of 11 MW. As well, in 2008, a wave power plant with Pelamis technology and a power capacity of around 2 MW began operating in the Aguçadoura region. Electricity consumption is expected to increase by 1 %. To be prepared for this additional load, the Portuguese government is promoting an awareness campaign for an energy saving plan. This campaign has resulted in monetary saving and, therefore, has reduced in uncertain percentage of the government's expenses.

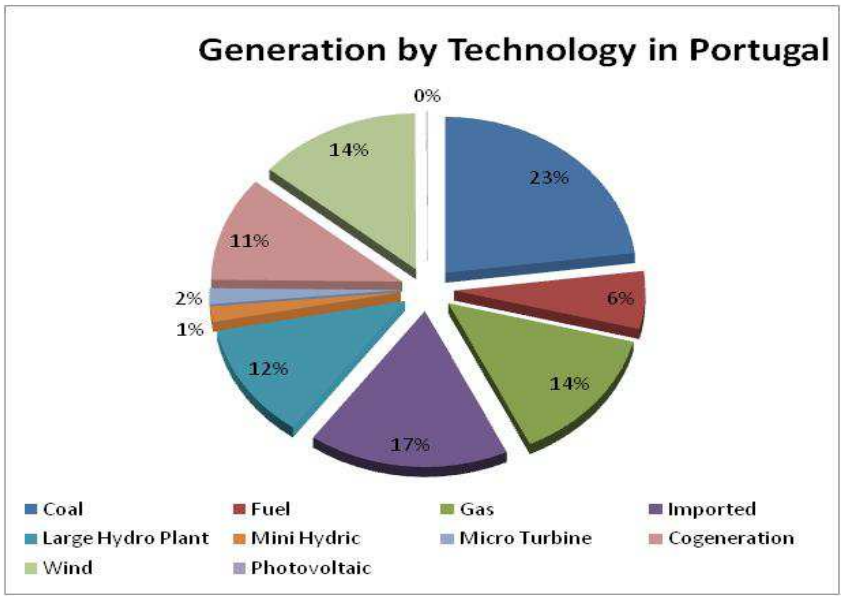

Fig. (1). Electricity production in Portugal by generation type.

Figure (2) shows the evolution of the monthly Portuguese consumption from 2006- 2008.

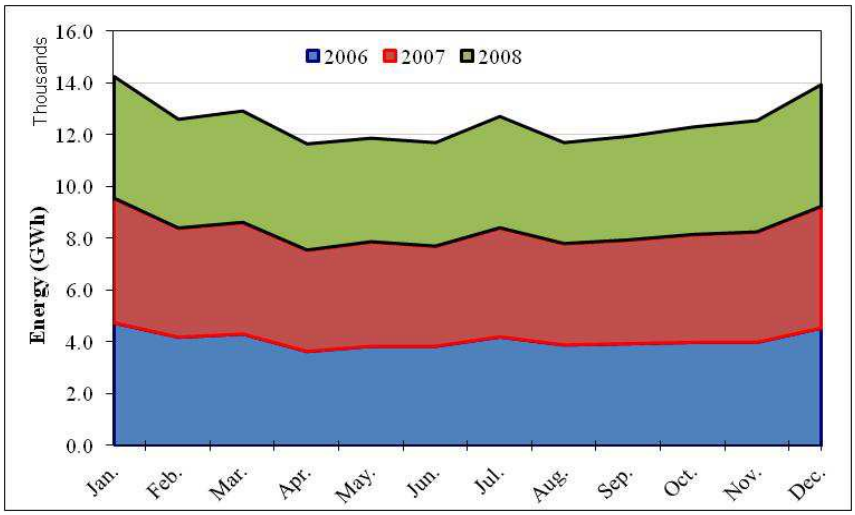

Fig. (2). Evolution Portuguese electrical consumption, 2006-2008.

The highest value of electricity power consumption was around 9 GW and occurred in the December of 2008.

The price of energy in Portugal is higher than the average price in the European Union countries, since the price of electrical energy in 2008 was 0.141 Eur/kWh for domestic consumers and 0.435 Eur/kWh for industrial clients [5].

Figure (3) depicts the evolution of the electrical energy prices in Portugal and 15 other countries in Europe.

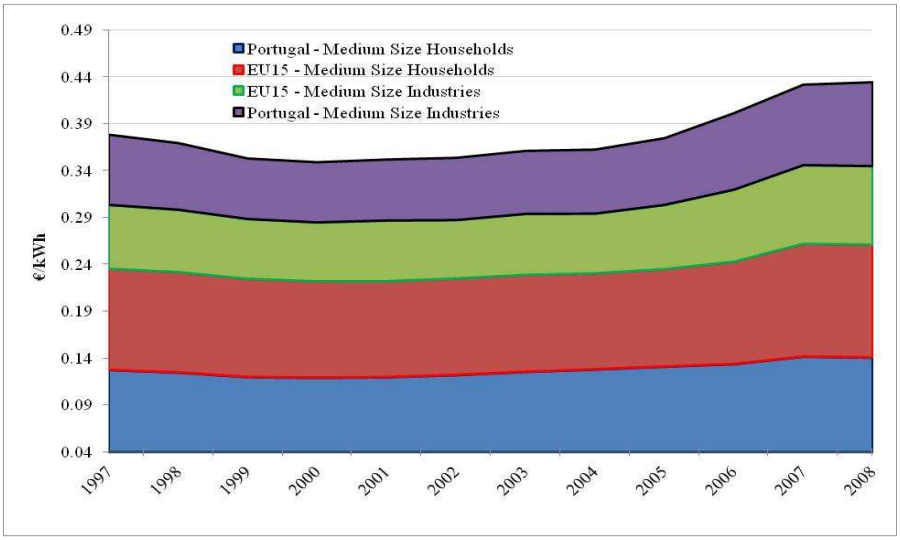

Fig. (3). Evolution of electric energy price in Europe, 1997-2008.

3. VIRTUAL PRODUCER AND CONSUMER AGENT METHODOLOGY (VPCAM)

With the liberalization of the power sector, electricity consumers can easily change their electricity-service contract from one electrical supplier to another. In this new environment, the market agents must provide new products and services offering attractive tariffs in order to take advantage of the competition opportunities. Choosing among several retailers could be a difficult task as contracts should be more flexible than they were previously, which can provide dynamic and therefore a fair contract management. Innovative and attractive contracts can provide different and flexible tariffs assuring a diverse quality of supply depending on the chosen tariff framework.

The electricity price is determined mainly by fixed costs, or the costs of generation, transmission and distribution, limiting retailer flexibility and the influence of customer behavior on electricity prices.

Currently, the Portuguese government and regional utility companies are working together to increase the influence of customers behavior and its impact on prices. An integrated vision of power generation and load demand, involving a set of power generation resources and loads, could provide the means to increase this influence positively.

The aggregation of distributed generation (DG) plants has resulted in a new concept: the Virtual Power Producer (VPP). VPPs are multi-technology and multi-site heterogeneous entities. VPPs can manage DG so that generators are optimally operated and the generated power has a good chance of being sold in the electricity market. Moreover, VPPs are able to commit to a more robust generation profile, raising the value of non-dispatched generation technologies.

In this context, VPPs can secure an environmentally friendly generation and optimal management of heat, cold and electricity together. They can also provide the means to ensure the optimal operation, the maintenance of generation equipment and, the electricity market participation. Aggregating loads as a consumer's agents to VPPs, resulting in a VPCAM, allows these entities to undertake the optimized integrated management of the aggregated DER and loads. Fig. 4 shows the VPCAM operation. The management of loads and power generation by the same entity allows new management strategies for DSM technique. With daily forecasting of power generation and consumption the VPCAM can coordinate several generation technologies and different load types and storage systems efficiently.

Another possibility for using VPCAM is in autonomous isolated systems disconnected from the main network. In these systems and in the isolated micro-grids, the power sources are limited to those inside the system, so that generation scheduling becomes increasingly important to satisfy the basic rule of the power system locally inside the isolated area [3].

In this system type, the most important power producers are the renewable energy sources, e.g., photovoltaic panels (PV), fuel cells, and wind turbines in combination with gas generators and cogeneration plants. These small power generations entity needs distributed and autonomous control for its correct performance. The use of small isolated power systems is also an attractive alternative for power utility companies, since these systems can help to improve the power quality and power supply flexibility and may increase reliability due to its availability in presence of faults. Also, they can provide a spinning reserve, ancillary services and reduce the transmission and distribution costs. Finally, these systems can be used to feed the customers in the event of an outage in the primary substation [6]. In order to characterize the consumers, the VPCAM should have an exact knowledge about when and how its clients consume electricity and their behaviors, as well as what electricity price has resulted from the market, and what generation has been forecasted in each considered time period.

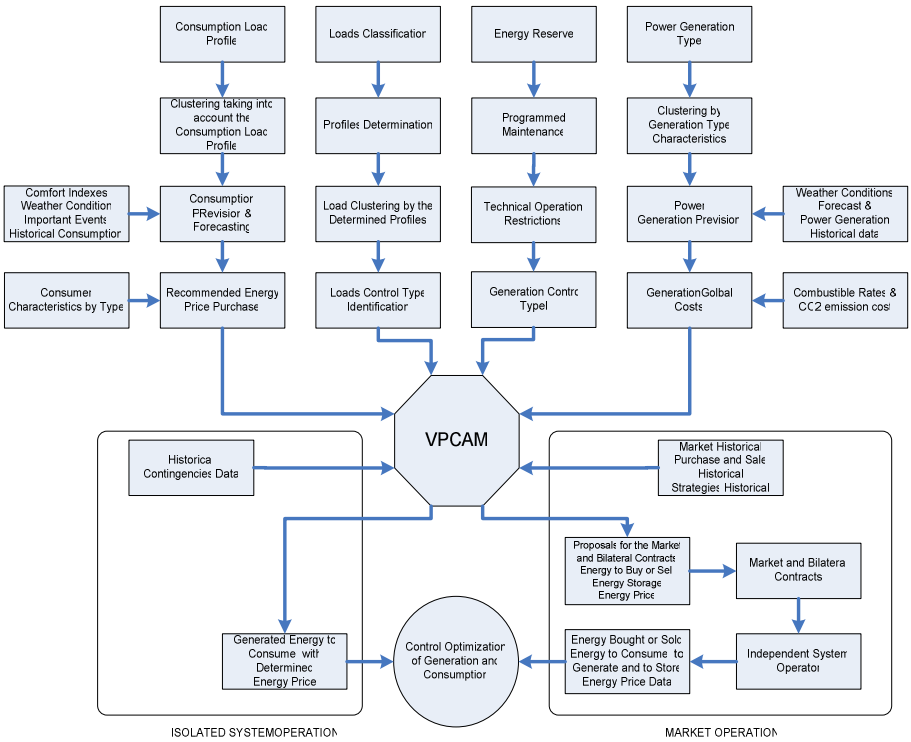

Fig. (4). Schematic representation of the functioning of a VPCAM.

The VPCAM should also identify the consumers who will be available to changing their electricity-consumption behavior taking into account the advantages which may be presented in term of price opportunities in the time period. A model can be used to determine the limited number of load profiles that are needed for resource management, as in cases of an energy shortage of determined loads. The major challenge here is the management for each considered time period the availability of the generated power during the considered time period, maximizing the reliability, so optimally handling the load curtailment decisions. Decisions must be based on the relevant knowledge of the consumers' behavioral characterization and its impact on the price in each time period.

4. CHARACTERIZATION PROCESS OF MEDIUM VOLTAGE CUSTOMERS

4.1 Customer clustering and classification

Figure (5) shows the study process for Knowledge Discovery in Databases (KDD) [7, 8, 9, 10].

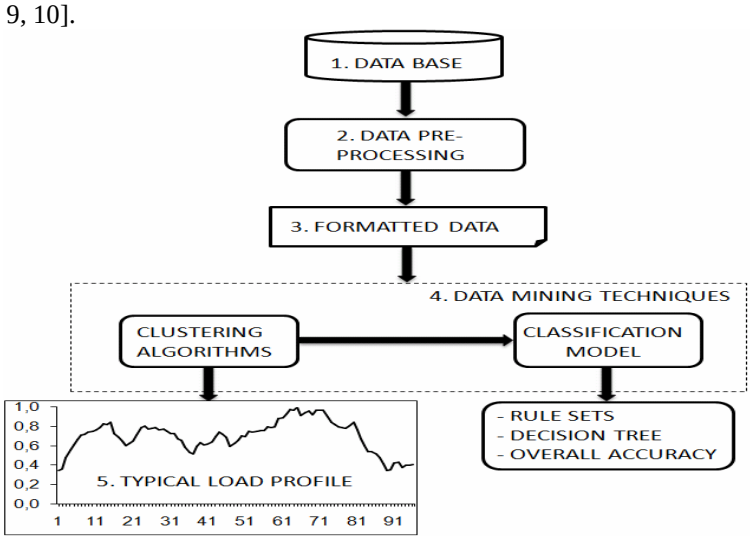

Fig. (5). MV consumer's characterization process.

The developed consumers' framework characterization used in this work is based on the process of Fig. 5. It includes several phases and uses Data Mining (DM) techniques in the calculation process. The framework is fragmented into different steps with different degrees of complexity: data and features selection, data preprocessing, formatted data, data mining techniques and the most important extracted knowledge.

DM techniques are used to characterize the typical customer profile, starting from an initial data set from a Portuguese utility [11]. The main goal of the consumer profiling is to group the data into classes so that the clusters of data in each class are highly similar and highly dissimilar to the clusters in other classes. With the new classification model, the new consumers can be placed in one of the known clusters according to their characteristics. By using a real data base released by the Portuguese distribution company with 229 MV customers, and collected during a period of 3 months in summer and the same period in winter for business days and weekends, the typical daily load curve of each customer was determined. Through data preprocessing action, 21 customers were discarded from the initial data, remaining 208 consumers to be analyzed. By using all the completed data, a representative load curve was obtained by averaging the daily load diagrams of each customer. Therefore, each customer is now represented by its typical load curve [11].

Figure (6) shows the representative business days load diagram obtained for each cluster, directly using the measured power [11].

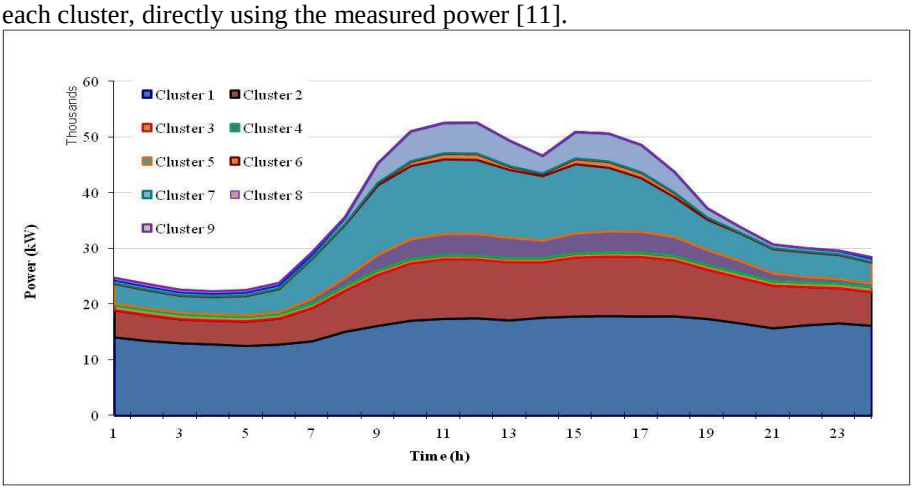

Fig. (6). Clusters obtained by using the two-step cluster algorithm for working days.

Each load curve depicts a cluster representing a customer group with the same consumption load pattern. Figure (7) shows the total amount of the electrical energy consumed by the 208 consumers considered in this case study.

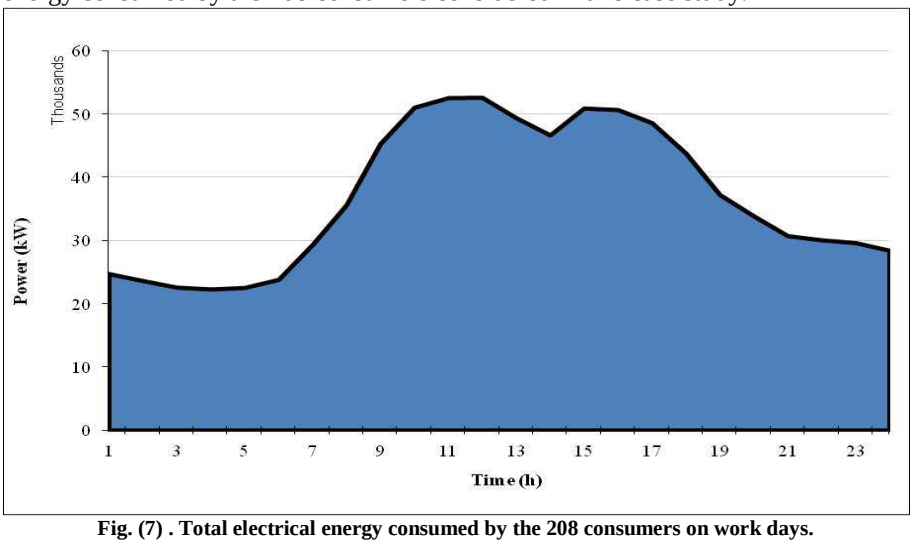

Fig. (7) . Total electrical energy consumed by the 208 consumers on work days.

4.2 Load Flexibility

Currently, the small isolated power systems are increasingly being used in the rural and remote electric service areas, instead of using only one centralized power

generation system and its corresponding large networks that are necessary to feed the remote electric loads.

Although the advantages of using small power systems are considerable, these systems are based only on renewable energy resources, which require the use of storage capability due to the intermittence characteristics to increase their power availability. The VPCAM can explore dynamic pricing during the day to take advantage of the customers' load profile modeling. Dynamic pricing includes the price value variation during the day reflecting the highest cost of the peak electricity generation usage. VPCAM, power producers and consumers should not miss this opportunity, but to take advantage of it, the electricity consumers must be prepared to change their consumption habits following the dynamic electricity prices. Thus, the consumers who are available to changing their electricity-consumption behavior must be identified.

Let us consider four different typical load profiles that will permit, in some way, changes in their consumption habits:

- Profile 1: This load does not allow for any load curtailment, independently of the time of the day. This profile applies to vital industrial producing processes and to emergency infrastructures such as hospitals and military sites.
- Profile 2: The load can alter its schedule according to operational constraints (e.g., generation shortage). This profile applies to some tasks that can be done at any hour of the day (e.g., using a washing machine).
- Profile 3: The load can be partially curtailed under the same conditions. This profile may apply, for instance, to lighting, air conditioning and heating systems (which can be reduced by 1 or 2 degrees), compressed air (which can be reduce by 0.5-1 bar in air pressure), and escalators.
- Profile 4: The load can be curtailed at any time of the day. The contract specifies what electrical circuits can be curtailed.

By using this approach and knowing each load profile, a VPCAM can manage all generation units and consumers' loads in order to achieve the established goals, which might be diverse (e.g., to guarantee power system stability, to increase profits of power producers, to reduce consumers costs tariff, or to reduce the global costs).

4. RENEWABLE ENERGY RESOURCES AND LOAD MANAGEMENT

The VPCAM aims to optimally manage all the available energy resources and loads in order to achieve the established goals. In order to do so, it needs relevant information to define the amount of energy generated by wind energy, photovoltaic energy, fuel cell, mini-hydro, Combined Heat and Power (CHP), and the storage battery power charging and discharging. Decision making requires accounting for the following considerations:

- The wind power generation strongly depends on the weather conditions. To have enough precision, the generation capability can be estimated for a period of only 24 hours in advance.

- The photovoltaic generation can be forecasted precisely.
- For fuel cells and CHP, the total generated energy is determined by the amount of the fuel.
- Mini-hydroelectric plants have a limited quantity of stored water and low generator capacity.
- Storage battery power discharging is limited by the maximal discharging capacity and existing storage energy.
- The loads are forecasted by considering several aspects; however, most of the loads can be controlled under only certain limits (using DSM – Demand Side Management). For each cluster, the VPCAM knows the loads which can be totally or partially curtailed or moved to a different time slice.
- To ensure system power balance, the VPCAM can determine the terms of reserve. For example, the VPCA can limit the minimum reserve to 10% of the forecasted load. This reserve can be assured by using storage and fuel cells.

The main objective is to carry out an optimal dispatch accounting for all the available energy resources, the forecasted load, the load profiles, and the relevant considerations. The surplus energy is used for charging the storage battery system. The different generation units' costs are considered. The optimal schedule of the demand and generation can be made for the envisaged time horizon (e.g., 5 minutes, 1 hours, 1 day, 1 week, 1 month or 1 year). For solving this mixed-integer constrained portfolio problem, the CPLEX solver supported by the GAMS platform was used [12].

The constraints of the problem were elaborated while considering five different operation modes [13]:

- A surplus energy that can be stored is available (as in the case presented in Fig. 8).
- The generation is not enough to assure the supply of the total load; therefore, the battery is discharged.
- In case of a lack of generation based on renewable sources (wind, water and/or sunshine) the battery, CHP and fuel cell come into operation (as in the case presented in Fig. 9).
- In case of insufficient energy generation, the load must be shed.

The objective function of the mixed-integer linear model is the minimization of the total cost for a given period (T) as follows:

$$Minimize\ f = \sum_{t=1}^{T} \left(\begin{array}{l} C^{(t)}_{W,Ph,Hy,CH,Fc} \cdot P^{(t)}_{W,Ph,Hy,CH,Fc} + C^{(t)}_{SBd} \cdot P^{(t)}_{SBd} + C^{(t)}_{\mathrm{R}} \cdot P^{(t)}_{\mathrm{R}} + \\ P^{(t)}_{LMP} \cdot C^{(t)}_{LMP} + C^{(t)}_{LS} \cdot P^{(t)}_{LS} + C^{(t)}_{NSE} \cdot U^{(t)}_{NSE} - C^{(t)}_{SBc} \cdot P^{(t)}_{SBc} - C^{(t)}_{E} \cdot E^{(t)}_{E} \end{array} \right) \quad (1)$$

Where: T is the period study, which may be one day, one week, one month or one year. In this case T is for 24 period of the one day. The methodology is prepared to be applied from the one year scheduling. C is the cost coefficient of each power generation type during the considered time period t. P is the power generation type.

Subscripts *W, Ph, Hy, CH, Fc* refer to wind, Photovoltaic, Hydroelectric, Combined Heat and Power and Fuel Cell power generation respectively. Subscripts *SBd, R, LM, LS, NSE, SBc, E* are Storage Battery discharge, Reduction, Load Shedding, Non Served Energy, Storage Battery charging and Excess respectively.

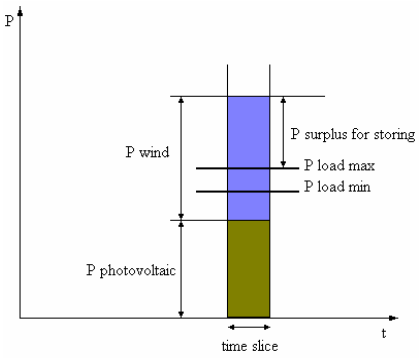

Fig. (8). Surplus of primary energy, adopted from [13]

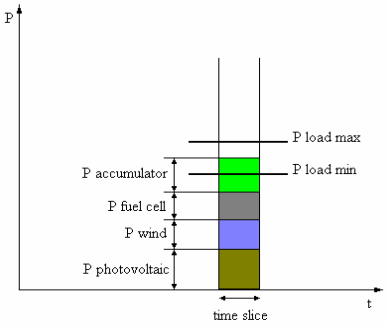

Fig. (9). The storage and the fuel cell in operation, adopted from [13]

Equation (1) is subject to the following technical constraints:

– First Kirchhoff Law or Power Balance

$$\sum_{t=1}^{T}\left(P_{W,Ph,Hy,CH,Fc}^{(t)}+P_{SBd}^{(t)}+P_{\mathrm{R}}^{(t)}+P_{LS}^{(t)}+P_{LMP}^{(t)}+U_{NSE}^{(t)}\right)=\sum_{t=1}^{T}\left(Load^{(t)}+P_{SBc}^{(t)}+P_{LMV}^{(t)}+E_{E}^{(t)}\right) \quad (2)$$

Where: Subscripts *LMP* and *LMV* are the Loads that have to be moved from the peak load curve and Loads moved to the Valley of load curve respectively.

– Wind, Photovoltaic, Hydroelectric, Combined Heat and Fuel cell Power generation limits in each time period "*t*". This constraint can be stated for each power generation type.

$$P_{W,Ph,Hy,CH,Fc}^{(t)} \le P_{W,Ph,Hy,CH,Fc}^{(t)}(\lim it); \quad t=1,...,T \quad (3)$$

– Storage battery limits in each time period "*t*"

$$P_{SB}^{(t)} \le P_{SB\ (Max)}^{(t)}; \quad t=1,...,T \quad (4)$$

Where: *SB* and $SB_{(Max)}$ are the Storage Battery and the Storage Battery .maximum respectively

– Storage battery maximal discharge limits in each time period "*t*"

$$P_{SBd}^{(t)} \le P_{SBd\,(Max)}^{(t)} \cdot X^{(t)}; \quad t=1,...,T;\ X=0 \ \ or\ 1 \quad (5)$$

Where SBd(Max) Is the Storage Battery maximum discharge .

– Storage battery maximal charge limits in each time period "*t*"

$$P_{SBc}^{(t)} \le P_{SBc(Max)}^{(t)} \cdot Y^{(t)}; \quad t = 1,...,T; \quad Y = 0 \ \ or \ \ 1 \tag{6}$$

– The battery cannot charge and discharge at the same time in each time slice "*t*"

$$X^{(t)} + Y^{(t)} \le 1; \quad t = 1,...,T; \quad X \ and \ Y = 0 \ \ or \ \ 1 \tag{7}$$

– Storage battery maximal discharge limits in each time period "*t*" considering the battery state storage in time period t-1

$$P_{BD}^{(t)} - P_{B}^{(t-1)} \le 0; \quad t = 1,...,T \tag{8}$$

– Storage battery maximal charge limits in each time period "*t*" considering the battery state storage in time period t-1

$$P_{BC}^{(t)} + P_{B}^{(t-1)} \le P_{BMax}^{(t)}; \quad t = 1,...,T \tag{9}$$

Where the subscripts BC, B and $Bmax$ are the Battery Charge, Battery and Battery Maximum capacity

– State balance of battery

$$P_{B}^{(t)} = P_{B}^{(t-1)} - P_{BD}^{(t)} + P_{BC}^{(t)}; \quad t = 1,...,T \tag{10}$$

– Initial state of the battery

$$P_{B}^{(t=0)} = P_{B}^{0} \tag{11}$$

For the succeeding time slices, the constraints are the same. The existing stored energy is updated between time slices.

5. CASE STUDY

The proposed methodology was applied to a real case study. The following prices were considered: wind energy cost 0.4 Eur/kWh; photovoltaic energy cost 0.4 Eur/kWh; hydroelectric energy cost 0.4 Eur/kWh; CHP energy cost 0.6 Eur/kWh; fuel cell energy cost 0.9 Eur/kWh; storage energy discharging cost 0.7 Eur/kWh; energy storage charging cost 0.4 Eur/kWh; load energy moving for a different time slice cost 1.2 Eur/kWh; load energy reduction cost 1.3 Eur/kWh; load energy curtailment cost 1.4 Eur/kWh; undelivered energy cost 1.5 Eur/kWh; and the excess of the generated energy is with cost 0 Eur/kWh, due to the Portuguese legislation that does not permit any generated energy injection into the main grid in these time, but now is under study by the specialized governmental entity to be permitted in the near future.

To illustrate the generality and the effectiveness of the proposed methodology, a scenario involving several energy resources was created. The data for this scenario are presented in Table I. The VPCAM has detailed information about not only the consumption of all customers, but also the characteristics of their loads pattern and the industry's electricity needs. The real electricity needs of all consumers must be known and understood in order to adequately manage all the available resources, including the use of DSM.

Solving the optimization problem allows the VPCAM to obtain the optimal renewable energy generation dispatch by accounting for the cost of each generation technology. Several simulations were performed in order to demonstrate the importance of considering the different load profiles. Figure (10) presents the obtained results for the load supply in a situation where all the consumers do not allow for load shedding independent of the time of the day. Fig. 10 reveals that an amount of undelivered energy is present in time slices 10 to 18.

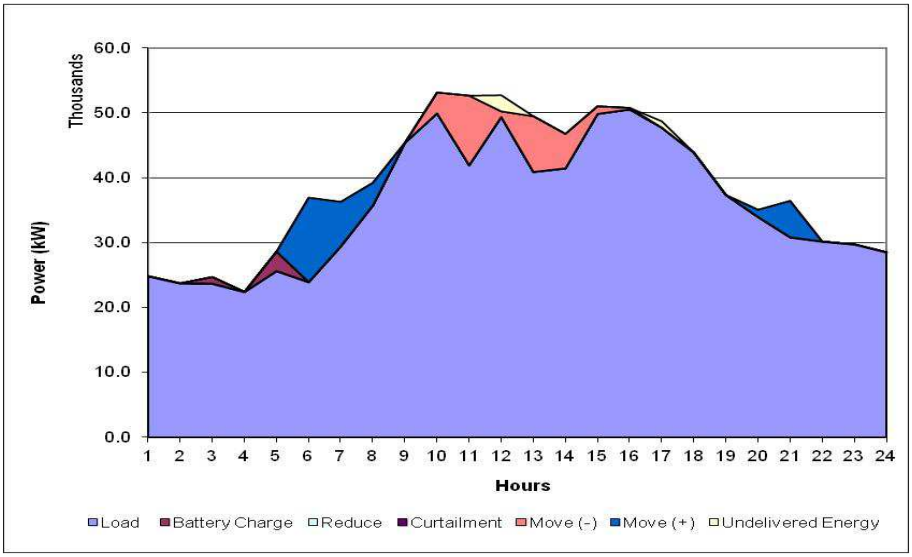

Fig. (10) . Energy consumption without consumption management.

Figure (11) shows the optimal generation scheduling for the same situation. By considering the contracts with all profile types, the VPCAM can manage the generation and consumption to reduce the undelivered energy to the important loads. For the same demand, the VPCAM will consider a set of contracts allowing for demand-side flexibility. By using the nine clusters obtained in Section III, the following profiles were considered:

- Clusters 2, 4 and 6 – Profile 1;
- Clusters 1 and 5 – Profile 1 and Profile 2;
- Clusters 3, 8 and 9 – Profile 1 and Profile 3;
- Cluster 7 – Profile 1 and Profile 4.

Fig. 12 shows the results for electricity consumption in this situation, revealing that the VPCAM was able to manage the resources so that no energy was undelivered for priority loads. Demand-side flexibility was achieved by moving a part of the load for off-peak periods and reducing and curtailing a part of the loads. The battery was charged in two periods.

Table (1). Estimated Power Generation and Consumption Forecast (kWh).

T.S	P_{W_1}	P_{W_2}	P_{W_3}	P_{PH}	P_{HYD}	P_{CHP_1}	P_{CHP_2}	P_{FC}	P_{S-1}	P_{SC}	P_{SD}	P_{CUT}	P_{RED}	P_{RED}	*LOAD*
1	6540	8760	8760	0	Storage water to 60000 ≤10000	≤10000	≤3000	≤5000	1000	≤3000	≤1500	0	282	0	24778
2	7810	9780	9780	0								0	285	0	23674
3	8120	7690	7690	0								0	279	0	22632
4	9130	7560	7560	0								0	268	0	22349
5	10040	6830	6830	0								0	261	0	22575
6	9760	6350	6350	0								0	261	0	23863
7	10130	5490	5490	0								0	259	0	29380
8	10250	7980	7980	50								0	224	0	35690
9	9760	8150	8150	140								1041	171	0	45383
10	9570	8490	8490	280								1611	159	0	51122
11	8790	8670	8670	540								1628	153	17410*	52640
12	6540	9050	9050	770								0	144	30865*	52704
13	7130	9890	9890	850								0	148	29376*	49464
14	7430	10100	10100	890								0	153	11639*	46736
15	7800	10400	10400	840								0	150	12488*	50997
16	6430	8960	8960	790								500	161	11475*	50752
17	6580	7890	7890	450								489	165	0	48684
18	5900	8760	8760	320								370	168	0	43863
19	5670	7650	7650	240								0	172	0	37300
20	6490	6780	6780	110								0	185	0	33923
21	7830	7100	7100	40								0	179	0	30783
22	8120	7560	7560	0								0	181	0	30128
23	8340	7890	7890	0								0	203	0	29689
24	8760	8150	8150	0								0	238	0	28477

*- The consumption of the energy in a time slice can be moved to time slices 7 to 10h or 18 to 20h

Figure (13) shows the optimal generation scheduling for the same situation. In this simulation, the consumers with the most impact on the results were those that allowed some electrical energy to be moved during the off-peak hours. The other

consumers were important for balancing the time slices with short difference between generation and consumption.

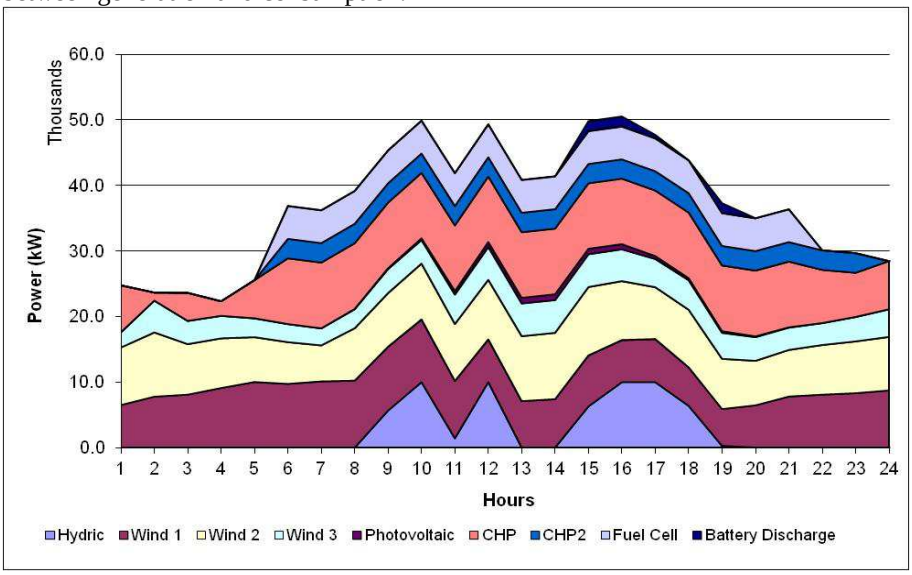

Fig. (11). Generation without consumption management.

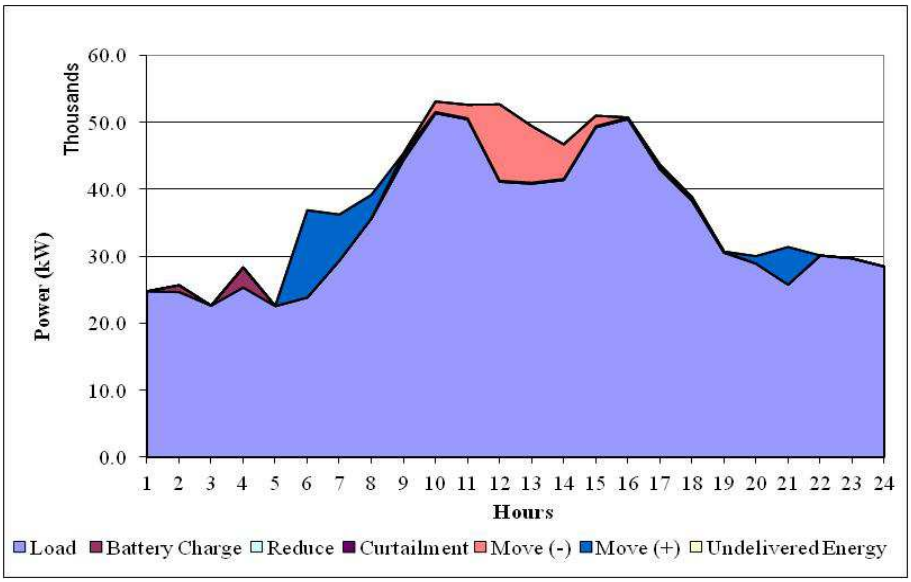

Fig. (12). Energy consumption by moving, reducing and curtailing some energy consumption.

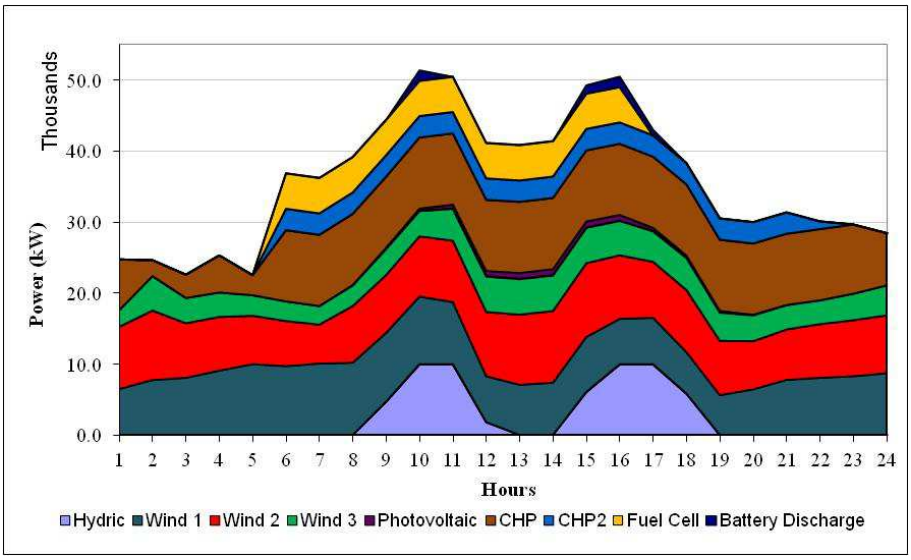

Fig. (13). Generation with moving, reducing and curtailing some electrical energy consumption.

6. CONCLUSION

This paper proposed a methodology to manage the operation of an isolated system by a Virtual Power Producer and Consumer Agent Methodology (VPCAM). The main goal was to minimize the total involved cost, which includes the generation costs, storage energy system charging and discharging costs, and demand-side flexibility use costs, subject to all the operational technical constraints. The VPCAM must assure a permanent balance between generation and consumption by undertaking the required load curtailment, when is necessary in an optimized way.

This paper presented the results of the application of the methodology to a set of real consumers' data. The dispatch was formulated as a mixed integer linear programming optimization problem and programmed and solved by using the GAMS platform and the CPLEX Solver, respectively. The obtained results demonstrate that the proposed methodology is effective and robust. It is also efficient as it requires only a brief execution time. The proposed method helps to minimize the operation costs by accounting all the available energy resources and the demand-side flexibility.

7. REFERENCES

[1] Praça, I., Ramos, C., Vale, Z., and Cordeiro, M., "MASCEM: A Multi-Agent System that Simulates Competitive Electricity Markets," *IEEE Intelligent Systems*, Vol. 18, (2003), pp. 54-60.

[2] Gellings, C. W., "Emerging Energy Customers of the Twenty-First Century," *CIGRE/IEEE Technical Session, IEEE Power Engineering Review*, (1998).

[3] Morais H., Kádár P., Cardoso, M., Vale, Z., Khodr H. M., "VPP Operating in the Isolated Grid," *IEEE PES General Meeting*, Pittsburgh, Pennsylvania, USA, 20-24 July, (2008).
[4] Redes Energéticas Nacionais (REN), "*Monthly Report Information – Power System Generation– Dec. 2008*", Portugal, Published (in Portuguese), January, (2009).
[5] http://epp.eurostat.ec.europa.eu (Eurostat).
[6] Milošević, M., and Andersson, G., "Generation Control in Small Isolated Power Systems," *37th Annual North American Power Symposium*, (2005).
[7] Figueiredo, V., Rodrigues, F., Vale, Z., and Gouveia, B., "An Electric Energy Characterization Framework based on Data Mining Techniques," *IEEE Transactions on Power Systems*, Vol. 20, (2005), pp. 596-602.
[8] Frawley, W.J., Piatetsky-Shapiro, G., and Matheus, C., "Knowledge Discovery in Databases: an Overview," Technical Report, (1995).
[9] Fayyad, U., Piatetsky-Shapiro G., Smith, P. J., and Uthurasamy, R., "From Data Mining to Knowledge Discovery: an Overview," *Advances in Knowledge Discovery and Data Mining*, AAAI/MIT Press, (1996), pp. 1-34.
[10] Chicco G, Napoli, R., Postulache, P., Scutariu, M. and Toader, C., "Customer Characterization Options for Improving the Tariff Offer," *IEEE Transactions on Power Systems*, Vol. 18, (2003), pp. 381-387.
[11] Ramos, S., Vale, Z., Santana, J., and Duarte, J., "Data Mining Contributions to Characterize MV Consumers and to Improve the Suppliers-Consumers Settlements," *PES GM 07– IEEE Power Engineering Society*, Tampa, Florida, USA, 24-28 July, (2007).
[12] GAMS Development Corporation, Washington, DC 20007, USA, "*GAMS-The Solver Manuals*," GAMS User Notes, (2001).
[13] Morais, H., Vale, Z., Faria, F., and Khodr, H. M., "Optimal Scheduling of a Renewable Micro-Grid in an Isolated Load Area Using Mixed-Integer Linear Programming," *Renewable Energy*, Vol. 35, (2010), pp. 151–156.

الإدارة المثلى لمصادر الطاقة المتجددة باستخدام منهجية منتج القدرة ووكيل المستهلك الافتراضي

حسين محمد خضر

كلية الهندسة- جامعة القصيم- المملكة العربية السعودية
khodr.hussein@qec.edu.sa

(قدم للنشر في ١١/٢٩ /٢٠١١م ؛ قبل للنشر في ٢/٩ /٢٠١٢م)

ملخص البحث. يستخدم هذا البحث منهجية منتج القدرة ووكيل المستهلك الإفتراضي بغرض الحصول على ادارة مثلى لمصادر طاقة جديدة موزعة، وكذلك تحسين التحكم في إدارة جهة الطلب وأحماله المجمعة، وتعتمد الطريقة على مقترح للتنسيق بين تقنيات توليد الطاقة ونوعيات الأحمال المختلفة ونظم التخزين. هذه الطريقة تستخدم إطار عمل مبني على أساليب تنقيب البيانات لتحديد منحنيات أحمال المستهلكين. ولقد تم صياغة مسألة إيجاد التحكم الأمثل باستخدام البرمجة الخطية للأعداد الصحيحة المختلطة، وذلك بسبب وجود متغيرات ذات طبيعة مستمرة وأخرى ذات طبيعة رقمية ثنائية. وقد تم نمذجة المسألة رياضياً باستخدام نظام النمذجة الجبرية العامة، وحلت بواسطة حزمة برمجة ذات كفاءة مرتفعة يمكنها إيجاد الحلول للبرمجة الخطية وبرمجة الأعداد الصحيحة المختلطة وأيضا البرمجة التربيعية.

ولقد أظهر تطبيق الطريقة لدراسة حالة حقيقية في منطقة خدمة كهربائية معزولة في البرتغال كفاءة عالية في تحديد التشغيل والتحكم الذي يحقق الأداء الأمثل لتلك الشبكة الصغيرة، ولقد تم الوصول إلى النتائج المثلى بعد ٣٠ محاولة وفي زمن لم يتجاوز ٩٠ ميللي ثانية.

Journal of Engineering and Computer Sciences
Qassim University, Vol. 5, No. 1, pp. 53-76 (January 2012/Safar 1433H)

Frost Formation and Heat Transfer over Flat Plate Evaporator

G.I. Sultan[*a,b], E. A. ElShafiee[a], M. G. Safan[a], M. A. Elraouf
[a] *Mansoura University, Faculty of Engineering, Mansoura, Egypt*
[b] *Qassim University, Faculty of engineering, Burydah, Saudi Arabia*
Email: gisultan@mans.edu.eg

(Received 2/3/2011; accepted for publication 24/2/2012)

ABSTRACT. In the present study, numerical and experimental investigations of heat and mass transfer characteristics of a plate type evaporator immersed in a still humid air environment with the presence of frost formation is carried out. In the numerical investigation, the suggested model considered the frost layer as a porous medium. The solution of a set of partial differential equations characterizing frost formation taking into consideration the variation of air ambient conditions during frost formation process and a diffusion term is preceded. In experimental investigation, the ambient air temperature is changed over a range of 20°C to 25°C and the relative humidity is varied from 41% to 56% while maintaining the plate type evaporator average temperature at nearly -10°C. Also, Rayleigh number was varied from 10^4 to $1.2x10^6$ and the dimensionless time from zero to 1. The results show that the system coefficient of performance decreases within a range of (10% - 15%), the average Nusselt number varies within a range of (15% - 30%) and the average Sherwood number varies within a range of (25% - 40%).

Keywords: frost formation, moisture, mass transfer**.**

NOMENCLATURE

A	Face area	**m^2**
Cp	Specific heat	kJ/kg.K
C	Concentration	kg/m^3
D	Diffusion coefficient	m^2/**s**
G	Gravity acceleration	**m/s^2**
H	Convective heat transfer coefficient	$W/m^2.K$
h_m	Mass transfer coefficient	m/s
I	Compressor current intensity	**A**
K	Thermal conductivity	W/m.K
L	Length of flat plat evaporator.	**m**
$\dot{m}$	Rate of mass collected from the cooled frost	kg/s
M	Mass of collected frost	**kg**
m"	Frost mass flux	kg/m^2
N	No. of measuring points on the surface (6 points)	-
P	Pressure	**N/m^2**
q''	Heat flux	kW/m^2
Q_{add}	Rate of heat added to the system	kW
Q_{loss}	Rate of heat loss from the system to the surrounding	kW
$Q_{tot.}$	Sum of rates of added and lost heat from the system	kW

T	The system collecting time duration	s
T_{air}	Ambient air temperature	K
$T_{f,s}$	Frost surface temperature	K
T_i	Plate surface temperature at point i	K
T_p	Flat plate average temperature	K
U	Velocity component in x-direction	m/s
V_c	Potential difference of the feeding current	V
V	Velocity component in y-direction	m/s
W_d	Input work of the compressor	kW
$\overline{W}_d$	Average input work of the compressor	kW
X	X-coordinate	m
Y	Y-coordinate	m
y_f	Frost thickness	m
$y_{f,init.}$	Initial frost thickness	m
$L_{Solid.}$	Latent heat of solidification	kJ/kg
$L_{Liq.}$	Latent heat of condification	kJ/kg
$L_{Sub.}$	Latent heat of sublimation	kJ/kg
ΔT_{sens}	Sensible temperature difference	K
Greek Symbols		
B	Volumetric coefficient of thermal expansion	/ᵑK
ρ_f	Frost density	kg/m^3
Δ	Quantity difference	-
N	Kinematic viscosity	m^2/s
T	Dimensionless time	-
Dimensionless Groups		
Nu	Nusselt number	$\frac{h A_l}{k}$
Pr	Prantdl number	$\frac{\nu}{\alpha}$
Ra	Rayleigh number	$\frac{\rho \beta g \Delta T A_l^3}{\alpha A \nu}$
Sh	Sherwood number	$\frac{h A_l}{D}$
τ	Dimensionless time	$t.v/L^2$
Sub-scripts		
A	Air	-
c,sat	Condensate at saturation	-
f,s	Frost surface	-
Nb	Neighbors of the given grid point Po	-
P	Flat plate	-
Sat	Saturation	-
∞	Ambient	-
Super-scripts		
˚	Flow rate	-
″	Flux	-

1. INTRODUCTION

In the developing world, refrigeration is used chiefly to store foodstuffs at low temperatures, thus inhibiting the destructive action of bacteria, yeasts, and molds. Whenever humid air comes in contact with a cooling coil, its temperature is below both the dew-point of air and the freezing point, frost will form. The nature of the frost forming on the coil will depend on the psychometric conditions prevailing inside the freezer and whether the air around the coil is sub-saturated or supersaturated. The processes involving heat transfer from a humid air stream to a plate, with simultaneous deposition of frost, are of great importance in a variety of refrigeration equipment. It was well recognized that frost formation on heat exchanger surfaces seriously affects the performance of a refrigeration system.

A lot of research work has been done to study the growth of frost on a cooling coil. Kennedy and Goodman [1], investigated frost formation on a vertical surface under natural convection conditions. Local heat and mass transfer coefficients from humid air to the frost surface with effective thermal conductivity and density of the frost were studied. The temperature distribution in the boundary layer adjacent to the frost surface allowed the calculation of the local values of the heat flux. Marinyuk [2], studied experimentally the effect of frost formation on heat transfer between a cylinder and its gaseous environment. The studied parameters were the total heat flux, the steady-state convective heat transfer coefficient, and the mass of frost adhering to the test cylinder. He concluded that thermal conductivity was the main emphasis of frost and the diffusion mechanisms of moisture transfer within the frost layer causes the frost density and thermal conductivity to increase with time. Östin and Andersson [3], studied the formation of frost on parallel horizontal plates facing a forced air stream at varying temperatures, relative humidity and air velocities. They found that both the surface temperature of the plates and the relative humidity of the air stream have important effects on the frost thickness. Also, the density of frost was found to increase with relative humidity and air velocity. A strip method was applied to determine the thermal conductivity and internal changes in the frost layer. They observed two categories of frost formation, monotonic and cyclic growth. The condensed water vapor contributed in equal amounts to increase in the thickness and the density while in the latter melting at the frost surface results in abrupt internal densification. Tao *et al.* [4], simulated frost deposition on a cold surface exposed to a warm moist air flow using a one- dimensional, transient formulation based on the local volume averaging technique. The spatial distribution of the temperature, ice-phase volume fraction (related to frost density) and rate of phase change within the frost layer were predicted. Their results indicated that the local effective vapor mass diffusivity was up to seven times larger than the molecular diffusivity of water vapor in air. Le Gal *et al.* [5], predicted a one-dimensional transient formulation to predict frost growth and densification on a cold wall submitted to a moist air flow. The model was based on a local volume averaging technique that allows the computation of temperature and density distributions throughout the entire frost layer according to time. The effective vapor mass diffusivity throughout frost should reach values several times

larger than the molecular. Wu and Webb [6], conducted an experimental study to investigate the possibility of causing frost on a cold surface. Both hydrophilic and hydrophobic surfaces were examined. A thermo-electric cooler was used to provide a cooling source for the frosting surface. Fossa and Tanda [7], investigated experimentally and theoretically frost growth on a vertical plate in free convection and developed a simple model to predict frost growth key parameters (frost thickness, heat/mass transfer rates). The model had a good agreement with the experiments owing to the some simplifying assumptions made in the model (frost/air interface assumed to be flat, and the usage of simple relationships for frost properties). Cheng and Wu [8], investigated experimentally and theoretically the frost formation on a cold plate. Experimental observations were performed for the early stage of the frost growth process. It was found that the frost layer may exhibit a multiple-step ascending pattern in no more than 30 min which means that in a short time, the frost layer was possible to reach the frost layer full growth period under some certain environmental conditions, especially for the cases at higher air temperature, higher air humidity, or higher air velocity. Lee *et al.* [9], presented a mathematical model to predict the frost layer growth and the heat and mass transfer by coupling the air flow with the frost layer without employing experimental correlations. They dealt with the frost layer as a porous. The parameters considered in their search were the plate surface temperature and air conditions, such as air velocity, temperature, and absolute humidity and finally the frost surface temperature. Cheng and Shiu [10], investigated the frost formation on a cold plate in atmospheric air flow experimentally and theoretically. A microscopic image system was used to provide observations for the early stage of the frost growth process, record the pattern and the thickness of the frost layer per five seconds after the onset of frost formation. They observed a multiple-step ascending frost growth pattern caused by melting of frost crystals at the frost surface. The effects of velocity, temperature and relative humidity of air were studied with varied surface temperature of the cold plate. Shin *et al.* [11], investigated experimentally the effect of surface temperature on frost formation. Test samples with three different surfaces of which dynamic contact angles were 23, 55, and 88 deg were installed in a wind tunnel and exposed to a humid air flow. The air flow Reynolds number, humidity, the air and the cold plate temperatures were maintained at 9000, 0.0042 kg/kg dry air, 12°C and -22°C, respectively. The thickness and mass of frost layer were measured and used to calculate frost density while heat flux and temperature profile were measured to obtain thermal conductivity. Their results showed that the surface with a lower dynamic contact angle showed a higher frost density and thermal conductivity during a two-hour test. Lee and Yang [12], developed frost maps for two different surfaces having two different hydrophilic characteristics and to find ambient conditions associated with the formation of frost structures. They found that frost structures on surfaces with different direct contact angles are similar. However, low direct contact angle surface at low humidity provides (20–30%) denser frost formation due to the shift of areas with different structures. Yang and Lee [13], proposed a mathematical model to predict frost properties , heat and

mass transfer within the frost layer formed on a cold plate. Laminar flow equations were employed for moist air and empirical correlations for local frost properties to predict the frost layer growth. Their results showed that the heat transfer coefficients obtained under non-frosting conditions are lower by 30% than those under frosting conditions and concluded that the air flow should be analyzed to obtain the accurate prediction for the frost growth. Lee and Ro [14], made a simple model on the assumption that the water-vapor concentration at the frost surface was saturated, and that the gradient of vapor pressure was the same as the value obtained from the (Clausius–Clapeyron) equation. Initial porosity of the frost layer affected the characteristics of frost growth and so modified the model with the assumption that the concentration of water-vapor at the frost surface was in super-saturation in order to solve the inconsistency of the diffusion resistance of water-vapor in the region of high porosity. Tso *et al.* [15], developed a model with two-phase flow for refrigerant coupled with a frost model for studying the behavior of an evaporator. They concluded that the formation of frost degrades the performance of the evaporator and that the air and wall temperature varies along the tubes and coil depth, which will lead to non-uniform frost growth with coil depth. Wu *et al.* [16], investigated experimentally frost formation on a horizontal copper. Their experiments showed that the frost formation on a cold surface generally began with the formation and growth of condensate droplets, freezing of the super-cooled condensate droplets, formation and growth of initial frost crystals on the frozen droplets, growth of frost crystals accompanied by the collapse of some of the crystals, and finally frost layer growth. Getu and Bansal [17], presented a theoretical model and experimental analyses of evaporators in frozen-food display cabinets at low temperatures in the supermarket industry. Their mathematical model adopted various empirical correlations of heat transfer coefficients and frost properties in a fin-tube heat exchanger in order to investigate the influence of indoor conditions on the performance of the display cabinets as it would be a good guide tool to the design engineers to evaluate the performance of supermarket display cabinet heat exchangers under various store conditions. Piucco *et al.* [18], advanced an investigation on the frost nucleation on flat surfaces as it focuses on the relevant parameters affecting the frost formation process, i.e., the surrounding air temperature and humidity, and the surface conditions (temperature, roughness and contact angle). Gupta *et al.* [19], presented a study of thermo-fluidic model developed for a domestic frost-free refrigerator. The governing equations, coupled with pertinent boundary conditions, are solved by employing a conservative control volume formulation, in the environment of a three-dimensional unstructured mesh. For the freezer compartment, the computationally predicted temperatures are somewhat higher than the experimental ones. Laguerre *et al.* [20], carried out experiments using a rectangular refrigerating cavity which can be more or less humidified and loaded with arranged cylinders. One of the vertical walls, made of aluminum, was kept at low temperature ($+1^{o}$C). They found that influence of water evaporation on air and cylinder temperatures is more pronounced at the bottom of the cavity.

In this work, a mathematical model is proposed and used to predict the frost formation and its growth accumulation on a flat plate heat exchanger. Heat and mass transfer coefficients and frost formation effect on the system performance are predicted. An experimental test rig is set up in a free air stream to validate the mathematical model.

2. THEORTICAL MODEL

In the present model, the moist air flows over a flat plate are shown in Figure (1) and frost layer is considered as a porous media. In order to predict the behavior of frost layer growth, it is assumed that all processes are unsteady and the variation of frost density in the direction normal to the horizontal cooling plate is negligible.

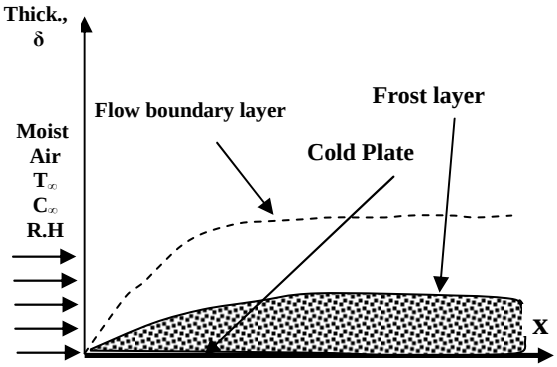

Fig.(1). Schematic diagram of theoretical model.

The governing equations are continuity, momentum, energy, and mass concentration assuming incompressible laminar flow with no viscous dissipation and using Boussinesqi approximation, these can be expressed as follows:

i. Continuity equation:

$$\frac{\partial u}{\partial x} + \frac{\partial v}{\partial y} = 0 \tag{1}$$

ii. Momentum equations:

$$\frac{\partial u}{\partial t} + u\frac{\partial u}{\partial x} + v\frac{\partial u}{\partial y} = -\frac{1}{\rho}\frac{\partial P}{\partial x} + \upsilon\left(\frac{\partial^2 u}{\partial x^2} + \frac{\partial^2 u}{\partial y^2}\right) \tag{2}$$

$$\frac{\partial v}{\partial t} + u\frac{\partial v}{\partial x} + v\frac{\partial v}{\partial y} = -\frac{1}{\rho}\frac{\partial P}{\partial y} + \upsilon\left(\frac{\partial^2 v}{\partial x^2} + \frac{\partial^2 v}{\partial y^2}\right) + g\beta(T - T_\infty) \tag{3}$$

iii. Energy equation:

$$\frac{\partial T}{\partial t} + u\frac{\partial T}{\partial x} + v\frac{\partial T}{\partial y} = \frac{k}{\rho Cp}\left(\frac{\partial^2 T}{\partial x^2} + \frac{\partial^2 T}{\partial y^2}\right) \tag{4}$$

iv. Mass concentration equation:

$$\frac{\partial C}{\partial t} + u\frac{\partial C}{\partial x} + v\frac{\partial C}{\partial y} = D\left(\frac{\partial^2 C}{\partial x^2} + \frac{\partial^2 C}{\partial y^2}\right) \quad (5)$$

v. The initial and boundary conditions

At the plate surface at (y=0)

$$at\ t = 0,\ u = 0,\ v = 0,\ T = T_w,\ C = C_w \quad (6)$$
$$0 \le x \le L,\ y = y_{f,int},\ C = C_{f,int}$$

Far from the surface at (y→∞)

$$\frac{\partial u}{\partial x} = 0,\ v = 0,\ T = T_w,\ C = C_w \quad (7)$$

For Interface between the frost layer and air

$$\left(\frac{\partial T}{\partial y}\right)_{y=y_f} = \frac{k}{k_f}\left(\frac{\partial T}{\partial y}\right)_{y=y_f^-} + \frac{\rho L_{sub} D}{k_a}\left(\frac{\partial T}{\partial y}\right)_{y=y_f^+} \quad (8)$$

The previous equations can be solved to get the physical quantities heat and mass transfer coefficients and in turn Nusselt and Sherwood numbers as follows:

$$h = \frac{q''}{(T_a - T_p)} \quad \& \quad h_m = \frac{\Delta C''}{(\rho_{va} - \rho_{vf})} \quad (9)$$

Where q'' is the heat flux by the plate surface area, T_{air} is the temperature of the surrounding ambient air, T_p is that of the plate, Δc *is* the concentration flux of the collected frost and ρ_{va} is the vapor density at air temperature and ρ_{vf} is the vapor density at frost surface temperature.

$$Nu = \frac{h L}{k}, \quad Sh = \frac{h_m L}{D} \quad (10)$$

Where L is the plate length, k is the thermal conductivity of air and D is the mass diffusivity of water vapor in air.

vi. Calculation of frost properties:

The water vapor transferred into the frost surface from moist air increases both the frost density (C_δ) and thickness (C_ρ). This phenomenon can be expressed as follows:

$$C_f = \frac{\rho D}{\Delta C}\left(\frac{\partial C}{\partial Y}\right)_{\delta_f} = C_\delta + C_\rho \quad (11)$$

The mass flux for the frost density absorbed into frost layer is given by:

$$C_\rho = \int_{y=0}^{y=y_f}\left(\frac{D\ \rho_{vf}}{\Delta C}\right) dy \quad (12)$$

The frost density and thickness for each time interval are calculated as follows:

$$C_f^{t+\Delta t} = C_f^t + \left(\frac{C_\rho}{\rho_f\ y_f}\right)\Delta\tau \quad (13)$$

$$y_f^{t+\Delta t} = y_f^t + \frac{C_y}{\rho_f\ y_f} \quad (14)$$

The previous equations are solved using (CFD) Fluent 6.26 numerical technique.

3. EXPERIMENTAL TEST RIG

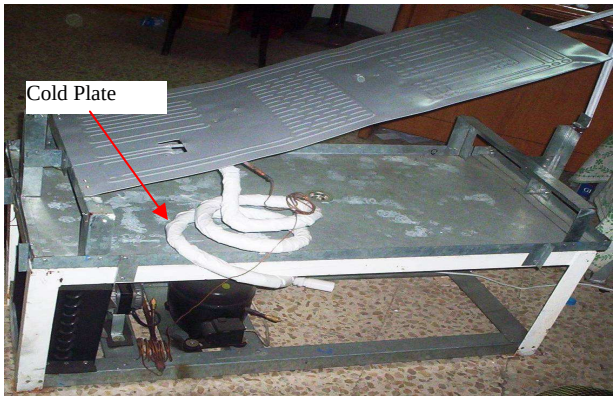

Fig.(2). Photo of the test rig components.

A photo of the test rig is presented in Figure (2). Figure (3) shows a schematic diagram for the details of the test rig. It consists of a simple refrigeration system with an easily tilted evaporator that is supported on an iron frame. The apparatus components are listed as follows: An evaporator flat plate (1) which is aluminum 980 mm 320 mm x 4 mm thickness and the flowing tubes which are punched through the plate. The evaporator is supported with two hinges at one side and riveted with a handle to help in tilting.

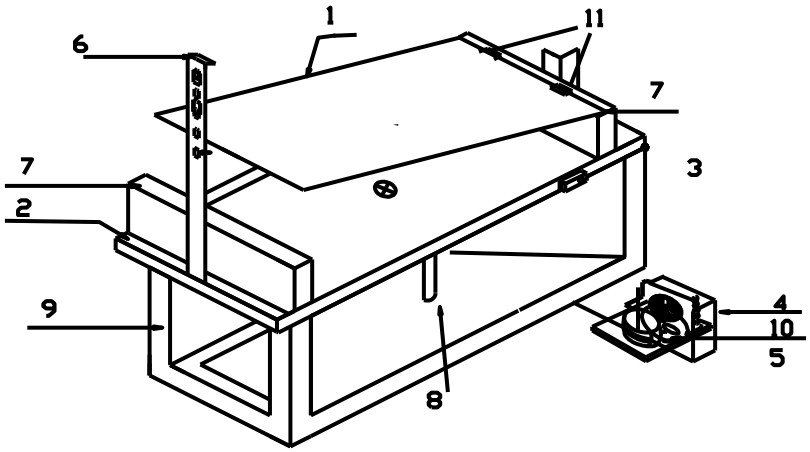

Fig.(3). Details of the test rig.

1. Evaporator
2. Drain enclosure
3. Thermostat
4. Air cooled condenser
5. Hermetic compressor
6. Level handlers
7. Evaporator seats
8. Drain hose
9. Apparatus body
10. Condenser fan
11. Tilt Hinges.

A drain pan (2) is made of a galvanized steel sheet (1160 x 550) mm, 1 mm thickness and height 5 mm. This enclosure supports the evaporator seats and collects the drainage of the melted ice from the evaporator. A thermostat (3) which is the main controller of the refrigeration cycle as it contains a bulb that is supported on the lower face of the evaporator. It has a range from (-30^{o}C / 30^{o}C) as it passes the electric current through the cycle only if it has not reached the required temperature. A condenser (4) which is an air cooled coil made of iron (270 mm x 270 mm x140 mm) with 5 rows and 3 columns of tubes.

A hermetic compressor (5) of 1/3 hp capacity and works on refrigerant R134a with a starting circuit and overload protection (power factor is 0.9). Two level steel handlers (6) 130 mm x 15 mm with holes for supporting the evaporator during its tilting. One of these is riveted to the plate and the other hinged to the evaporator seats (7). Evaporator seats are a pair of U-shaped galvanized steel pieces that are supported on the drain enclosure at the two ends of the evaporator. One includes the two tilting hinges and the other holds the plate when it is totally horizontal. Drain hose (8) is a flexible plastic hose that drains the melted frost from the two faces of the evaporator through the drainage tank. Apparatus frame (9) is made from iron 1130 mm x 460 mm x 400 mm. that includes the compressor, the condenser with its fan and the thermostat inside it and carries the evaporator with the drainage enclosure. Condenser fan (10) is an electric fan that is placed in one face of the condenser to help the heat transferring out of the condenser.

4. DATA REDUCTION

The frost formation mass flow rate (m˚) can be calculated for a time average as:

$$\dot{m} = \frac{m}{t} \tag{15}$$

Where, *m* is the mass of collected frost in grams and t is the time interval in seconds**,** The plate temperature can be calculated as the average temperature at different points on the plate as shown in Figure.(4).

$$T_p = \frac{\sum_{i=1}^{n} T_i}{n} \tag{16}$$

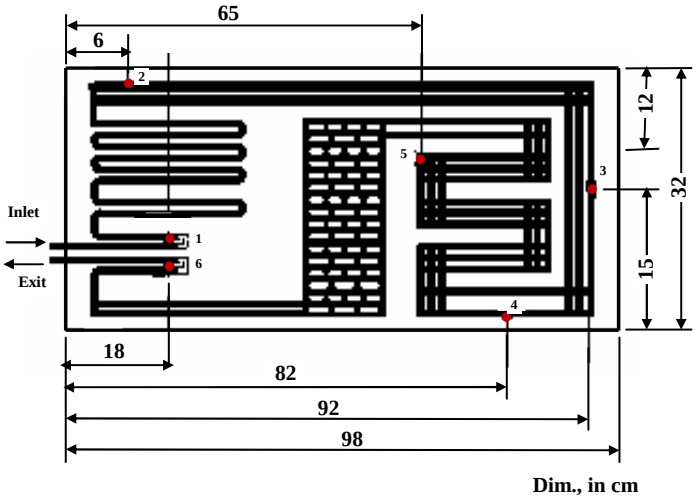

Fig.(4). Schematic diagram for the thermocouples position on the plate surface.

The quantity of heat added to the system (which is both sensible and latent) ($Q_{Add.}$) can be calculated as follows:

$$Q_{add} = \dot{m}\left[(Cp\Delta T_{sen})_v + L_{liq} + (Cp\Delta T_{sen})_s + L_{solid}\right] \quad (17)$$

Where, $L_{Liq.}$ is the latent heat of liquefaction, C_p is the specific heat of water, L_{Solid} is the latent heat of solidification of water, $\Delta T_{sens.)v}$ is the sensible temperature difference between liquid water and freezing point and $\Delta T_{sens.)s}$ is the sensible temperature difference between freezing point and the frost surface temperature.

The rate of heat gain from the environment can be described as:

$$Q_{loss} = h_a A \Delta T_{sen} \quad (18)$$

Where h_{air} is the convection heat transfer coefficient ($W/m^2.K$)**,** A is the evaporator surface area and $\Delta T_{loss.}$ is the Temperature difference between the frost and ambient temperature**.**

One can calculate the total capacity up the system as follows:

$$Q_T = Q_{add} + Q_{loss} \quad (19)$$

The input power of the refrigeration system is that of the compressor which can be calculated as follows

$$\dot{W}_d = I V_c \cos \emptyset \quad (20)$$

Where I is the compressor current intensity, V is the potential difference of the feeding current and cos φ is the power factor.

The coefficient of performance of the system (COP) and heat flux q" are calculated from:

$$COP = \frac{Q_T}{W_d} \quad (21)$$

$$q'' = \frac{Q_T}{A} \tag{22}$$

Where q" is the heat flux .
The time average convective heat transfer coefficient (h) by dividing the heat flux by the temperature difference between ambient air and that of the plate as:

$$h = \frac{q''}{T_a - T_{f,s}} \tag{23}$$

Where $T_{f,s}$ is the frost surface temperature.

Nusselt number can be calculated as follows:

$$Nu = \frac{h\ L}{k} \tag{24}$$

Where L is the plate length and k is the thermal conductivity of air (W/m.K).

Similarly, one can calculate the time average mass transfer coefficient h_m by dividing the mass collected by both the plate surface area and the density difference between that of the water vapor at surrounding air temperature and that of just to be formed frost.

$$h_m = \frac{\dot{m}}{A\left(\rho_{v,a} - \rho_{f,s}\right)} \tag{25}$$

And so Sherwood number can be calculated as follows:

$$Sh = \frac{h_m\ L}{D} \tag{26}$$

Where L is the plate length and D is the mass diffusivity of water vapor, and the moist air properties are calculated at bulk temperature between frost surface and air temperature.

5. MEASUREMENTS AND INSTRUMENTATION

5.1 Temperatures measurement

The temperature of the evaporator surface is measured by Copper – Constantan thermo-couples (T-type) of 0.5 mm as shown in Figure (4) (six thermocouples are glued into the surface of evaporator by high conductive glue (epoxy) and distributed on the surface). They are connected to the temperature recorder via a selector switch to the temperature recorder which has an accuracy of (**±0.**1°C).The surface temperature is considered to be the average temperature of al thermocouples readings.

5.2 Ambient temperature and relative humidity measurement

The ambient conditions that are measured by a thermo/hygrometer with range for temperature -10°C to 60°C ±(1°C) and for relative humidity 10 % to 99 % ±(3%)).

5.3 Frost mass measurement

A sensitive digital balance is used for measuring the mass of the formed frost on both sides of the evaporated surface after melting that are drained into the drain

enclosure. The balance has a range from (0.2 – 300 g) and with an accuracy of (±1%).

5.4 Electric current intensity and potential difference measurement

The electric current intensity is measured by digital ammeter with the following specifications [range (0 - 10 Amp.± 1 %)] and the electric potential difference is measured by digital voltmeter the following specifications [range (0- 400 V ± 1%)].

6. EXPERIMENTAL ERROR ANALYSIS

The accuracy of the results obtained from experimental measurements is governed by the accuracy of the individual measuring devices. The maximum error in calculating heat transfer coefficient, mass transfer coefficient, Sherwood number are ±4.35%, ±6.5% and ±8.2% while the maximum error in calculating COP is about ±2%.

7. RESULTS AND DISCUSSION

7.1 Theoretical model results:

The theoretical results are illustrated for a two dimensional model using CFD (FLUENT 6.26) package. Figure (5) indicated that the average Nusselt number increases with increasing Rayleigh number until it reach the constant value at Rayleigh number up to $4x10^5$ because the frost layer takes its maximum value and acts as insulation. Also, the average Nusselt number increases with increasing of Prandtle number.

Figure (6) shows that the average Sherwood number has the same trend of average Nusselt number with Rayleigh number. The average Sherwood number increases with increasing Rayleigh number. Also, the average Sherwood number slightly increases with increasing of Schmidt number.

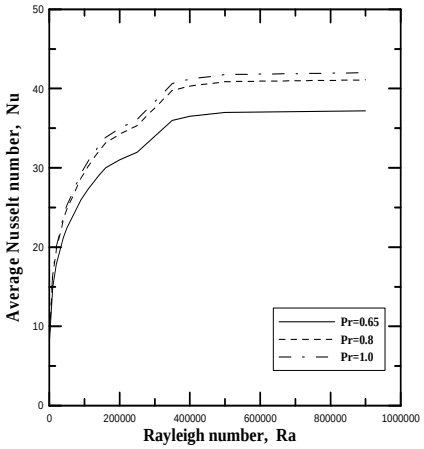

Fig.(5). Nusselt number versus Rayleigh number

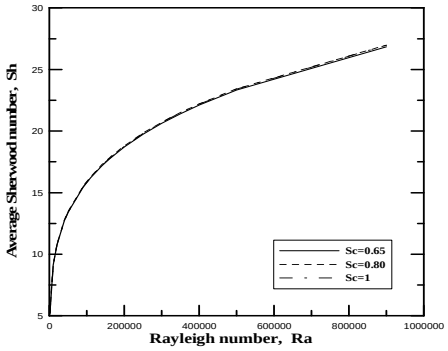

Fig.(6). Sherwood number versus Rayleigh number

7.2 Effect of plate temperature:

From Figure (7), the air temperature at a plane 3 mm above the cold surface increases with the dimensionless distance (x_i/L). It is noted that at lower plate temperatures, the rate of increasing the air temperature is higher. Also, the air temperature increases for increasing plate temperature at a certain horizontal position.

The variation of local Nusselt number with dimensionless horizontal distance is shown in Figure (8). The local Nusselt number increases with the decreasing of the plate temperature.

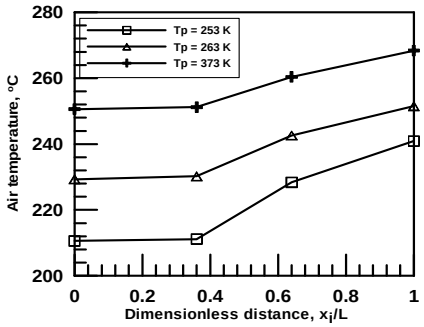

Fig.(7). Plate temperature distribution along the plate

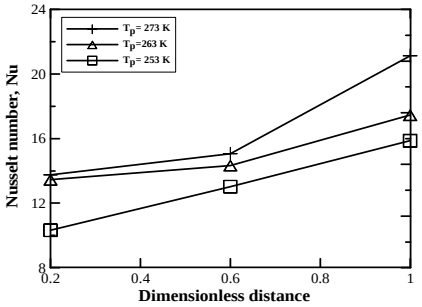

Fig.(8). Local Nusselt number vs position.

Figure (9), shows the plate temperature with dimensionless time ($\tau = \frac{\alpha_w t}{L^2}$) at different relative humidity. At a certain relative humidity, the plate temperature decreases with time. This decrease is due to the increase in the frost layer thickness which decreases the rate of heat transfer between the free air and the plate surface. The frost layer works as a growing insulator with time.

Figure (10) illustrates the relation between plate temperature and dimensionless time at different air temperature and fixed relative humidity of 52%. One can deduce that the plate temperature decreases with time due to the growth of frost layer.

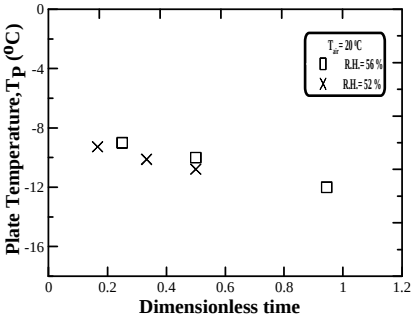

Fig.(9). Average plate temperature versus dimensionless time at varying relative humidity

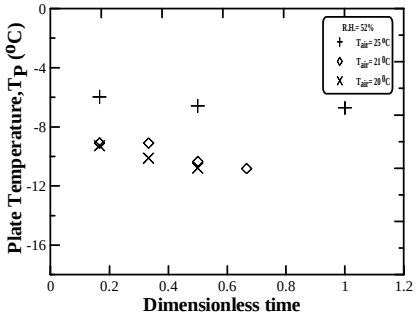

Fig.(10). Average plate temp., versus dimensionless time at varying air temperature

7.3 Validity of the model:

The average Nusselt number calculated from the present model is compared with that of the reference [13] for the same range of Rayeligh number at unity Prantdl number as shown in Figure (11). For the present and previous models the average Nusselt number increases with the increasing of Rayleigh number and takes the same trend.

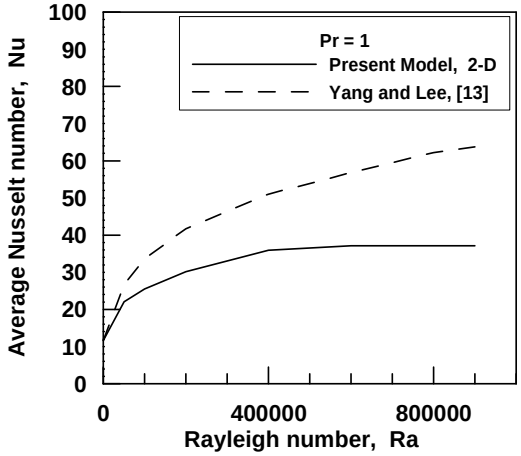

Fig.(11). Nusselt number versus Rayleigh number comparison.

8. EXPERIMENTAL RESULTS

The experimental results including plate temperature, frost collected mass, frost thickness, coefficient of performance of the system, heat and mass transfer coefficients, Nusselt and Sherwood numbers are demonstrated.

8.1 Plate temperature:

Figure (12) illustrates the plate temperature variation with dimensionless time, ($\tau = t.\nu/L^2$) at different relative humidity. One can recognize that at a certain relative humidity, the plate temperature decreases with time and this decreasing is due the increase in the frost layer thickness which decreases the rate of heat transfer between the free air stream and the plate surface. The frost layer works as a growing insulator with time. The higher the relative humidity, the higher the rate of this degradation can be observed.

Figure (13) shows the relation between plate temperature and dimensionless , ($\tau = t.\nu/L^2$) at different air temperature while relative humidity is 52%. It is deduced that the plate temperature decreases with both time due to the growing frost layer insulating process.

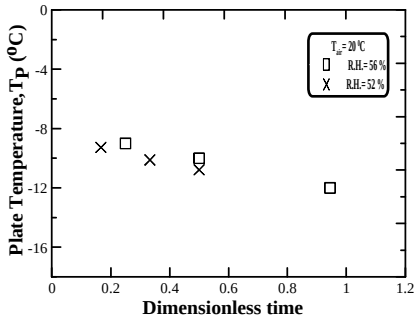

Fig.(12). Average plate temp., versus dimensionless time at varying relative humidity.

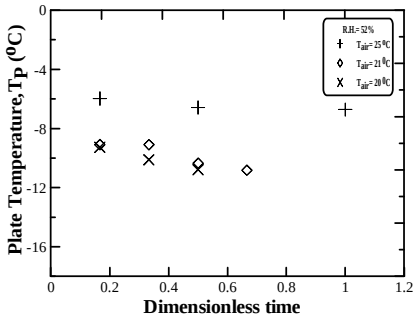

Fig.(13). Average plate temp., versus dimensionless time at varying air temperature.

8.2 Frost collected mass

Figure (14) illustrates the relation between frost mass collected (total mass from the plate) and dimensionless time, ($\tau = t.\nu/L^2$) at different relative humidity. One can observe that the increase of the collected frost mass with time which is reasonable due to the increase of the water vapor frosted from the air stream as the thickness and density of the frost layer increases with time. Also, it can be observed that the collected frost mass increases with the increase of the relative humidity for the same air temperature due to the increment of moisture content available in the same air stream subjected to be frosted on the plate.

Figure (15) illustrates the relation between frost mass collected and dimensionless time at different relative humidity. One can find that the frost mass collected increases with time at any air temperature. In a certain time the collected mass increases with increase of air temperature for the same relative humidity as the air moisture content increases and so the ability of changing a bigger part of it into frost is substantial.

8.3 Frost thickness:

One can illustrate that the relation between frost thickness and dimensionless time at different relative humidity from Figure. (16). It is noticeable that the frost thickness increases with time as the frost layer accumulates, Also, one can notice the higher increase in the frost thickness at higher air relative humidity for the same air temperature.

Figure (17) illustrates the relation between frost thickness and dimensionless time at different air temperature; one can deduce the increase of the frost layer with time and with air temperature as the frost layer accumulates due to the increase in the moisture content.

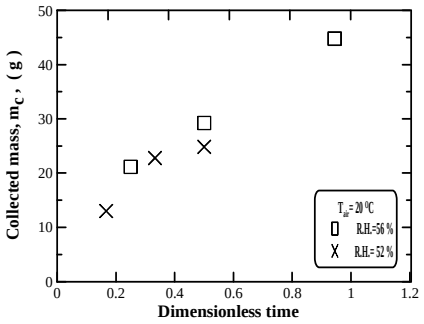

Fig. (14). The frost collected mass versus dimensionless time at Tair= 20OC.

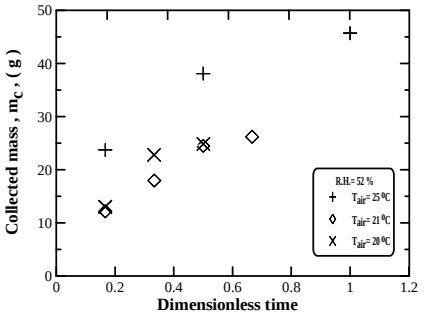

Fig.(15). The frost collected mass versus dimensionless time at R.H.=52%.

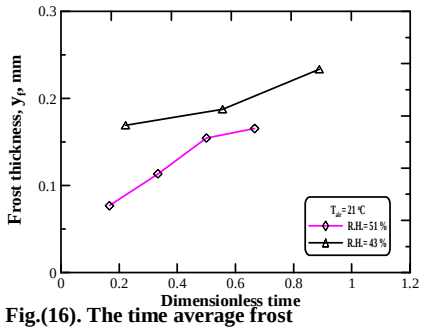

Fig.(16). The time average frost thickness and dimensionless time at Tair= 21 OC.

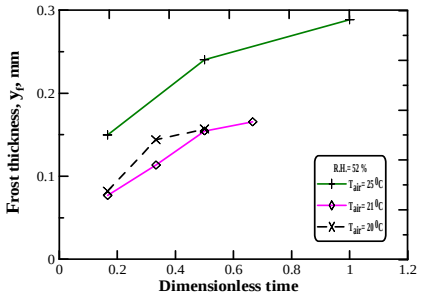

Fig.(17). The time average frost thickness and dimensionless time at R.H.= 52%.

8.4 Coefficient of performance

Figure (18) illustrates the relation between the average coefficient of performance and dimensionless time at different relative humidity; one can recognize the coefficient of performance decreasing with time for a range from (10-15%) due to the frost layer blockage and so degrading heat transfer process and so increasing the average compressor work done and increasing the frost thickness above the plate. Figure (19) illustrates the average coefficient of performance and dimensionless time at different air temperature; one can recognize that the decreasing of coefficient of performance is due to the growth of frost layer with time within a range of (10-15%). Due to the previously noted, frost layer blockage, the compressor work increases.

8.5 Effect of dimensionless time on heat and mass transfer coefficients

Figure (20) illustrates the relation between the time average heat transfer coefficient and dimensionless time at constant air temperature. The heat transfer coefficient increases during

the early stage, while it decreases uniformly with time after that as the frost layer acts as heat transfer blocker.

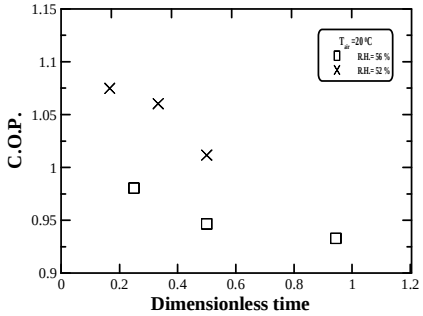

Fig. (18). The coefficient of performance versus dimensionless time at Tair= 20OC.

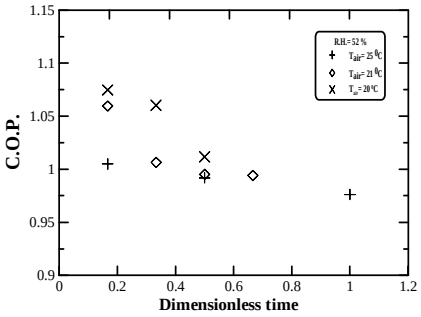

Fig.(19). The coefficient of performance versus dimensionless time at R.H.=52%.

Figure (21) illustrates the relation between the time average heat transfer coefficient and dimensionless time at constant relative humidity. The heat transfer coefficient increases uniformly with time, Also, the air temperature is inversely proportional to the heat transfer coefficient.

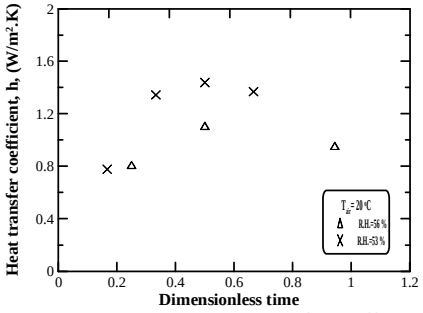

Fig.(20). Time average heat transfer coeff. versus dimensionless time at Tair= 20OC.

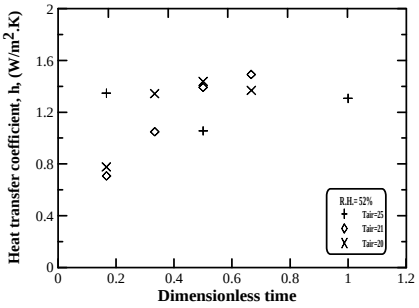

Fig.(21). Time average heat transfer coeff. and dimensionless time at R.H.=52%.

Figure (22) illustrates the relation between the mass transfer coefficient and dimensionless time at constant relative humidity at different air temperature. It is clear that the mass transfer coefficient increases uniformly with time and the lower the air temperature, the higher the mass transfer coefficient.

Figure (23) illustrates the relation between the mass transfer coefficient and dimensionless time, ($\tau = t.\nu/L^2$) at constant relative humidity at different air temperature. One can observe that the mass transfer coefficient increases uniformly with time and the lower the air temperature, the higher the mass transfer coefficient.

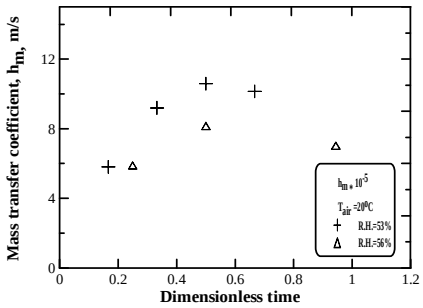

Fig.(22). Time average mass transfer coeff. versus dimensionless time at Tair= 20OC.

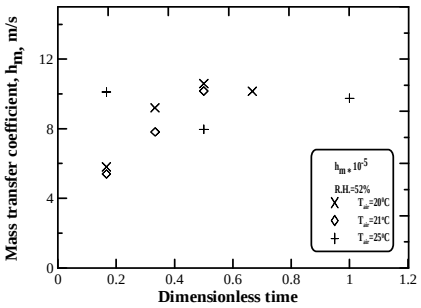

Fig.(23). Time average mass transfer coeff. versus dimensionless time at R.H.= 5.

8.6 Effect on dimensionless time on Nusselt and Sherwood numbers

Figure (24) illustrates Nusselt number and dimensionless time at constant air temperature and different relative humidity. It is observed that Nusselt number has the same trend of the heat transfer coefficient as Nusselt number increases during the early stage, while it decreases uniformly with time after that as the frost layer acts as heat transfer blocker.

Figure (25) illustrates the relation between Nusselt number and dimensionless time at constant relative humidity and different air temperature. The average Nusselt number increases uniformly with time and the air temperature is inversely proportional to the average Nusselt number.

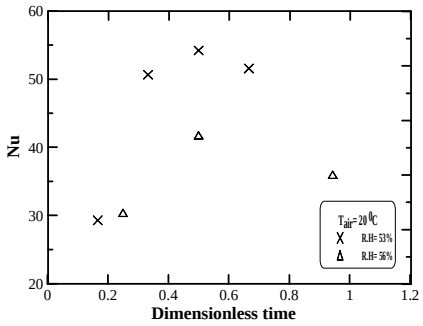

Fig.(24). Time average Nusselt number versus dimensionless time at Tair= 20OC.

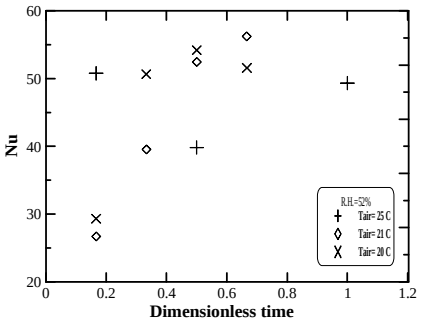

Fig.(25) . Time average Nusselt number versus dimensionless time at R.H.= 52%.

Figure (26) illustrates the relation between Sherwood number and dimensionless time at different relative humidity and ambient temperature of 20°C. It is clear that Sherwood number increases uniformly with time and the lower relative humidity led to a significant decrease in Sherwood number. Figure (27) shows Sherwood number versus dimensionless time at constant relative humidity and different air temperature. It is clear that Sherwood number increases uniformly with time and the lower the air temperature, the higher Sherwood number.

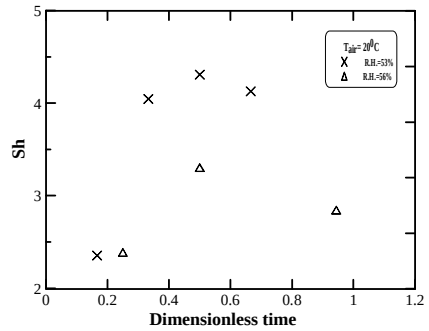

Fig.(26). Time average Sherwood number versus dimensionless time at Tair= 20 OC.

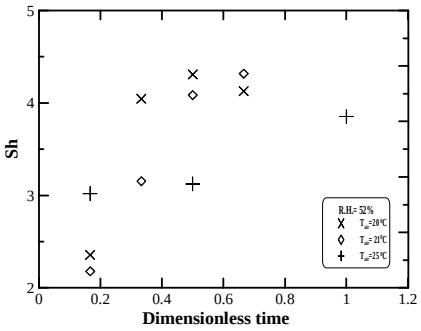

Fig. (27). Time average Sherwood number versus dimensionless time at R.H.=52%.

8.7 Comparison between present experimental and previous results

Figure (28) represents the mass of the frost accumulated variation with dimensionless time for the present experimental work and Gao *et al.*[21] numerical study at the same air temperature, relative humidity, and plate temperature .It is clear that the mass accumulated from the present model is higher than that of Gao *et al.*[21] and this is due the difference in the surface areas between the present and previous work.

Figure (29) represents the frost thickness variation with dimensionless time for present model and Gao *et al.*[21] at the same air temperature, relative humidity, and plate temperature. It is observed that the comparison between the two models shows a fairly in a good agreement.

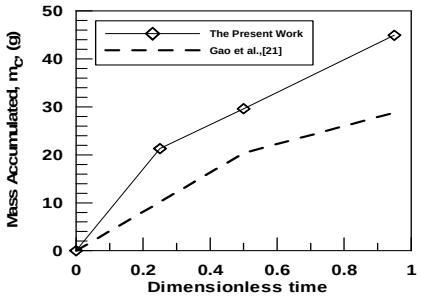

Fig.(28). Comparison between the present experimental data and the model of Gao *et al.* [21] for the collected mass.

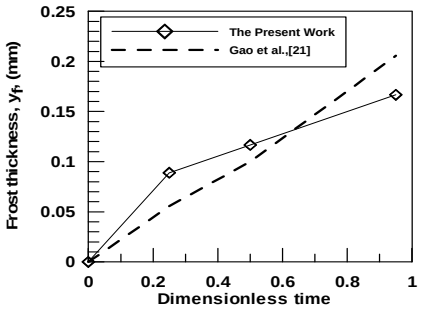

Fig.(29). Comparison between the present experiments and the model of Gao et.al. [21] of the frost thickness.

8.8 Heat and mass transfer correlations

The heat and mass transfer experimental results are correlated. The affecting parameters are the following: mass flow rate, the heat flux, the plate length, density, thermal conductivity, and temperature difference or thermal diffusivity. These correlations can be expressed as follows:

$$Nu = 2.46\ Ra^{0.21} \quad (27)$$

$$Sh = 2.01437\ Ra_m^{0.027057} \quad (28)$$

The correlations (27) and (28) are valid for; 10^4 <Ra < $1.2x10^6$ within error of ± 12% for Nusselt number and ± 10% for Sherwood number as shown in Figs.(30) and (31).

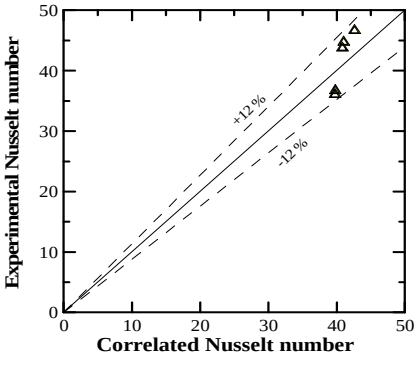

Fig.(30). Comparison of Nusselt number between the present experiments and the calculated results for (104 <Ra < 1.2x106).

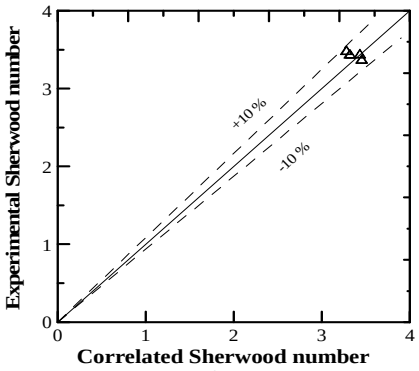

Fig.(31). Comparison of Sherwood number between the present experiments and the calculated results for (104 <Ra < 1.2x106).

8.9 Comparison between the present theoretical and experimental results:

Figure (32) shows the relation between theoretical and experimental average Nusselt number and Rayleigh number. One can observe that the average Nusselt number in both cases take the same trend but the experimental ones is higher than the theoretical; this is because of the assumptions of constant properties in the theoretical model.

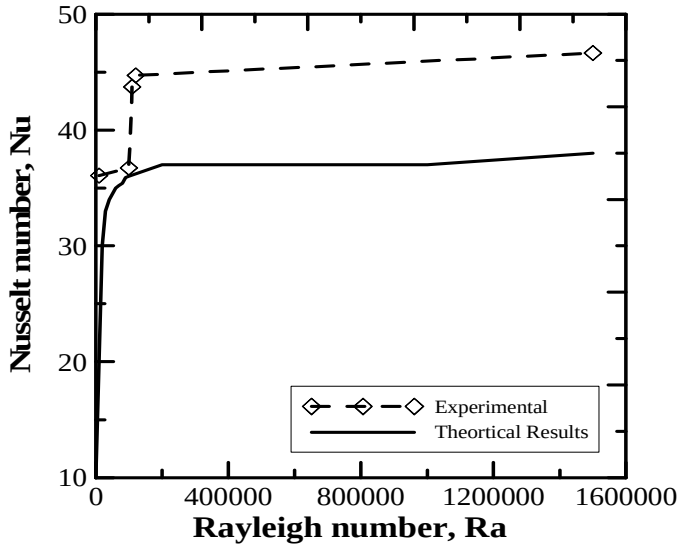

Fig.(32). Comparison between present theoretical and experimental results.

9. CONCLUSION

This study presents a mathematical model to predict the frost layer growth and the characteristics of its heat and mass transfer by coupling the air flow with the frost layer assuming the frost as a porous media. Also, the experimental facility is developed and constructed to investigate the frost growth process. The following remarks are concluded:

1- The frost layers accumulation causes degradation in the performance of the heat exchanger

2- The heat transfer coefficient is inversely proportional to the dimensionless time and accordingly Nusselt number.

3- Due to the degradation in the performance of the heat exchanger, subsequently the decrease in the COP will be significant as:

- The system coefficient of performance decreases within a range of (10% - 15%).
- The average Nusselt number varies within a range of (15% - 30%).
- The average Sherwood number varies within a range of (25% - 40%).

10. REFERENCES

[1] Kennedy, L.A., and Goodman J., "Free Convection Heat and Mass Transfer Under Conditions of Frost Deposition*", Int. J. of Heat and Mass Transfer*, Vol. 17, No. 4, (1974), pp. 477-484.

[2] Marinyuk, B. T., "Heat and Mass Transfer under Frosting Conditions", *Int. J. of Refrigeration*, Vol. 3, No. 6, (1980), pp. 366-368.

[3] Östin, R. and Andersson, S., "Frost Growth Parameters in a Forced Air Stream "*Int. J. of Heat and Mass Transfer*, Vol. 34, No. 4-5, (1991), pp. 1009-1017.
[4] Tao, Y.X., Besant R.W. and Rezkallah K. S., "A Mathematical Model for Predicting the Densification and Growth of Frost on a Flat Plate" *Int. J. of Heat and Mass Transfer*, Vol. 36, No. 2, (1993), pp. 353-363.
[5] Le Gall, R., Grillot J. M. and Jallut, C., "Modeling of Frost Growth and Densification", *Int. J. of Heat and Mass Transfer*, Vol. 40, No. 13, (1997), pp. 3177-3187.
[6] Wu, X. M. and Webb, R. L., "Investigation of the Possibility of Frost Release From a Cold Surface", *Experimental Thermal and Fluid Science*, 24, No. 3-4, (2001), pp. 151-156.
[7] Fossa, M., and Tanda, G., "Study of Free Convection Frost Formation on a Vertical Plate", *J. of Experimental Thermal and Fluid Science*, Vol. 26, (2002), pp. 661–668.
[8] Cheng, C.H., and Wu, K. H., "Observations of Early-Stage Frost Formation on a Cold Plate in Atmospheric Air Flow", *J. of Heat Transfer*, Vol. 125, (2003), pp. 95-101.
[9] Lee, K.S., Jhee, S., and Yang, D., "Prediction of the Frost Formation on a Cold Flat Surface", *Int. J. of Heat and Mass Transfer*, Vol. 46, (2003), pp. 3789–3796.
[10] Cheng, C., and Shiu, C. "Oscillation Effects on Frost Formation and Liquid Droplet Solidification on a Cold Plate in Atmospheric Air Flow", *Int. J. of Refrigeration*, Vol. 26, (2003), pp. 69–78.
[11] Shin, J., Lee, H., Ha, S., Choi, B., and Lee, J., "Frost Formation on a Plate with Different Surface Hydrophilicity", *Int. J. of Heat and Mass Transfer*, Vol. 47, (2004), pp. 4881–4893.
[12] Lee, K. S., and Yang, D., "Dimensionless Correlations of Frost Properties on a Cold Plate", *Int. J. of Refrigeration*, Vol. 27, (2004), pp. 89–96.
[13] Yang, D., and Lee, K. S., "Modeling of Frosting Behavior on a Cold Plate", *Int. J. of Refrigeration*, Vol. 28, (2005), pp. 396–402.
[14] Lee, Y. B., and Ro, S. T., "Analysis of the Frost Growth on a Flat Plate by Simple Models of Saturation and Super Saturation", *J. of Experimental Thermal and Fluid Science*, Vol. 29, No. 6, (2005), pp. 685-696.
[15] Tso, C. P., Cheng, Y. C., and Lai, A. C. K., "Dynamic Behavior of a Direct Expansion Evaporator Under Frosting Condition, Part I. Distributed Model", *Int. J. of Refrigeration*, Vol. 29, (2006), pp. 611–623.
[16] Xiaomin, W, Wantian, D, Wangfa, X, and Liming, T., "Meso-scale Investigation of Frost Formation on a Cold Surface" *J. of Experimental Thermal and Fluid Science*, Vol. 31, (2007), pp. 1043–1048.
[17] Getu, M., and Bansal, P. K., "Modeling and Performance Analyses of Evaporators in Frozen-Food Supermarket Display Cabinets at Low Temperatures", *Int. J. of Refrigeration*, 30, No. 7, pp. 1227-1243.

[18] Piucco R. O., Hermes C. J. L., Melo, C., and Barbosa, J. R., "A Study of Frost Nucleation on Flat Surfaces", *Experimental Thermal and Fluid Science*, Vol. 32, No. 8, (2008), pp. 1710-1715.
[19] Gupta J. K., Gopal M., and Chakraborty, S., "Modeling of a Domestic Frost-free Refrigerator", *Int. J. of Refrigeration*, Vol. 30, (2007), pp.311-322.
[20] Laguerre O., Remy, D., and Flick, D.**,** "Airflow, Heat and Moisture Transfers by Natural Convection in a Refrigerating Cavity", *J. of Food Engineering*, Vol. 91, (2009), pp. 197–210.
[21] Gao, B., Dong, Z., Cheng, Z., and Luo, E., "Numerical Analysis of the Channel Wheel Fresh Air Ventilator under Frosting Conditions", *HVAC Technologies for Energy Efficiency*, Vol. 4, (2006).

انتقال الحرارة وتكون الجليد على مبخر لوحي

جمال سلطان[١،٢]، السيد الشافعي[١]، محمد سعفان[١]، محمد عبد الرؤوف

[١] كلية الهندسة بجامعة المنصورة – المنصورة – مصر

[٢] كلية الهندسة بجامعة القصيم – بريدة - السعودية

Email: gisultan@mans.edu.eg

(قدم للنشر في ٢٠١١/٣/٢م ؛ قبل للنشر في ٢٠١٢/٢/٢٤م)

ملخص البحث. في هذه الدراسة تم عمل دراسة نظرية ومعملية لانتقال الحرارة والكتلة لهواء رطب يمر على سطح بارد مع تكون طبقة الصقيع . في الدراسة النظرية تم وصف الظاهرة بمعادلات تفاضليه جزئية في حالة السريان وكمية الحركة والطاقة والتركيز في حالة عدم الاستقرار وتم فرض أن السريان رقائقى فوق السطح البارد وتأثير تغير كثافة بخار الماء الموجود في الهواء على انتقال الكتلة والحرارة المصاحبة بالحمل الرقائقى الحر. ثم تم حل المعادلات بطريقة الفروض المحدودة في اتجاهين باستخدام حزمة برامج جاهزة (Fluent 3.2.1) في الاتجاهات الثلاثة وذلك لإيجاد توزيع درجة الحرارة والسرعة والكثافة وسمك طبقة الصقيع فوق السطح الأفقي البارد ومعامل انتقال الحرارة والكتلة وكذلك رقمي نوسلت وشيروود.

وفى الدراسة المعملية تم تصميم وتنفيذ دائرة تبريد وتزويدها بأجهزة قياس لدرجة حرارة السطح الأفقي البارد وكذلك قياس الجهد والتيار اللحظي لضاغط التبريد طوال التجارب المعملية وكذلك وزن كتلة الماء في نهاية كل تجربة وكذلك زمن التشغيل وتم عمل التجارب في الظروف الجوية العادية حيث تتراوح درجة حرارة الهواء الجوى ٢٠°C إلى ٢٥°C والرطوبة النسبية تتراوح من ٤١٪ إلى ٥٦٪ ومتوسط درجة حرارة السطح تقريبا -١٠°C وتراوح مدى رقم رايلى كعامل مؤثر من ١٠٤ إلى x1061,2 والزمن اللابعدى من ٠ إلى ١ . وقد بينت هذه الدراسة مع تكون طبقة الجليد على سطح المبخر انخفض معامل أداء دائرة التبريد بنسبة تتراوح بين ١٠٪ و ١٥٪ ، تغير رقم نوسلت المتوسط بنسبة تتراوح بين ١٥- ٣٠٪ بينما تغير رقم شيروود المتوسط بنسبة تتراوح بين ٢٥-٤٠ ٪ .

Journal of Engineering and Computer Sciences
Qassim University, Vol. 5, No. 1, pp. 77-92 (January 2012/Safar 1433H)

Numerical Simulation of Mixed Convection from Longitudinal Fins in a Horizontal Rectangular Channel

A. S. Alosaimy
Mechanical Engineering Department, Faculty of Engineering,
Taif University, Taif 21974, Saudi Arabia
alosaimy@yahoo.com

(Received 18/4/2011; accepted for publication 4/11/2011)

ABSTRACT. A numerical investigation was undertaken to investigate heat transfer in three-dimensional laminar mixed convection heat transfer from longitudinal fins in a horizontal rectangular channel. Numerical simulations were conducted at different fin spacing, Reynolds number of 1500 and modified Rayleigh number of 4 x 10^7 and 2x 10^8 for fin to channel height ratios of 0.5 and 0.25. Validity of the modelling technique is verified by comparing computational results with corresponding experimental data from literatures. The numerical model is able to simulate the mixed convective flow through a rectangular channel subjected to constant heat flux heating boundary conditions. The predicted heat transfer coefficient and local Nusselt number distribution shows a good agreement with the experimental results and its improvement with higher channel height ratio at the expense of increased pressure drop across the longitudinal fins.

Keywords: longitudinal fins, mixed convection, Numerical simulation.

NOMENCLATURE

A	channel cross sectional area, m^2
C_p	Specific heat, kJ/ kg
f	friction factor
D_h	channel hydraulic diameter, 4A/P, m
G	gravitational acceleration, m/s^2
h_{av}	average convective heat transfer coefficient, W/m^2K
H	channel height, m
H_f	fin height, m
k	air thermal conductivity, W/m K
L	channel heated length, m
L_m	length of te model, m
Nu_{av}	average Nusselt number, $Nu_{av}=h_{av}D_h/k$
Nu_{wx}	local Nusselt number, $Nu_{wz}= q_{con} D_h/ ((T_{wx}-T_{in}) k)$
p	pressure, Pa and perimeter, m
q_{con}	Convection heat flux, W/m^2
Ra^*	modified Rayleigh number, $Ra^*=(g\beta q_{con}D_h^4)/(k\,\alpha\upsilon)$
Re	Reynolds number, $Re= u_{in} D_h/\upsilon$
S	fin spacing, m

T	temperature, K
T_{wx}	local wall temperature, K.
u	u-velocity componente, m/s
U	streamwise bulk velocity, m/s
v	v-velocity component, m/s
W	half channel width, m
x_w	axial distance along heated wall,m
x	x-coordinate direction
y	y-coordinate direction
z	z-coordinate direction

Greek letters

α	thermal diffusivity, m^2/s
β	thermal expansion coefficient, 1/K
υ	kinematic viscosity, m^2/s
ρ	density, kg/m^3
τ	shear stress, N/m^2

Subscripts

av	average
f	fin
in	inlet
w	wall
x	x-direction

1. INTRODUCTION

Fins are widely used to enhance convective heat transfer in engineering applications such as solar collectors, heat exchangers, HVAC industries and substation transformers. Many types of flat fins have been presented by Shah and Sekulic' [1]. The most common were the plain, wavy and interrupted and the first types of fins were used in those applications in which the pressure drop is quite low.

Krikkis and Razelos [2] presented correlations for optimum dimensions of longitudinal rectangular and triangular radiating fins with mutual irradiation. Kasbioui *et al.* [3] studied the heat transfer and fluid flow by mixed convection in a vertical rectangular cavity containing adiabatic partitions attached to the heated wall. The parameters of Rayleigh number, Reynolds number, aspect ratio of the cavity and the aspect ratio of the micro cavities were considered. The results indicated that the heat exchange between the system and the external medium, through the cold wall and the upper vent, were considerably affected by the presence of the partitions.

Experiments were performed by Maughan [4] to determine secondary flow development and Nusselt number distributions for laminar mixed convection in the thermal entry region of a parallel plate channel heated uniformly from below. Longitudinal distributions of the local Nusselt number initially followed forced convection. Subsequent mixing associated with the development of secondary flow caused Nusselt numbers to rise to an initial maximum before decreasing slightly and assuming a fully developed value. Tiwade and Pathare [5] investigated experimentally the performance of continuous longitudinal fins solar air heater. They demonstrated that the addition of continuous longitudinal fins to the upper or bottom side of the absorber plate improves the heat transfer rate. Also, it is found that effective heat transfer coefficient is maximum for the smallest pitch of the longitudinal fins, in addition the friction factor and pressure drops are found lowest with largest Reynolds number.

Mixed convection heat transfer from longitudinal fins inside a horizontal channel has been investigated by Dogan and Sivrioglu [6] in the natural convection dominated region for a wide range of Rayleigh numbers and different fin heights and spacing. An experimental parametric study was made to investigate effects of fin spacing, fin height and magnitude of heat flux on mixed convection heat transfer from rectangular fin arrays heated from below in a horizontal channel. The optimum fin spacing to obtain maximum heat transfer has also been investigated. Experiments were conducted for Reynolds number of 250 and modified Rayleigh numbers ranging between 3×10^7 and 6×10^8. The results showed that the dimensionless optimum fin spacing to channel height (S/H) which yields the maximum heat transfer is between $S/H = 0.08$ and $S/H = 0.12$. Results also show that optimum fin spacing depends on modified Rayleigh number and fin height. They conducted the same experiments with different inlet conditions [7]. Experiments were conducted for Reynolds number of 1500 and modified Rayleigh numbers ranging between 3×10^7 and 8×10^8. The results showed that the dimensionless optimum fin spacing

to channel height (S/H) which yields the maximum heat transfer is between S/H = 0.08 and S/H = 0.09.

Numerical investigation of shrouded fin array under combined free and forced convection was studied by Al-Sarkhi *et al.* [8]. It is concluded that Nusselt number is significantly enhanced by the effects of buoyancy in the mixed convection regime.

Biswas et al [9] carried out numerical computation of laminar mixed convection flows and heat transfer in a rectangular channel with geometrical fin configuration to represent a part of gas-liquid, fin-pipe cross flow heat exchanger (gas side). The mixed convection condition was characterized by buoyancy induced secondary flows leading to increase the vortex strength and improve the heat transfer. Wu and Perng [10] studied the simulation of laminar mixed convection in a horizontal channel containing heated blocks. The effect of an oblique plate on the heat transfer improvement was obtained. These results show that the installation of the plate can improve the heat transfer and flow field instability.

Yalcin et al [11] investigated the effects of clearance parameters on the steady-state heat transfer. A finite volume based CFD code was used in order to solve the three-dimensional elliptic governing equations. The numerical results have been compared to existing experimental values from the literature and the comparison showed a good agreement. It was found that the heat transfer coefficient increases with the increase in the clearance parameter and it approaches to the value of heat transfer coefficient obtained for un-shrouded fin arrays. Four basic fins of the plate-fin heat exchangers have been modelled and simulated by Zho and Lee [12]. Three-dimensional numerical simulations on the flow and heat transfer in the four fins were investigated and carried out at laminar flow regime. Validity of the modelling technique was verified by comparing computational results with both corresponding experimental data and three empirical correlations from literatures.

The objective of the present study is to perform numerical three-dimensional simulation of mixed convection heat transfer from longitudinal fin arrays in a horizontal channel. The validity of the calculations was verified by comparing the computational results with corresponding experimental data of Dogan and Sivrioglu [7]. All computations were performed using ANSYS FLUENT 12- CFD code.

2. MODEL DESCRIPTION AND SIMULATION

The problem analyzed in this study involved convective heat transfer in a rectangular duct with longitudinal fins of 1 mm thickness each attached to the bottom wall. The computational domain of the physical problem is shown in Figure 1. The problem is modeled using one face as symmetric plane along the flow. By exploiting the symmetry of the flow field in the spanwise direction, and the width of the computational domain is reduced to half of the actual width of the duct (W = 0.15 m) with channel height H of 0.10 m. The length of the model L_m is equal to 1.0 m and consists of unheated entrance region L_{in} of 0.20 m, heated wall involving longitudinal fins L of 0.60 m and finally the unheated exit region L_{ex} of 0.20 m. Two fin heights H_f are considered in this investigation to satisfy fin height ratios H_f/H of

0.25 and 0.50. Thin aluminum fins of 1mm thick are considered with different spacing S.

Calculations were carried out using inlet Reynolds number of 1500 and modified Rayleigh number Ra* of 4 x 10^7 and 2x 10^8 for fin to channel height ratios H_f/H of 0.5 and 0.25 respectively. In the experimental results of Dogan, M., Sivrioglu. [7], it has been shown that values of Richardson number for fin heights H_f/H= 0.25 and 0.50 at different fin spacing ratios indicates the dominant effect of mixed convective heat transfer for these conditions experimental.

The steady laminar three-dimensional momentum and energy equations are solved numerically (using finite volume scheme) together with the mass conservation equation to simulate the thermal and the flow fields. The equations are expressed in the Cartesian tensor notation and given by:

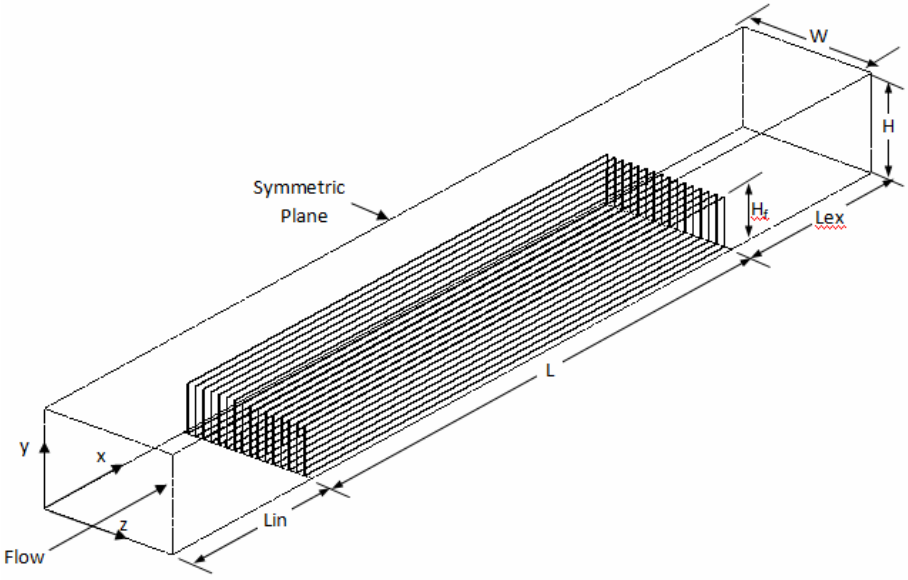

Fig.(1). Three-dimensional computational model.

Mass conservation equation:

$$\frac{\partial}{\partial x_i}(\rho u_i) = 0 \tag{1}$$

Momentum equation

$$\frac{\partial}{\partial x_j}(u_i u_j) = -\frac{\partial p}{\partial x_i} + \frac{\partial}{\partial x_j}\tau_{ij} + \rho_{in} g_i \beta (T - T_{in}) \tag{2}$$

where

$$\tau_{ij} = \mu\left(\frac{\partial u_i}{\partial x_j} + \frac{\partial u_j}{\partial x_i} - \frac{2}{3}\delta_{ij}\frac{\partial u_l}{\partial x_l}\right) \quad (3)$$

Energy Equation:

$$\frac{\partial}{\partial x_j}\left(\rho C_p u_j T\right) = \frac{\partial}{\partial x_j}\left(k\frac{\partial T}{\partial x_j}\right) \quad (4)$$

Here the coordinate direction is referred as x_i ($x_i = x, y, z$), and the velocity component in such direction is represented by u_i ($u_i = u, v, w$).

In the present study all computations were performed using ANSYS FLUENT 12- CFD code. The simulation of three-dimensional flow was adopted with assumption of steady laminar flow conditions. The momentum and energy equations governing the fluid motion and the energy transport for incompressible flow were solved through the Finite Volume Method, using a three-dimensional formulation with the SIMPLEC-algorithm for pressure velocity coupling.

The mesh consisted of 247197 binary nodes and 65216 quadrilateral wall faces at heated rib-channel interface. The interior faces were counted as 59792 quadrilateral in the ribs and 2596146 (triangular) in the channel area. In total 1310871 mixed cells were generated for the entire model. The exterior walls of the channel were set as isothermal and the bottom wall was subjected to a constant heat flux. Average values of heat transfer coefficient are evaluated from the following expression:

$$h_{av} = \frac{1}{A}\int h dA \quad (5)$$

3. RESULTS AND DISCUSSION

3.1 Heat transfer coefficient, local temperature and Nusselt number

The comparison between the predicted values and the experimental results published by Dogan, M., Sivrioglu [7] are presented in Figures 2-4. The Effect of fin spacing on the variation of average convection heat transfer coefficient h_{av} is presented in Figure2. It is shown that the predictions are able to catch the optimum of the h_{av} at fin spacing S= 8 mm as well as the experimental results. However, discrepancies between the present numerical predictions and the published results are evident in both cases of modified Rayleigh number. The average heat transfer is overestimated except for fin spacing greater than 12 mm at Ra* of 4 x 10^7. The maximum deviation between the numerical and the experimental results is 7.6% compared with an uncertainty of around ±6% for the experimental results.

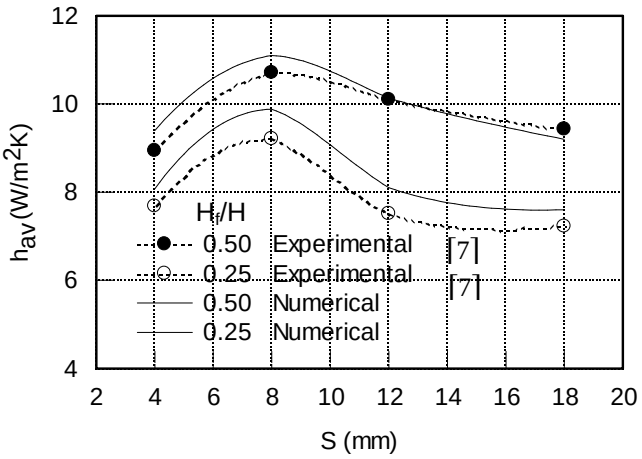

Fig.(2). Variation of average convection heat transfer coefficient with fin Spacing.

The variation of dimensionless temperature and local Nusselt number distributions with the main flow direction are shown in Figures 3 and 4 for different modified Rayleigh number , fin heights H_f/H= 0.25 and 0.50 for the same fin spacing ratio S/H=0.08. It is seen that the numerical and the experimental results have the same trend and the dimensionless temperature is underestimated up to 80% of the heated wall length. This results are associated with higher predicted local Nusselt number, and the predicted maximum dimensionless temperature is close to the experimental value for fin height H_f/H= 0.50 at modified Rayleigh number Ra* of 4×10^7.

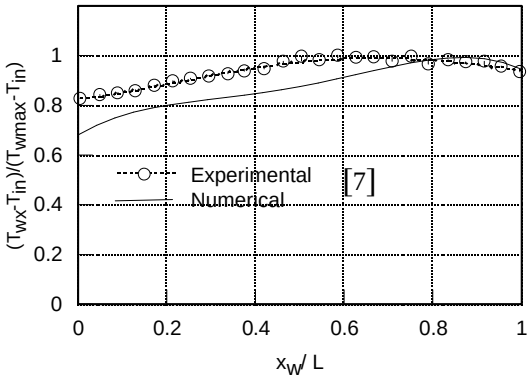

(a)

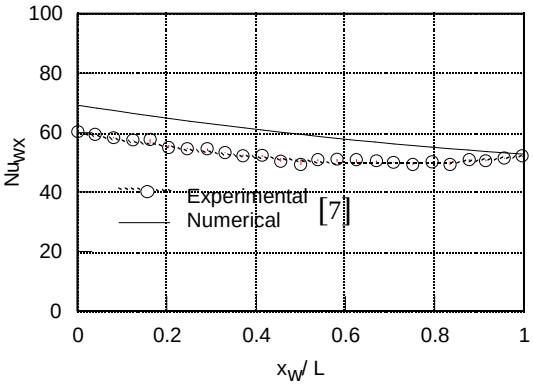

(b)

Fig.(3). (a) Variation of the temperature distribution and (b) variation of local Nusselt number with the main flow direction (S/H=0.08 and Hf /H=0.25).

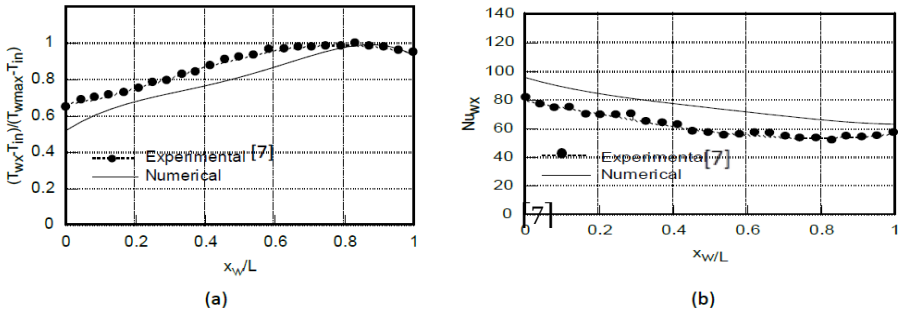

Fig. (4). (a) Variation of the temperature distribution and (b) variation of local Nusselt number with the main flow direction (S/H=0.08 and Hf /H=0.50)

3.2 Temperature profiles

The temperature profiles on the heated bottom wall with 16 Longitudinal fins is shown in Figure (5). It is clear that the temperature increases in the streamwise flow direction. The temperature at the side wall of the channel increases near the exit section. This may be attributed to the very low velocities at the corner of the channel located between the bottom and the side wall. [7]

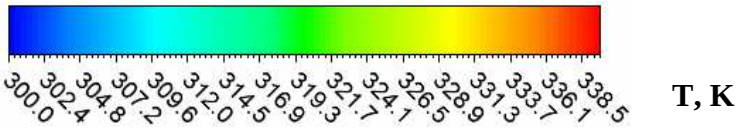

Side wall

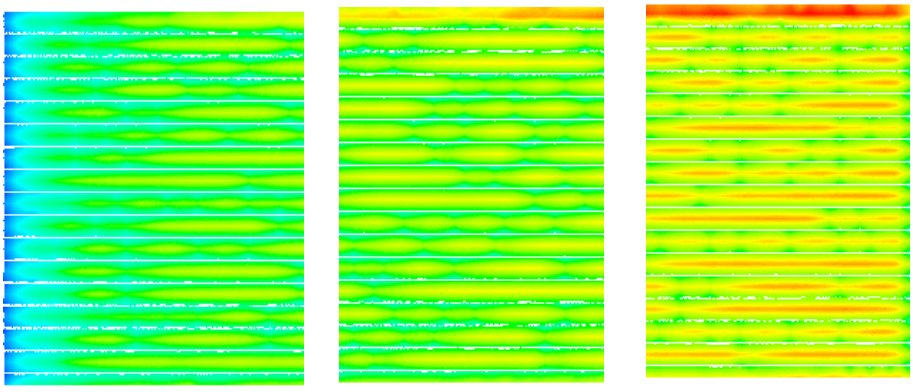

Symmetric plane

Near Inlet Middle Section Near Exit

Fig. (5). Temperature profiles on the heated wall (S/H=0.08 and H_f/H=0.50).

The temperature profiles across and along flow symmetric plane are shown in Figures (6 and 7) for the case of S/H=0.08 and H_f/H=0.50. It is clear that temperature gradients are evident due to heat transfer from bottom wall and the walls of fins. Higher temperatures are shown between ribs and in particular at the proximity of the bottom wall. A large region of the duct outside the fin grooves is occupied with air having the same temperature of inlet condition. This region is extended along the flow up to the middle section of the duct.

3.3 Velocity profiles

The velocity vectors plots along the flow and velocity component v at symmetric plane are shown in Figures(8 and 9). The flow velocities at the upper region, which is not occupied by fins, shows a lower values compared with the velocities at the region between fins. In addition, such region reaches the fully developed profile of streamwise velocities as shown in Figure (10). The peak streamwise velocity tends to have a maximum value at the central section of the duct. The magnitudes of the v velocity components near the inlet section of the duct exhibits negative values to indicated a downward flow at this region. This is attributed to the weak effect of heat transfer at the inlet section of the duct to force the air upward due to low temperature as presented in Figure (8). However, due to the higher temperature near the exit of the duct, the cross flow velocity shows higher positive values between the fins except a small region close to the sidewall of the duct.

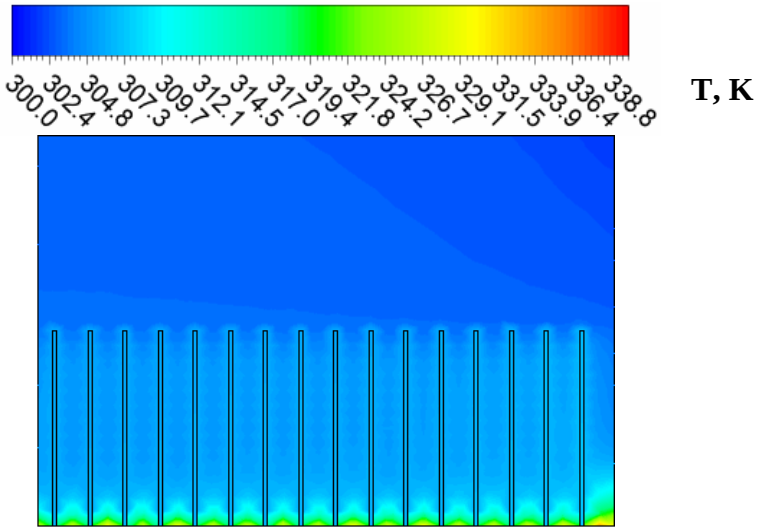

Fig. (6). Temperature profiles across the flow at xw/L =0.5 (S/H=0.08 and Hf/H=0.50).

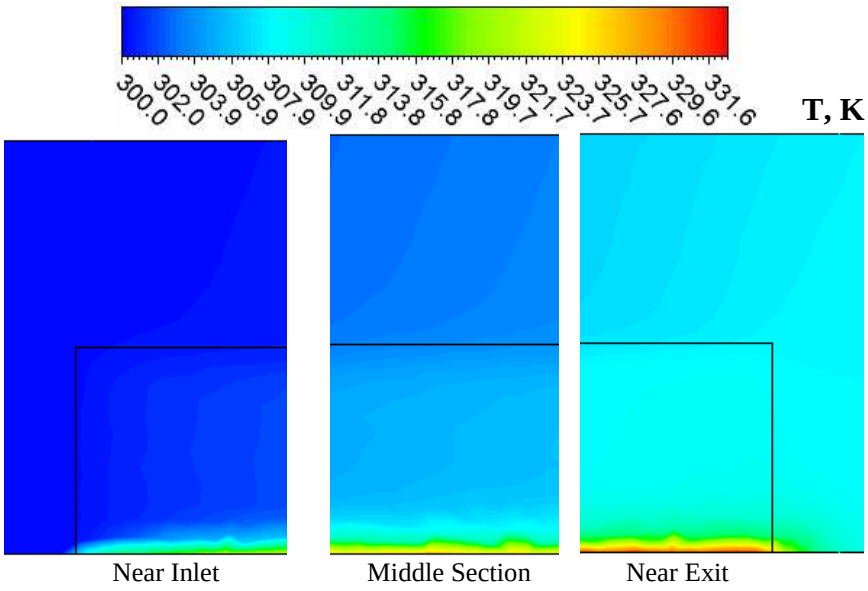

Fig. (7). Temperature profiles at symmetric plane (S/H=0.08 and Hf/H=0.50).

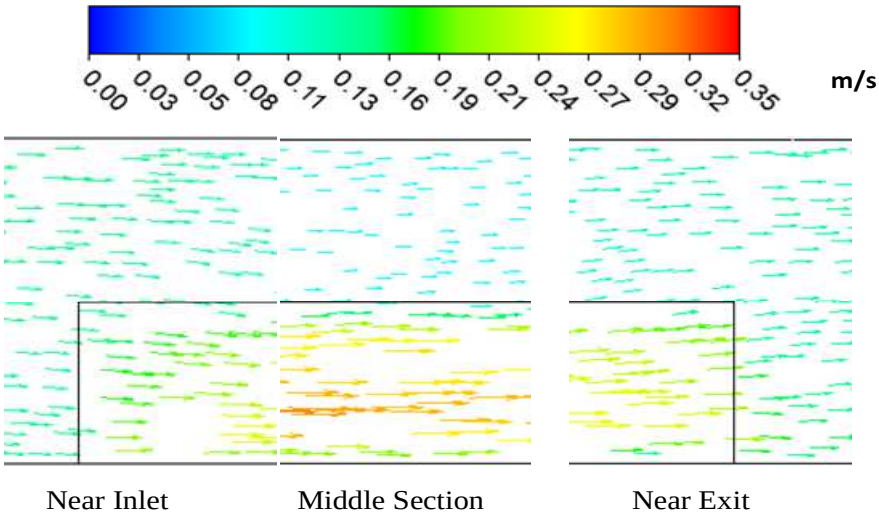

Fig.(8). Velocity vectors plots along the flow at Symmetric plane (S/H=0.08 and Hf/H=0.50).

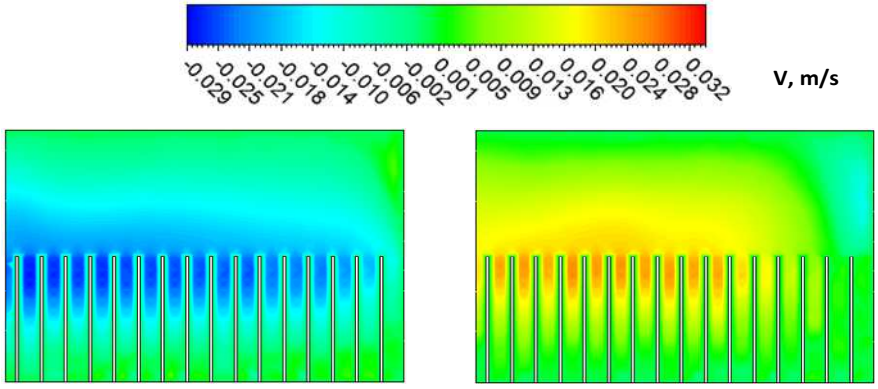

Fig.(9). Velocity profiles across the flow in y-direction (S/H=0.08 and Hf/H=0.50).

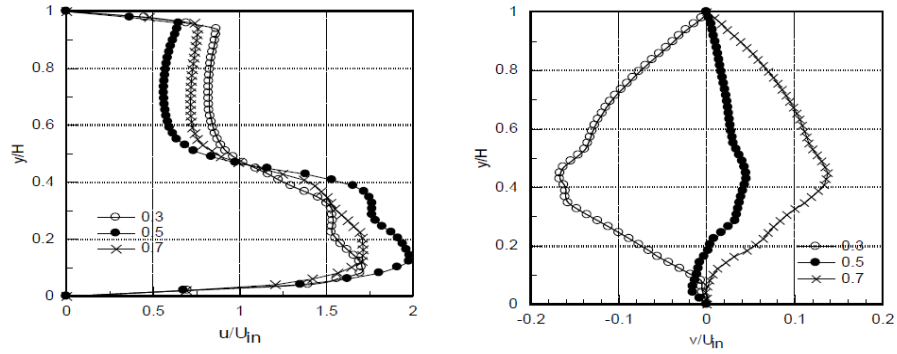

Fig.(10). Velocity distributions at symmetric plane (S/H=0.08 and Hf/H=0.50).

3.4 Friction factor

The pressure drop Δp is defined as the calculated difference between the channel inlet and the channel exit of the model, and the friction factor f, which measures the dimensionless pressure drop, is given by:

$$f = \frac{\Delta p}{\frac{1}{2}\rho U^2}\left(\frac{D_h}{4L_m}\right) \quad (6)$$

The effect of fin spacing (S/H) on the friction factor for fin to channel height ratios (H_f/H) of 0.25 and 0.5 are shown in Figure 11. It is noticed that, the friction factor increases significantly with decreasing spacing ratio and increasing the channel height ratios. This is attributed to the flow resistance generated by the presence of longitudinal fins. The number of fins for (S/H) =0.04, 0.08 and 0.12 are

59, 32 and 12 respectively and more flow resistance and hence pressure drop are expected for higher number of fins or lower values of channel spacing to height ratio.

By investigating Figures (2 and 11), it is seen that the average convection heat transfer coefficient can be improved with higher channel height ratio at the expense of increased pressure drop across the longitudinal fins. The results of calculations showed that, at fin spacing (S/H)=0.08, the average heat transfer coefficient is increase by 12.3% with increasing fin heights (Hf/H) from 0.25 to 0.5. This improvement is associated with an increase in pressure drop by 23.1%.

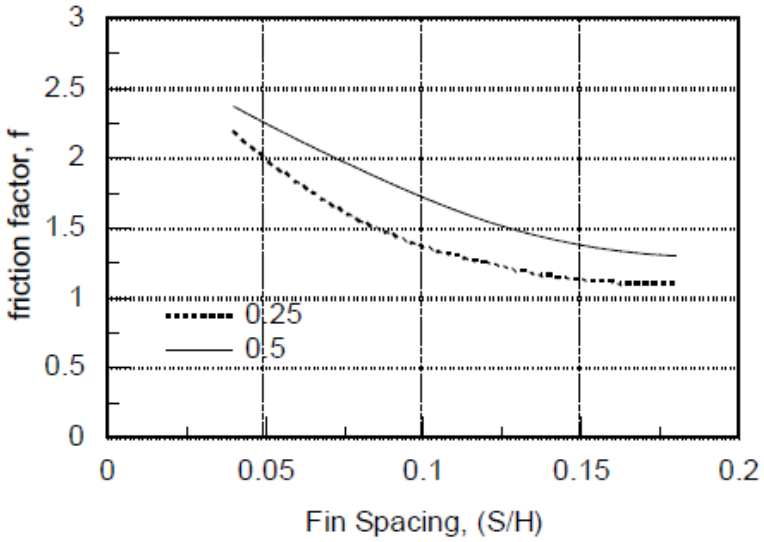

Fig. (11). Effect of fin spacing on the friction factor.

4. CONCLUSIONS

Results from numerical simulations of three-dimensional laminar mixed convection heat transfer from longitudinal fins in a horizontal rectangular channel are validated by experimental work given in literature. Numerical simulations are conducted at Reynolds number of 1500 and modified Rayleigh number of 4×10^7 and 2×10^8 for fin to channel height ratios of 0.5 and 0.25 respectively. The following conclusions may be drawn:

1- The predicted average convection heat transfer coefficient at various configurations of fin spacing and height ratios shows a good agreement with the experimental results.

2- The streamwise velocities between fins reached the fully developed profile and the heating of bottom wall affected the direction of cross flow velocity component downstream of channel inlet section.

3- The friction factor of three-dimensional laminar mixed convection heat transfer from longitudinal fins is significantly increased with decreasing spacing ratio and increasing the channel height ratios.
4- The average convection heat transfer coefficient can be improved with higher channel height ratio at the expense of increased pressure drop across the longitudinal fins.

5. REFERENCES

[1] Shah, D. and Sekulic', D. P., *Fundamentals of heat exchanger design*, Page 699, John Wiley & Sons, Inc., 2003.

[2] Krikkis R.N.و and Panagiotis R., "Optimum Design of Space craft Radiators with Longitudinal Rectangular and Triangular Fins", *J. Heat Transfer*, Vol.124, (2002), pp. 805-811.

[3] Kasbioui, E.K., and Lakhal, M. H., "Mixed convection in rectangular enclosures with adiabatic fins attached on the heated wall", *Engineering Computations*, Vol. 20 No. 2, (2003), pp.152 – 177.

[4] Maughan, J. R. "An experimental and numerical investigation of mixed convection in channels and the application of extended surfaces for heat transfer enhancement", *Journal of Engineering Physics and Thermophysics*, Vol. 19, No. 2, pp. 1011-1015.

[5] Tiwade, P. C., and Pathare, N.R., "Experimentation and performance analysis on continuous longitudinal fins solar air heater", *2nd International Conference on Engineering and Technology (ICETET)*, (2009), pp. 1047-1051.

[6] Dogan, M., and Sivrioglu, M., "Experimental investigation of mixed convection heat transfer from longitudinal fins in a horizontal rectangular channel: In natural convection dominated flow regimes", *Energy Conversion and Management*, Vol. 50, No. 10, (2009), pp. 2513- 2521.

[7] Dogan, M., and Sivrioglu, M., "Experimental investigation of mixed convection heat transfer from longitudinal fins in a horizontal rectangular channel", *International Journal of Heat and Mass Transfer* Vol. 53, (2010), pp. 2149-2158.

[8] Al-Sarkhi, A. Abu-Nada, E., Akash, B. A. and Jaber, J. O., "Numerical investigation of shrouded fin array under combined free and forced convection", *Int. Commun. Heat Mass Transfer*, Vol. 30, (2003), pp. 435–444.

[9] Biswas, G., Mitra, N. K., and Fiebig, M., "Computation of laminar mixed convection flow in a rectangular duct with wing-type built-in obstacles", AIAA, *Thermophysics, Plasmadynamics and Lasers Conference*, San Antonio, TX, (1988), pp. 27-29.

[10] Wu, H. W., and Perng, S. W., "Effect of an Oblique Plate on the heat transfer enhancement of mixed convection over heated blocks in horizontal channel", *International Journal of Heat Transfer*, Vol. 42, (1999), pp. 1217-123.

[11] Yalcin, H. G., Baskaya, S., and Sivrioglu, M., "Numerical analysis of natural convection heat transfer from rectangular shrouded fin arrays on a horizontal surface", *Int. Commun. Heat Mass Transfer* Vol. 35, (2008), pp. 299–311.

[12] Zho, Y., and Lee, Y., "Three-dimensional numerical simulation on the laminar flow and heat transfer in four basic fins of plate-fin heat exchangers", *J. Heat Transfer*, Vol. 130, No. 11, (2008), pp. 111-122.

المحاكاة العددية لانتقال الحرارة بالحمل المختلط من زعانف طولية في قناة أفقية مستطيلة

علي العصيمى

قسم الهندسة الميكانيكية كلية الهندسة – جامعة الطائف –المملكة العربية السعودية-
alosaimy@yahoo.com

(قدم للنشر في ٢٠١١/٤/١٨م ؛ قبل للنشر في ٢٠١١/١١/٤م)

ملخص البحث. لقد تم إجراء دراسة عددية لبحث انتقال الحرارة بالحمل المختلط لزعانف طولية في قناة مستطيلة أفقية ثلاثية الأبعاد ولتدفق رقائقي. وقد تم عمل المحاكاة العدديه عند قيم مختلفة من المسافات بين الزعانف وعند رقم رينولدز ١٥٠٠ وعند قيم رقم ريليه المعدل قدرها ٤٠ مليونا و٢٠٠ مليون ولنسبة ارتفاع الزعانف إلى ارتفاع القناة من ٠,٥ إلى ٠,٢٥. وقد تم التحقق من مصداقية اسلوب المحاكاه من خلال مقارنة النتائج الحسابية مع نتائج التجارب المعملية في ظروف مناظرة لباحثين سابقين. ويستطيع البرنامج العددي محاكاة انتقال الحرارة بالحمل المختلط خلال القناة المستطيلة والتي تخضع لتدفق حرارة منتظم كظروف حدية. كما بينت الدراسة أن التوزيع الموضعي لقيم كل من معامل انتقال الحرارة ورقم نوسلت خلال القناة توافقت بشكل جيد مع القيم التجريبية بالإضافة إلى تحسن ملحوظ في معدل انتقال مع زيادة نسبة الارتفاع في القناة وذلك على حساب الفقد في الضغط خلال الزعانف الطولية.

قواعد النشر

أهداف المجلة

تهدف المجلة إلى نشر إنتاج الباحثين من داخل الجامعة وخارجها في جميع تخصصات العلوم الهندسية وعلوم الحاسب، والمجالات الرئيسية التي تشملها المجلة هي:

- الهندسة الكهربائية
- الهندسة المدنية
- الهندسة الميكانيكية
- الهندسة الكيميائية
- هندسة التعدين والبترول
- هندسة الحاسب
- علوم الحاسب
- تكنولوجيا المعلومات
- نظم المعلومات
- العلوم الهندسية الأساسية

لغة المجلة:

تقبل المجلة البحوث باللغة الإنجليزية.

أ) المواد التي تقبلها المجلة للنشر:

١- البحث: وهو عمل أصيل للمؤلف (أو المؤلفين) يضيف جديداً للمعرفة في مجال تخصص (فرع المجلة).

٢- المقالة المرجعية: وتتناول العرض النقدي والتحليلي للبحوث والكتب ونحوها التي سبق نشرها في ميدان معين والرسائل العلمية المتميزة.

٣- المقالة القصيرة (تعليق تقني): مقالة قصيرة تحوي تطبيقاً تقنياً.

٤- الابتكارات العلمية المتميزة وبراءات الاختراع.

٥- المراسلات: وتتناول عرض فكرة أو رأي علمي أو اقتراح بحثي.

٦- انتقادات الكتب

ب) شروط النشر:

١- أن يكون البحث متسماً بالأصالة والابتكار والمنهجية العلمية وسلامة الاتجاه وصحة اللغة وجودة الأسلوب.

٢- أن لا يكون البحث قد سبق نشره أو قدم للنشر لجهة أخرى.

٣- جميع البحوث المقدمة للنشر في المجلة خاضعة للتحكيم.

ج) تعليمات النشر:

عند تقديم البحث للنشر يشترط الآتي:

١- أن يقدم الباحث طلباً بنشر بحثه، ويوضح فيه العنوان الالكتروني للمراسلات.

٢- لا يجوز إعادة نشر أبحاث المجلة في أي مطبوعة أخرى إلا بإذن كتابي من رئيس التحرير.

٣- يرسل الباحث بحثه باللغة الانجليزية عن طريق البريد الالكتروني على العنوان الالكتروني المذكور في فقرة المراسلات، وكذلك ملخص باللغتين العربية والإنجليزية بحيث لا تزيد كلماته عن ٢٠٠ كلمة.

٤- يكتب البحث باستخدام برنامج (Microsoft word) ويستخدم font 12 Times New Roman في كتابة المتن، مع ترك مسافة ونصف بين الأسطر.

٥- يجب ألا يزيد عدد صفحات البحث شاملا الرسومات والجداول عن ٢٠ صفحة حجم A4.

٦- أن يكتب عنوان البحث واسم الباحث وعنوانه ولقبه العلمي والجهة التي يعمل بها على الصفحة الأولى مستقلة.

٧- توضع هوامش كل صفحة أسفلها.

٨- يشار إلى المراجع داخل المتن بالأرقام حسب تسلسل ذكرها وتثبت في فهرس يلحق بآخر البحث.

أ) الدوريات: يشار إليها في المتن بأرقام داخل أقواس مربعة على مستوى السطر. أما في قائمة المراجع فيبدأ المرجع بذكر رقمه داخل قوسين مربعين فاسم عائلة المؤلف ثم الأسماء الأولى أو اختصاراتها فعنوان البحث (بين علامتي تنصيص) فاسم الدورية (تحته خط) فرقم المجلد، فرقم العدد فسنة النشر (بين قوسين) ثم أرقام الصفحات.

مثال: الحميدي، إبراهيم عبدالله. "الهجرة الداخلية في المملكة العربية السعودية حجمها واتجاهاتها." مجلة كلية الآداب، جامعة الملك سعود، م١٦، ع١ (٢٠٠٤م)، ١٠١-١٥١.

ب) الكتب: يشار إليها في المتن داخل قوسين مربعين مع ذكر الصفحات، مثال ذلك [٨، ص١٤]. أما في قائمة المراجع فيكتب رقم المرجع داخل قوسين مربعين متبوعاً باسم عائلة المؤلف ثم الأسماء الأولى أو اختصاراتها فعنوان الكتاب (تحته خط) فمكان النشر ثم الناشر فسنة النشر.

مثال: اليوسف، صالح سليمان. المشقة تجلب التيسير: دراسة نظرية وتطبيقية، الرياض: المطابع الأهلية للأوفست، ١٩٨٨م.

٩- ترفق جميع الصور والرسوم المتعلقة بالبحث في ملف مستقل.

١٠- ترقم الجداول والرسومات ترقيماً مستقلاً عن ترقيم البحث ويعنون الجدول بعنوان فوق الجدول والرسم بعنوان تحت الرسم.

١١- لا يعاد البحث إلى صاحبه سواء نشر أو لم ينشر.

١٢- يعطى الباحث نسختين من المجلة وعشرين مستلة من بحثه المنشور.

١٣- يلزم الباحث إجراء التعديلات المنصوص عليها في تقارير المحكمين، مع تعليل ما لم يعدل.

١٤- تعبر المواد المنشورة في المجلة عن آراء ونتائج مؤلفيها فقط.

عناوين المراسلة

E-mail: quecjour@qec.edu.sa


بسم الله الرحمن الرحيم

جامعة القصيم
Qassim University
المجلة العلمية لجامعة القصيم
(مجلة محكمة)

المجلد (٥) – العدد (١)

مجلة
علوم الهندسة والحاسب

صفر ١٤٣٣هـ - يناير ٢٠١٢م

النشر العلمي والترجمة

هيئة التحرير

رقم الإيداع : ٢٠٢٣ / ١٤٢٩

مجلة علوم الهندسة والحاسب،
جامعة القصيم المجلد (٥)، العدد (١)، ص ص ١- ٩٤ بالإنجليزية (يناير ٢٠١٢م / صفر ١٤٣٣هـ)

المحتويات

صفحة